Electron Transport and Performance Degradation in Next Generation Photovoltaic Technologies

By

CHASE M. HANSEN
DISSERTATION

Submitted in partial satisfaction of the requirements for the degree of

DOCTOR OF PHILOSOPHY

in

PHYSICS

in the

OFFICE OF GRADUATE STUDIES

of the

UNIVERSITY OF CALIFORNIA

DAVIS

Approved:

Professor Gergely Zimanyi

Professor Dong Yu

Professor Richard Scalettar

Committee in Charge

2021

This thesis is dedicated to all of those who would help others in times of need, the good humans.

Contents

Abstract

Solar cells are among the most promising green technologies for energy production that exist. While currently solar energy production makes up only around 2% of the total energy production in the United States, in order to maintain a livable planet, it will become a necessity for green technologies like solar energy to displace fossil fuels in the coming years. Because our society places great value in economic well-being as well, it is hard to sell the idea of solar cells over their competitors unless the effective dollar per watt is comparable or better. To this end, it is imperative to improve on this figure of merit in any way possible, to help the solar cell industry replace fossil fuels with their much greener alternative. In this dissertation, I show the progress I've made on this front from the standpoint of computational condensed matter physics. In the first several chapters, I explore various physical phenomena that greatly affect the efficiency in nanoparticle solar cells, and model various systems to try to better understand one of the great roadblocks for nanoparticle solar technologies, their low carrier mobility, which leads to a low efficiency. In the final chapter, I shift focus to a more proven technology, Heterojunction with Intrinsic Thin layer (HIT) solar cells. HIT solar cells exhibit faster degradation than their crystalline silicon counterparts, and as such, have a higher averaged dollar per watt over their lifetime, despite their out-of-the-box world record holding terrestrial efficiencies. This degradation is not fully understood at a fundamental level, and so, in chapter 6 I show a hierarchical modelling technique that sheds some light on the degradation of these record setting solar cells.

Acknowledgments

My time here at UC Davis has been a time of great personal and professional growth, and I attribute a great deal of my development to those I've met along the way. The most powerful force in my development was certainly my advisor, Gergely Zimanyi. Gergely has gone far beyond what an advisor is expected to do, he views himself as a mentor to his students in many ways, and I think that he succeeds incredibly in all of them. I can honestly say that I don't think I would have been able to make it all the through without his unique, powerful brand of mentorship.

I further would like to thank my collaborators within the Zimanyi group, Luman Qu, Davis Unruh, Miguel Alba, Michael Kovtun, and Zeke Zhao. Each of them played a part in the various papers contained within this thesis, and their help in the physics and outside of it has been invaluable to me.

I'd also like to thank my collaborators outside of the Zimanyi group that helped us more deeply understand the physics in all of the papers presented within this thesis. Because of the large number of people involved in the various papers, I will not list the names here, but know that you are all appreciated, again, thank you.

I'd further like to thank Professors Richard Scalettar and Dong Yu for their input on this thesis, their comments and suggestions are greatly appreciated and have greatly improved the quality of the presentation.

Finally, I'd like to thank my family and friends that helped me out along the way. There were several times during this journey that I would have been crushed without their support.

CHAPTER 1

Introduction

The world is moving in a direction that will require that green energy be adopted by a large percentage of the population. Traditional energy sources are simply not sustainable, so we need as many green options as we can to bring the planet back from the brink. One of the leading technologies in green energy is the photovoltaic cell. Currently photovoltaics are competitive in many regions with traditional energy sources, but their market penetration is not nearly enough to get us off the train towards self-destruction that we find ourselves on.

Generation I (currently highly marketable) photovoltaic technology appears to be nearing its efficiency saturation point. While there are many ways towards improving the figure of merit for marketability of photovoltaics, the dollar per Watt, I've decided to focus on just two of them: 1) improving the efficiency of solar cells and 2) reducing the degradation rate of solar cells. In order to do this, I have looked beyond generation I technology and ventured to better understand generation II and III (not yet highly marketable) technologies, the solar cells of tomorrow.

This broader thesis focuses primarily on two areas within improving solar cell efficiency. First, I look at understanding carrier transport in nanoparticle solids. The end goal of this work is being able to make statements about how to improve the electron mobility, and therefore the photovoltaic efficiency of such materials. Second, I look at understanding degradation in the world champion terrestrial solar cells, Heterojunction with Intrinsic Thin layer (HIT) cells. These cells already have the highest efficiency among cells that could reasonably be deployed at the scale and price point necessary for energy production on earth, however, they degrade twice as fast as generation I solar cells. This degradation is not well understood, and if it can be remedied such that HIT cells degrade only as fast as current generation I technologies, this would be roughly equivalent to improving the efficiency of HIT cells by about 1%, a very large improvement. In solar technology, there are several hierarchical levels that people frequently refer to when they talk about degradation and efficiency, the cell level, which refers to individual solar cells, the module level, which refers to a

collection of solar cells that are grouped together, these are the panels that you see on rooftops, and the system level, which includes essentially everything that goes into getting the energy from the sun to your home. This thesis is restricted to the cell level, though each level is extremely important for improving solar technology.

1.1. Nanoparticle Solar Cells

Traditional solar cells have a limit to their efficiency, and while we are not yet at that limit, we are coming closer and closer to that theoretical limit, and ideally, we'd like to find materials that don't fall prey to some of the loss mechanisms that go into the calculation of this theoretical maximum. At a very basic level, light from the sun excites electrons from the valence band into the conduction band, and with the help of a built in electric field, these electrons form a current. These electrons, however, can only be excited to the conduction band if the photons are energetic enough, any photons not energetic enough to cause this transition will not be absorbed by the material, and can be treated as a loss. The other major loss mechanism is thermal relaxation, where very high energy photons excite an electron deep into the conduction band, but the electron quickly thermalizes to the conduction band edge, losing all of the excess energy to phonons. These losses as a function of band gap are illustrated in figure 1.1. It turns out that some materials have properties that allow them to mitigate some of these losses, which is why they are of such great interest.

Colloidal semiconductor nanoparticles (NPs) are singularly promising nanoscale building blocks for fabricating mesoscale materials that exhibit emergent collective properties. Nanoparticle materials have been shown to exhibit several phenomena that are eminently useful in maximizing solar cell efficiency, particularly carrier multiplication, intermediate bands, and a tunable band gap [**2**,**3**]. First, I'd like to touch on the idea of a tunable band gap. Because of their small size, nanoparticles' electronic energy levels are closely related to their size, the larger the particle, the smaller the gap between states, this can be most easily seen by treating an electron of the nanoparticle as a particle in a box. Thus, by changing the size of nanoparticles, one also changes the band gap of nanoparticle solids. As shown in figure 1.1 there are different losses that dominate the cell for different bandgaps, and so one can use this tunability to optimize the cell for efficiency, this problem was

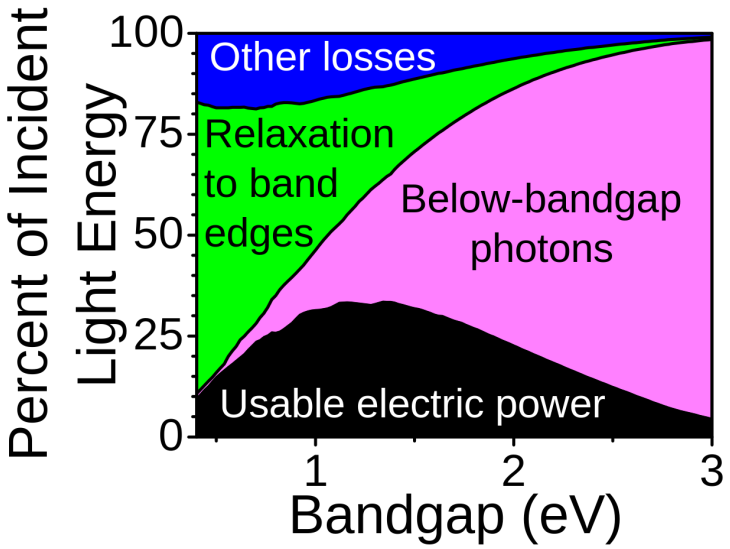

FIGURE 1.1. Usable solar energy as a function of band gap for traditional solar cells [**1**]. One can see that increasing the band gap reduces the relaxation losses but increases losses due to sub gap photons.

analyzed for traditional solar cells by Shockley and Queisser [**4**], and the efficiency limit is known as the Shockley-Queisser Limit. Next, I'd like to highlight some ways in which nanoparticle solar cells can, in principle, surpass the Shockley-Queisser Limit.

The idea behind carrier multiplication is that one photon can potentially generate more than one electron-hole pair, removing a significant portion of the thermal loss that comes from high energy photons. This happens when a high energy conduction electron or valence hole collides with a valence electron and promotes it to a conduction electron. This can only happen if the high energy carrier had enough energy to both excite the electron to conduction and remain in the conduction (or valence in the case of a hole) band. This is effectively the inverse process of a kind of recombination known as Auger recombination, in which an electron and hole recombine and rather than emitting a photon, as in band to band recombination, they give their energy to another electron. It has been shown that nanoparticle solids have significantly improved quantum efficiency relative to their bulk counterparts due to carrier multiplication, as can be seen in fig 1.2.

Intermediate bands are additional bands between the conduction and valence bands. These intermediate bands allow for lower energy photons, that would normally pass right through the material, to be absorbed by the material, allowing multiple low energy photons to excite an electron

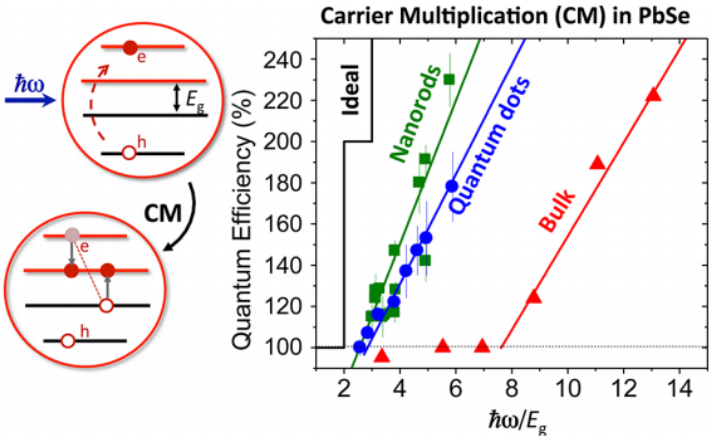

FIGURE 1.2. Sketch of carrier multiplication (left) and quantum efficiency (number of electron hole pairs per photon) vs. photon energy in units of the bandgap [**5**]. This mechanism allows for high energy photons to excite multiple carriers rather than just one.

first into the intermediate band, and then into the conduction band. Intermediate band solar cells have a much higher maximum theoretical efficiency (≈47% under one sun [**6**]) than "classical" solar cells (≈31% under one sun). We are primarily interested in one sun efficiency (to be contrasted with the higher efficiency of concentrated photovoltaics, that are able to operate at a higher voltage and current due to the higher illumination) because most photovoltaics currently operate without concentrator technology, as concentrator technology is really best suited to areas with high normal irradiance, and is generally on the decline in terms of deployment.

While the focus of my research is with respect to solar cells, for completeness, many of these same properties are useful for other opto-electronic devices such as light emitting diodes [**7**], and field effect transistors (FET) [**8**, **9**]. In fact, some of the research done in this thesis is done in the context of FETs because much of the underlying physical insights are transferrable to solar cells.

One of the central challenges in all of these applications is to improve the transport in the films, layers, and solids formed from nanoparticles. The value of hopping mobility in today's weakly-coupled insulating NP solids is typically low, $10^{-2} - 10^{-1}\text{cm}^2/\text{Vs}$. Various groups attempted to boost the mobility by boosting the inter-NP transition rate with a variety of methods, including: ligand engineering [**10**,**11**,**12**], band-alignment engineering [**13**,**14**], chemical-doping [**15**,**16**], photo-doping [**17**], metal-NP substitution [**18**], epitaxial attachment of NPs [**19**, **20**], and atomic layer

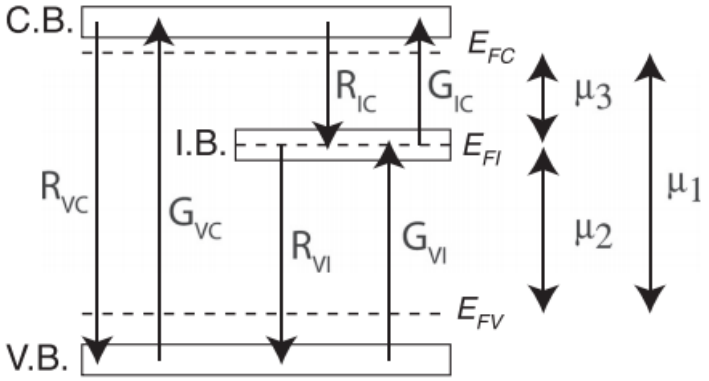

FIGURE 1.3. Schematic band diagram of intermediate band solar cell [**6**]. The intermediate band allows for sub gap photons to be absorbed that would normally just pass through the cell.

deposition methods [**21**]. Encouragingly, these efforts recently translated into progress, as NP films were reported to exhibit band-like, temperature-insensitive mobilities, with values approaching 10 cm^2/Vs at room temperatures.

A complete theoretical picture of transport in nanoparticle solids is not currently available. ab initio calculations cannot handle more than a few nanoparticles at once, so one needs to use higher level techniques to simulate transport among larger numbers of nanoparticles. In early papers in this field from the Zimanyi group, we used a hierarchical method culminating in a kinetic Monte Carlo (KMC) simulation to simulate transport through hundreds of particles. This is a significant step up from *ab initio* calculations, but it is still a far cry from the millions of nanoparticles present in experimental samples. In a later paper, I add a new hierarchical layer to this code to effectively simulate millions of nanoparticles. It should be noted, however, that the KMC-based simulations that our group employed don't include phase information, so the starting assumption is that the solids will be in an insulating phase, where transport is mediated by phonon assisted hopping from one nanoparticle to another. This means that even simulating millions of nanoparticles with KMC, we can only walk up to the doorstep of a metal-insulator transition, but never truly claim to describe metallic transport.

High conductivities require high mobilities and high carrier densities. However, introducing charge carriers in the nanoparticle solids (NP solids) is challenging. Due to intrinsic difficulties of

doping of NPs by impurity atoms [**22**], so far there have been only a limited number of experimental works achieving successful bulk doping [**23**, **24**, **25**]. This difficulty in doping arises from the fact that, unlike bulk materials, there is not actually a band that is spatially extended, but rather, there is a spatially confined set of distinct states. When the particles get small enough, the confinement energy exceeds the Coulomb energy which allows for dopant atoms, which are already able to ionize easily, transition into the nanoparticle states. This is a problem because a charged nanoparticle like this acts as a recombination center, and the carrier will be quickly absorbed and not participate in conduction.

Introducing carriers by applying a gate voltage V_G in a field effect transistor (FET) architecture is another promising approach. Several groups reported highly enhanced conductivities in FETs formed from Nanoparticle solids (NP-FETs). [**21**, **23**]. Because of this, many of the simulations I performed on nanoparticle solids, were done on structures with one or both of a FET geometry and a gate voltage. FETs are built such that while in operation, the current that is allowed to flow through the device is essentially only allowed to flow in an extremely narrow spatial band. Because of this, many of the simulations performed in this thesis on NP solids were done on quasi-2D structures, containing only 1 or 2 layers of nanoparticles, in order to best match the conditions of our experimental colleagues that perform mobility experiments on FET devices.

1.2. Heterojunction Solar Cells

Heterojunction (HJ) Si solar cells have world record efficiencies approaching 27%, due to the excellent surface passivation by their hydrogenated amorphous Silicon (a-Si) layer that leads to low surface recombination velocities and high open circuit voltages V_{OC}. A side view of a generic silicon HJ cell cell is shown in fig 1.4.

In spite of the impressive efficiency records, HJ Si cells have not yet been widely adopted by the market because of the perceived challenge that HJ cells may exhibit accelerated performance degradation, possibly related to their a-Si layer. Traditional crystalline Si (c-Si) modules typically exhibit about a 0.5%/yr efficiency degradation, primarily via their short circuit current I_{sc} and the fill factor FF, typically attributed to external factors, such as moisture ingress and increased contact resistance. In contrast, in 2018 two papers reported studies of how much fielded Si HJ

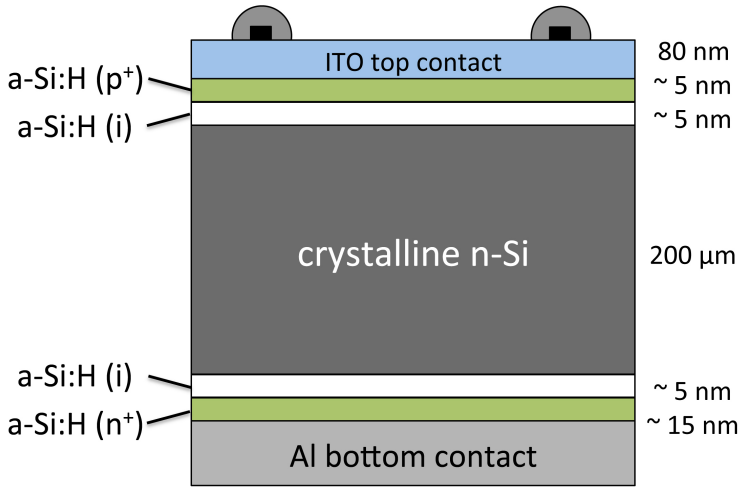

FIGURE 1.4. A cross section of a HIT solar cell [**26**]. The thin layer of amorphous silicon on top of the cell allows for higher open circuit voltages than standard silicon cells.

modules degraded over 5-10 years [**27**, **28**]. They reported degradation rates close to 1%/yr, about twice the rate of traditional cells. These papers pointed to a new degradation channel, the decay of V_{OC}, at a rate of about 0.5%/yr. The decay of V_{OC} suggests that the degradation is possibly due to internal factors, increasing recombination either at the a-Si/c-Si interface, or in the a-Si layer. Such increased recombination is typically caused by the increase of the electronic defect density.

These initial reports on fielded panels were followed up by in-laboratory analysis. The Bertoni group has studied the surface recombination velocity (SRV) at the a-Si/c-Si interface in HJ stacks. By applying a model for the recombination at the a-Si/c-Si interface to their temperature- and injection-dependent SRV data, they analyzed the degradation of the carrier lifetime and were able to attribute it to a loss of chemical passivation [**29**]. More recently, Holovsky et al. investigated ultrathin layers of hydrogenated amorphous silicon (a-Si:H), passivating the surface of crystalline silicon (c-Si) [**30**]. These authors applied highly sensitive attenuated total reflectance Fourier-transform infrared spectroscopy, combined with carrier lifetime measurements. They manipulated the a-Si/c-Si interface by applying different surface, annealing, and aging treatments. Electronic interface properties were discussed from the perspective of hydrogen mono-layer passivation of the c-Si surface and from the perspective of a-Si:H bulk properties. They concluded that both models have severe limitations and called for a better physical model of the interface [**30**].

Understanding the degradation of the passivated c-Si surface is important not only for understanding a-Si/c-Si heterojunction solar cells. The PV industry roadmap shows that among newly installed modules, the fraction of advanced Passivated Emitter/Rear Contact (PERC) modules will rapidly rise above 50% in the next 3 years. One of the advanced features of these PERC cells is the improved interface passivation with the application of elevated levels of hydrogen. However, the increased efficiency was accompanied by notable levels of degradation [**31**, **32**, **33**]. By experiments and by including all three charge states of hydrogen in their modeling, the authors speculated that the PERC cell degradation both in the dark and under illumination could be explained by the migration of and interaction between hydrogen ions in different charge states.

To summarize, the accelerated degradation of V_{OC} slows the market acceptance of the world-efficiency-record holder HJ Si modules, and impacts the introduction of the advanced PERC cells, thereby impacting the entire PV industry roadmap. Therefore, analyzing and mitigating this degradation process is of crucial importance.

1.3. Defects in Amorphous Si

Photoinduced degradation of a-Si under prolonged exposure to intense light was first studied, measured and modeled by Staebler and Wronski [**34**]. They reported that the degradation is characterized by a remarkably universal $t^{1/3}$ power-law temporal growth of the defect density. This behavior has become known as the Staebler-Wronski effect (SWE).

The SWE has been analyzed by several different methods. Some groups performed electron spin resonance (ESR) measurement on a-Si (a-Si:H) to experimentally detect the increase of the density of dangling bonds induced by light exposure [**35**, **36**, **37**]. Some of these papers also developed a phenomenological model to predict the SW defect-increase as a function of exposure time and light intensity. Other groups used the photocurrent method (PCM) to detect the change of defect density of a-Si under light exposure. In agreement with ESR experiments, PCM also revealed the increase of defect density under light exposure. While the ESR and PCM defect density measurements yielded analogous results, it is recalled here that they capture different type of defect states [**38**, **39**]. ESR detects all neutral defect states that only include dangling bonds (DBs), while PCM detects both neutral and charged defect states that include DBs and other types of defect states. Therefore

PCM measurements revealed that the origin of defect states might be a result of different type of general structural disorders beyond DBs. [**40**, **41**]

Recently, Wronski argued that three distinct defect states, A/B/C, are needed to account for all the data, instead of the standard single "midgap dangling bond" defect [**42**]. The A/B states are efficient electron recombination centers, while the C states recombine holes efficiently. Wronski speculated that these states are differentiated by their different structures: dangling bonds, mono- and divacancies, as also advocated by Smets. Other groups also analyzed their data in terms of three distinct states [**29**,**32**]. However, they focused on the alternative picture that the defect states may be the three charge states H+, H0, and H- of hydrogen. In addition to these experimental works, recent theoretical and computational papers also analyzed the defect states in a-Si, and they concluded that besides dangling bonds, highly strained bonds also contribute to midgap states significantly [**43**, **44**].

On the theoretical front, there have been a few models that attempt to explain the SWE. The hydrogen collision model suggests that mobile hydrogens in the amorphous silicon matrix "collide" and create metastable hydrogen complexes that leave behind additional dangling bonds [**45**] a cartoon of this process is shown in figure 1.5. There has also been a model put forward by Stutzmann et. al that suggests that recombination of electron hole pairs causes a restructuring of the amorphous silicon matrix that leads to new dangling bonds being formed [**36**]. While neither model has been completely corroborated by experiment, they do provide useful insights into possible channels for degradation to occur. They are also both able to reproduce the SWE $t^{\frac{1}{3}}$ defect density growth, despite their shortcomings, and it is possible that they each tell a part of the story.

To summarize, while a fair amount of progress has been achieved in characterizing defect generation in a-Si, its underlying mechanism and connection to the different types of structural disorder and defects is far from being settled and understood. The problem is still open to question, and in chapter 5, I will try to bridge this gap in understanding, at least partially, leaving a more complete bridging for future work.

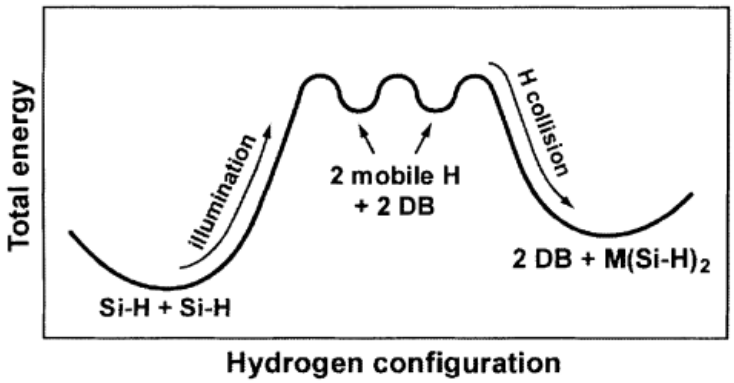

FIGURE 1.5. A cartoon of the hydrogen collision model mechanism [**45**]. Light elevates two bound hydrogens to two mobile hydrogens that carry dangling bonds with them. Eventually these mobile hydrogens collide, forming a higher energy metastable state that effectively left behind two dangling bonds.

CHAPTER 2

Commensuration Effects in Nanoparticle Solids

2.1. Introduction

Colloidal semiconductor nanoparticles (NPs) are singularly promising nanoscale building blocks for fabricating mesoscale materials that exhibit emergent collective properties. There is a growing interest to use NPs for numerous optoelectronic applications [**46**, **47**], including third generation solar cells [**2**, **3**] light emitting diodes [**7**], and field effect transistors (FET) [**8**, **9**].

One of the central challenges in all of these applications is to improve the transport in the films, layers, and solids formed from nanoparticles. The value of hopping mobility in today's weakly-coupled insulating NP solids is typically low, $10^{-3} - 10^{-2}$cm^2/Vs. Various groups attempted to boost the mobility by boosting the inter-NP transition rate with a variety of methods, including: ligand engineering [**10**,**11**,**12**], band-alignment engineering [**13**,**14**], chemical-doping [**15**,**16**], photo-doping [**17**], metal-NP substitution [**18**], epitaxial attachment of NPs [**19**, **20**], and atomic layer deposition methods [**21**]. Encouragingly, these efforts recently translated into progress, as NP films were reported to exhibit band-like, temperature-insensitive mobilities, with values approaching 10 cm^2/Vs at room temperatures.

High conductivities require high mobilities and high carrier densities. However, introducing charge carriers in the nanoparticle solids (NP solids) is challenging. Due to intrinsic difficulties of doping of NPs by impurity atoms [**22**], so far there have been only a limited number of experimental works achieving successful bulk doping [**23**, **24**, **25**].

Introducing carriers by applying a gate voltage V_G in a field effect transistor (FET) architecture is another promising approach. Several groups reported highly enhanced conductivities in FETs formed from Nanoparticle solids (NP-FETs). [**21**, **23**].

In NP-FETs, a notable issue is the spatial, layer-to-layer distribution of the added carriers. Mean-field analyses of the electron density and the conductivity of FETs [**21**, **48**], including Debye-Huckel estimates, as well as detailed experiments on PbSe NP-FETs [**49**], all conclude that electrons, introduced to the layered NP solid by the gate voltage V_G, occupy only the first couple layers closest to the gate [**50**].

This strongly confined spatial distribution of the carriers has the potential to profoundly effect the mobility and thus the conductivity. Most notably, it can lead to commensuration effects via the Coulomb-blockade mechanism. Such commensuration effects have been observed experimentally in CdSe NP solids [**51**], PbSe NP solids [**52**], and Si NP solids [**53**], among others.

Besides the obvious scientific interest in understanding the physics of commensuration, it is imperative to get these effects under control for optimizing NP-FETs for technical applications, as Coulomb blockade effects can substantially reduce or even zero out transport.

Important early steps in this direction were reported in the recent work of the Shklovskii group. [**50**, **54**] They analyzed the non-trivial evolution of the electron distributions in the first and second layers, and the resulting low-temperature conductivity, as the overall electron filling was varied. One of the key outcomes of this work was the theoretical demonstration of strong commensuration effects emerging. They were driven by the complex interplay of the long range Coulomb interaction and the other energy scales of the problem.

This important work was our motivation to explore the physics of commensuration in NP Solids. We focused our analysis on two previously unexplored directions. First, experimental evidence strongly suggests that the screening of Coulomb interactions is strikingly efficient in NP-FETs. [**55**] In some cases, the screening by the embedded NPs can be represented by a dielectric constant ϵ of the order of 10 or higher. Therefore, at least classes of NP-FETs are probably more faithfully modelled by concentrating on the short ranged, "on-site" Coulomb charging energy E_c, instead of keeping the entire long range form. This position is supported by the observed temperature dependence of the conductivities: at low temperatures, experiments often report Efros-Shklovskii type variable range hopping, pointing to the importance of keeping the long range part of the Coulomb interaction, whereas above $T \approx 50 - 80K$, the Efros-Shklovskii temperature dependence typically gives way to a simple activated form, suggesting that the long range portion of the Coulomb

interaction ceases to be crucial. Obviously, for solar and optoelectronic applications this second, higher temperature range is of primary interest.

Second, earlier papers did not concentrate on the mobility as a function of the electron filling FF, an experimentally relevant parameter, potentially tunable by the gate voltage V_G in NP-FETs. Instead, they studied the $1p^e - 1s^e$ energy splitting as the energy scale competing with Coulomb phenomena. In some NP-FETs, such as PbSe NP-FETs, this splitting can be as high as 200 meV, and thus may not be activable at the temperatures of interest. For both of these reasons, we expressly introduced the gate voltage V_G into our model, while dropping the representation of the $1p^e$ energy levels.

In this chapter, we adapt our previously developed Hierarchical Nanoparticle Transport Simulator (HiNTS) code to model bilayer NP solids (BNSs). HiNTS integrates the ab initio characterization of single NPs with the phonon-assisted tunneling transition model of the NP-NP transitions into a Kinetic Monte Carlo based simulation of the charge transport in NP solids.

Our main results include the following. (1) Starting with the model having an independent inter-layer energy offset Δ, (1.1) we observed the emergence of commensuration effects when the electron filling factors FF in both NP layers reached integer values. These commensuration effects were profound and consequential as they reduced the mobility by orders of magnitude. This reduction is much more substantial than the mobility reductions observed in the long range interaction case. (1.2) We showed the complexity of our model by demonstrating that different classes of commensuration effects emerge in different parameter regions, defining distinct dynamical phases. (1.3) We studied these commensuration effects in a five dimensional parameter space, as a function of the on-site charging energy E_C, the energy offset Δ, the disorder D, the electron filling factor, FF, and the temperature k_BT. We explored the dynamical phases in this 5D parameter space that were dominated by the different commensuration effects, and the phase boundaries between them.

(2) Second, we built on our independent energy offset model to describe NP-FETs by recalling that the Poisson equation relates the gate voltage V_G and thus the energy offset Δ to the electron filling factor FF. We modeled NP-FETs by implementing this Δ-FF relation, in effect simulating the NP-FETs as a reduced-dimensional subset of the independent Δ model. We found that commensuration effects analogous to those previously observed in the independent Δ model also

emerged in NP-FETs. This demonstrates the usefulness and paradigmatic nature of our findings in the higher dimensional parameter space. A word on terminology. In granular metals, a Coulomb blockade emerges during transport in neutral systems because when an electron leaves a neutral grain, it leaves a hole behind, while it charges the originally neutral target grain. The sum of the charging energies of the two grains combined with the electron-hole attraction blockades transport. This Coulomb blockade is present at all densities and is not sensitive to commensuration phenomena. [**56**, **57**, **58**]. However, this density-insensitive Coulomb blockade is not the subject of this chapter.

In contrast, the filling-driven Coulomb blockade, studied here, reduces transport only at commensurate fillings because all NPs the hopping electron intends to hop onto are already occupied by another electron that repels it, making the hops energetically unfavorable. In other words: the Coulomb blockade in neutral granular metals is driven by electron-hole attraction; whereas the filling-driven Coulomb blockade in NP solids is driven by electron-electron repulsion. This chapter focuses on studying this filling-driven Coulomb blockades. As mentioned above and demonstrated below, multi-layer NP solids exhibit a filling-driven Coulomb blockade in some regions of our five-dimensional parameter space, while in other regions the filling-driven Coulomb blockade is conspicuously absent at nominally commensurate fillings. The emerging dynamical phase diagram is therefore far from obvious and is thus worthy of study.

In some detail, in the simplest one-layer model, the suppression of transport by the filling-driven Coulomb blockade is natural. However, in our more complex bilayer NP Solid model, (a) the electrons can redistribute between the layers, thus *de facto* changing the fillings in each layer, and (b) the disorder can help the electrons to overcome the Coulomb barriers, and inter-layer offsets. In this more complex model, it is far from obvious where the blockaded regions will be located in the five-dimensional model-parameter space.

2.2. Simulation Methods

Recently, we have developed HiNTS, the **Hi**erarchical **N**anoparticle **T**ransport **S**imulator, as a multi-level Kinetic Monte Carlo computational platform, to study transport in nanoparticle solids. Previously, we have used HiNTS to study transport in NP-FETs [**59**], the metal-insulator transition

in NP solids [**60**], and binary NP solids systems [**61**]. For the present study, we have extended HiNTS and introduced new features, in order to study the commensuration effect in NP solids, in particular NP-FETs. The presentation and discussion of our results requires a brief description of the hierarchical levels of HiNTS. The details of our methods are provided in the Appendix.

(1) We adapted a k·p calculation of the energy levels of PbSe NPs in the diameter range of 5-7 nm. The theoretical results have been validated via comparison to optical experiments. [**62**] Our model also included the electron-electron interaction on the level of on-site/self-charging energy. This self-charging energy can be calculated by a variety of methods, including the semi-empirical pseudopotential configuration interaction method of Zunger and coworkers [**63**, **64**] and the tight-binding based many body perturbation theory method of Delerue [**65**]. In this chapter we report results with the latter approach, because it represents the details of the dielectric screening more realistically.

(2) On the next length scale of the order of 10 nm, we modelled the hopping transitions between neighboring NPs that are separated by twice a ligand length parameter. We incorporated into our model the Miller-Abrahams single phonon-assisted activated hoppings.

(3) On the hierarchically top length scale of hundreds to a few thousand nanometers, we generated an entire solid sample of the NPs, pair-wise coupled via the framework of step (2). We used the event-driven Molecular Dynamics code PackLSD [**66**] to obtain close packed (jammed) NP solids. Each sample contained several hundred NPs. We simulated the Bilayer NP Solids (BNS), or NP-FETs, by forming the NP solid in a simulation volume with a thickness of about two NP diameter. We determined whether the NPs belonged to the first or the second layer by tracking the z-coordinates of the NPs. To capture the naturally occurring randomness, the NP diameters were picked from a Gaussian distribution. This disorder in the NP diameters translated into a disorder of the NP energies with a width D.

(4) Finally, we simulated transport across the BNS/NP-FET by adapting and using our Extended Kinetic Monte Carlo (KMC) code that incorporated activated transitions [**59**, **67**] between all neighboring NPs. We injected electrons into the NP-FET to reach a predetermined electrons/NP density. Our central quantity of interest was the electron mobility. We always made sure that the voltage was sufficiently small to keep our simulations in the linear I-V regime.

The NP-NP separation (controlled by the ligand lengths), and the overall hopping attempt rate prefactor was selected such that the simulated mobilities were consistent with the experimental values, such as those from the Law group [**21**]. We systematically explored wide parameter regions, including that of temperature, disorder, electron density, and Coulomb interaction. For each parameter set, we simulated at least 40, typically several hundred samples.

2.3. Results and Discussion

To begin the exploration of the commensuration effects, we simulated a single-layer NP solid. Fig. 1 shows the mobility as a function of the electron filling factor FF, for two different, experimentally typical NP diameters of $d = 5.6$ nm, and $d = 6.5$ nm. It was assumed that the diameter d of each kind of NP had a Gaussian distribution around these mean values. Redoing the *ab initio* calculations of the NP energy levels, this diameter disorder translated into an energy disorder of width D. Visibly, the mobility shows a profound commensuration effect as the electron density per NP (e/NP), or filling factor FF, approaches integer values. Demonstrating the commensuration effect at integer fillings FF in the single-layer NP solid establishes the reference frame for the rest of our simulation work.

Figs. 2a-b illustrate the underlying physics of this commensuration-induced suppression of the mobility, as the filling FF approaches 1 from below. Fig. 2a shows how the HiNTS code evaluates the energetics of possible transitions for a selected electron (indicated by solid green), when surrounded by NPs that are already occupied by electrons, shown with black. Transition to any site already occupied comes at the additional energy cost of E_C, the charging, or on-site Coulomb energy. At low temperatures such energies are not available by thermal assistance, and the selected electron is blocked from executing this transition, as indicated by the red Xs. In the specific case of $FF \rightarrow$ integer, just about all target NPs are already filled with electrons, thus just about all NP-NP transitions are blocked. We refer to this phenomenon interchangeably as the filling-driven Coulomb blockade or commensuration-induced mobility minima. Its primary feature is the exponential suppression of the mobility at integer filling factors FF, as shown in Fig. 1, and more compellingly in Fig. 5a.

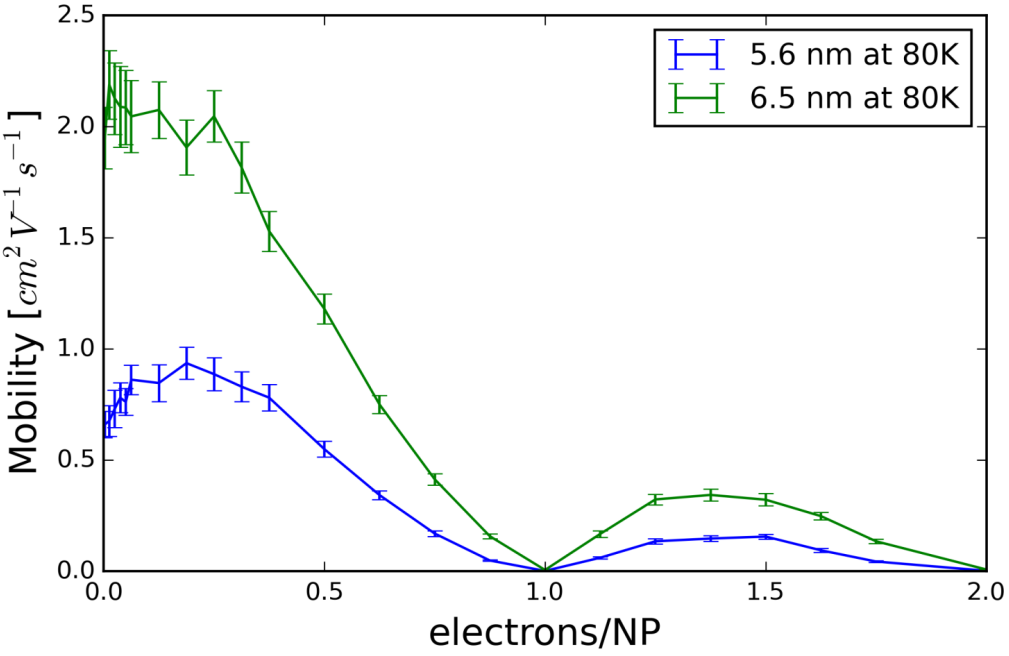

FIGURE 2.1. Mobility in single layer NP solid, exhibiting a clear commensuration-induced suppression. $E_C = 120$ meV, $k_BT = 80K$, $D(d = 5.6nm) = 55$ meV, $D(d = 6.5nm) = 45$ meV

Fig. 2b illustrates the limits of the commensuration induced by the filling-driven Coulomb-blockade. As the disorder D increases, and becomes comparable to E_C, even at commensurate fillings there will be NP-NP transitions where the net energy cost of the transition, of the order of $(E_C - D)$, will become comparable to the thermal energy k_BT, and thus more and more NP-NP transitions become possible even at $FF = 1$. This distinction is the basis to define separate dynamic phases of single-layer NP solids: for small disorder $D/E_C < 1$, the commensuration induces a Coulomb blockade, separated by a marked transition into a non-blockaded dynamic phase as the control parameter D/E_C exceeds a critical value of the order of 1. We will illuminate this argument with simulations in relation to Fig. 7 below.

With this preparation, we now move to the study of Bilayer Nanoparticle Solids (BNS). Fig. 3 illustrates a typical BNS sample. The sample was prepared by PackLSD, as described above in step (3) of HiNTS. The blue/red colors indicate whether a NP belongs to the lower or the upper layer. From here on, the nanoparticles are all selected from a Gaussian distribution of diameters

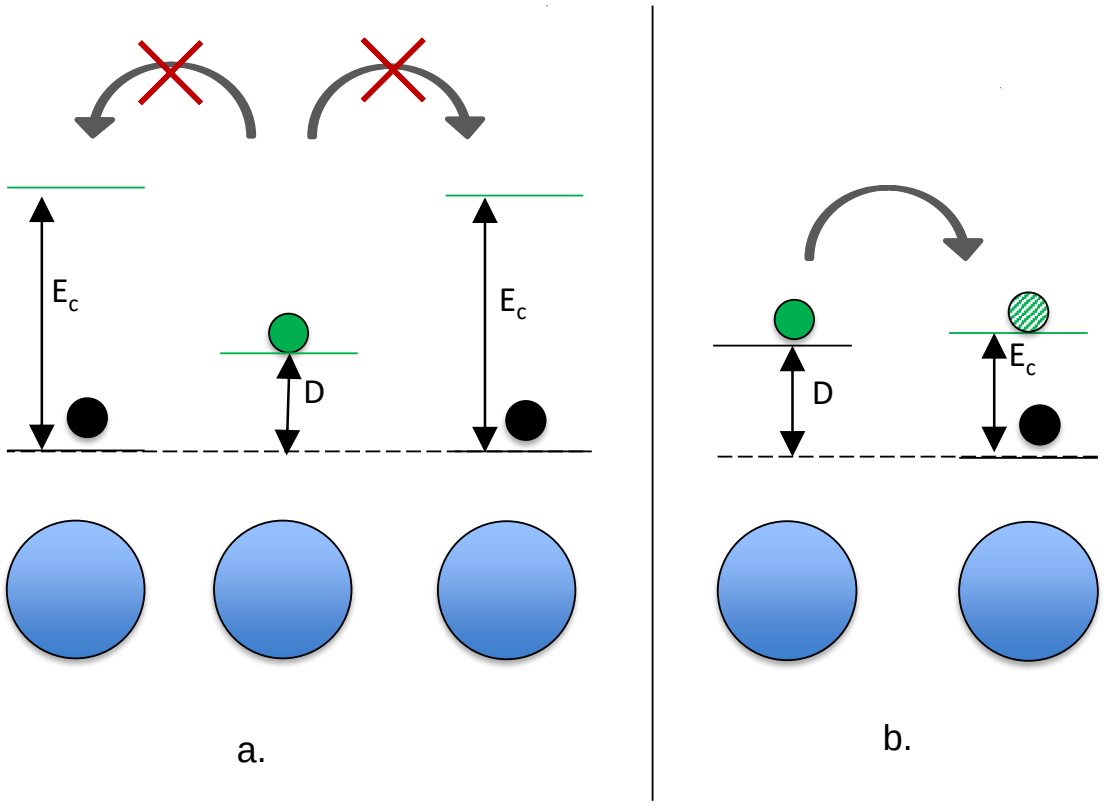

FIGURE 2.2. The physical mechanism of the Coulomb blockade driving the commensuration-induced suppression of the mobility.

with mean of $d = 6.5$nm and a width that translates to an energy disorder of D, typically chosen to be $D = 45$meV.

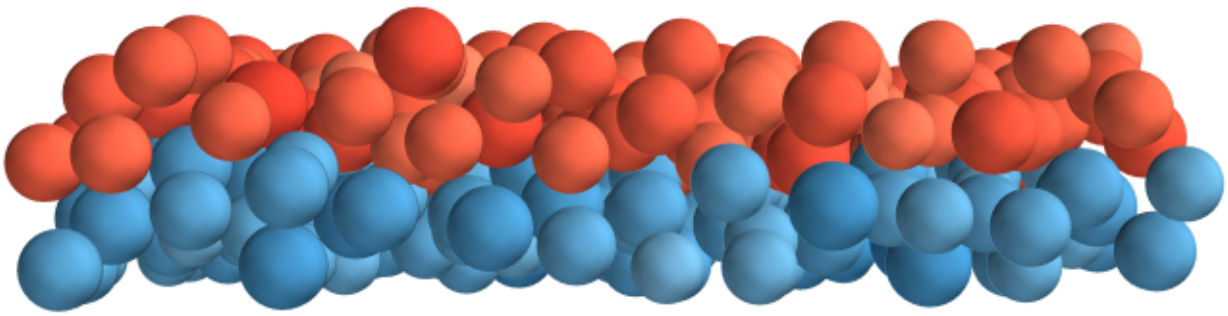

FIGURE 2.3. Illustration of a simulated bilayer Nanoparticle solid.

Fig. 4 shows the energy landscape in a BNS. In our model, there is an inter-layer energy offset Δ, which can be caused by various effects, such as a bending of the energy of the conduction band CB or a fixed transverse electric field. This energy offset Δ is a new competing energy scale in the problem beyond E_C and D.

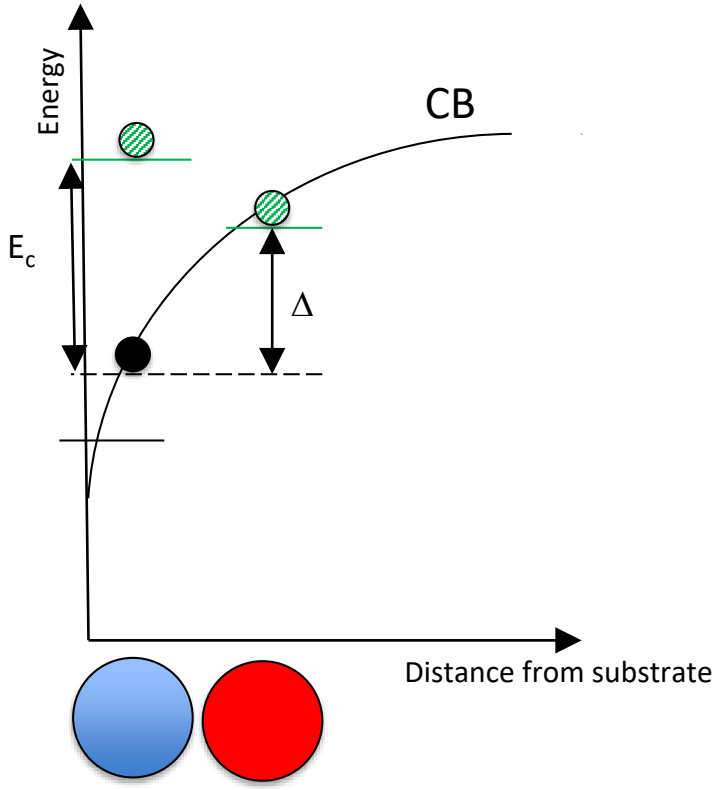

FIGURE 2.4. Energy landscape of a BNS with an inter-layer energy offset Δ.

Fig. 5a illustrates the mobility of a BNS as a function of the nominal electron filling factor per layer $FF = e/(NP/layer)$, for different energy offsets Δ. As an example, a BNS in which each layer has 200 NPs, will reach $FF = e/(NP/layer) = 1$ when filled by 200 electrons.

Fig. 5a shows that the mobility exhibits profound commensuration-induced minima at $FF = 1$ for $\Delta = 100$ meV and $\Delta = 500$ meV, but not at $\Delta = 20$ meV and $\Delta = 40$ meV; while at $FF = 2$ surprisingly, for $\Delta = 20$ meV, $\Delta = 40$ meV, and $\Delta = 500$ meV, but not at $\Delta = 100$ meV. The log scale shows convincingly that the mobility is exponentially suppressed by 2-3 orders of magnitude relative to the mobilities at non-commensurate FFs.

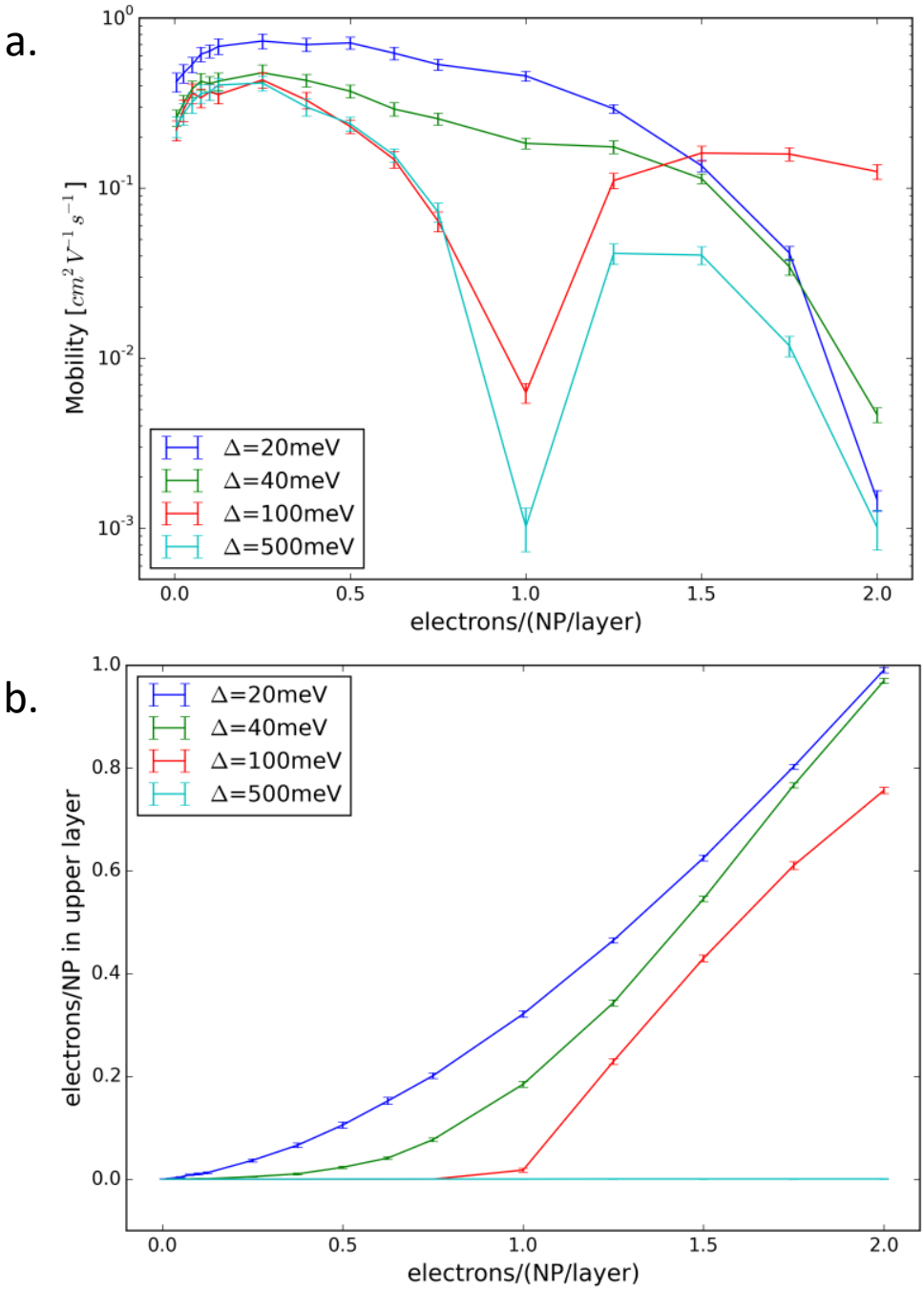

FIGURE 2.5. Mobility as a function of the filling factor FF. $E_C = 120$ meV, $k_bT = 7$ meV, and $D = 45$ meV. Energy offset Δ is varied from 20 meV to 500 meV.

Δ [meV]	20	40	100	500
FF_{upper}	0.30	0.20	0.02	0
FF_{lower}	0.70	0.80	0.98	1
Commensurate	No	No	Yes	Yes

a. $FF = 1$

Δ [meV]	20	40	100	500
FF_{upper}	0.99	0.97	0.77	0
FF_{lower}	1.01	1.03	1.23	2
Commensurate	Yes	Yes	No	Yes

b. $FF = 2$

TABLE 2.1. Summary of commensuration effects at $FF = 1$ and $FF = 2$.

The intriguing complexity of the BNSs is evidenced by the remarkable fact that the commensuration effects emerge at *different values of the energy offset* Δ for $FF = 1$ and for $FF = 2$. This is the result of the multi-dimensional competition of the energy scales, as explained next.

To set the stage, Fig. 5b shows FF_{upper}, the electron/NP Filling Factor specifically for the upper layer of the BNS, as a function of FF, the filling factor of the overall BNS. For $FF \leq 1$, for $\Delta = 100$ meV and $\Delta = 500$ meV, $FF_{upper} = 0$ up to $FF = 1$, i.e. all electrons remain in the lower layer up to $FF = 1$.

For $FF \geq 1$, FF_{upper} rises for $\Delta = 100$ meV, but stays put at $FF_{upper} = 0$ for $\Delta = 500$ meV. Finally, for $\Delta = 20$ meV and $\Delta = 40$ meV, FF_{upper} does not show any commensuration effect at $FF = 1$, but evolves towards the commensurate value $FF_{upper} = 1$, as FF approaches 2. These filling commensuration phenomena are summarized in Table I.a.

Fig. 6 explains the observations above. Figs. 6a-b are relevant for $FF = 1$, whereas Figs. 6c-d are relevant for $FF = 2$. Fig. 6a shows that when the energy offset Δ is much larger than the disorder $D = 45$ meV, for example $\Delta = 100$ meV or $\Delta = 500$ meV, then, as the electrons are filled into the BNS, they all remain in the lower NP layer. For $FF \leq 1$, the electrons do not doubly occupy the NPs, so the charging energy E_C does not enter into the competition of energy scales yet. This explains why FF_{upper} remains zero for $FF \leq 1$ for the higher energy offsets of $\Delta = 500$ meV and $\Delta = 100$ meV.

Since the competition of Δ and D confines all electrons into the lower layer, the charging energy E_C induces pronounced commensuration-induced mobility minima at $FF = 1$ for these high energy offsets, as shown by the blocked NP-NP transition, shown with a red X. Zooming in

on the mobility values at the commensuration-induced minima at $FF = 1$, Fig. 5a shows that the mobility minimum is lower for $\Delta = 500$ meV than for $\Delta = 100$ meV. This is because $\Delta = 500$ meV confines the electrons to the lower layer more effectively, as documented by Table I.a as well. Fig. 6b shows the complementary case of lower, 20 meV and 40 meV values of the energy offset Δ. For these lower offsets, the 45 meV disorder D is capable of overcoming the energy offset Δ and promoting the electrons from the solid green state on the blue, lower layer NPs to the shaded green state on the red, upper layer NPs, as shown by the allowed NP-NP transition. The possibility of freely transitioning between the lower and upper NP layers increases FF_{upper} to non-zero values, thus making the electron density non-integer in both NP layers. Since only integer Filling Factors activate the Coulomb blockade, these non-integer filling factors wash out the commensuration-driven mobility minima. This explains the disappearance of the commensuration effect in the blue and green curves of the mobility at $FF = 1$.

Figs. 6c-d are helpful to analyze how the physics of commensuration changes for $FF = 2$. For these higher fillings, (blue) NPs in the lower layer are often doubly occupied, as shown. Typical values of the charging energy E_C for isolated NPs are about 120 meV, considerably greater than the disorder. Therefore, the charging energy $E_C \approx 120$ meV replaces the disorder $D \approx 45$ meV, as the primary energy scale competitor to the offset Δ.

Fig. 6c is most relevant for the large energy offset of $\Delta = 500$ meV. Here, even an $E_C = 120$ meV is not capable of promoting electrons into the upper layer. Therefore, FF_{upper} remains zero even as FF grows from 1 to 2, as confirmed by Fig. 5b. By this mechanism, at $FF = 2$, the filling factors for both layers reach integer values, $FF = 2$, and $FF_{upper} = 0$, thus the Coulomb blockade once again drives a commensuration-induced effect: an exponentially suppressed mobility minimum.

Fig. 6d shows that the physics changes as the energy offset is reduced to $\Delta = 100$ meV. At this value, Δ is reduced to a level comparable to the charging energy E_C, thus freeing up the electrons to transition between layers. Fig. 6d shows that the energy of a (green) electron, residing on a (blue) NP in the lower layer, is lifted by the Coulomb repulsion from a (black) electron on the same NP, making the green electron capable of reaching the shaded green electron state on a (red) NP in the upper layer. Notably, since the energy offset and the charging energy are comparable,

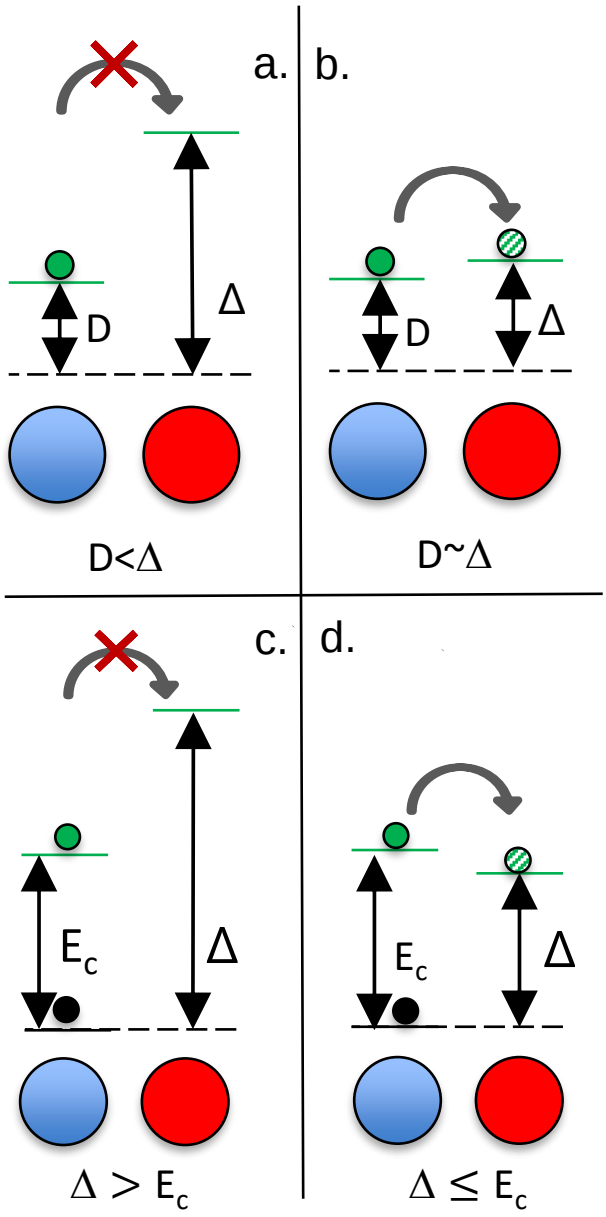

FIGURE 2.6. Energy diagrams to contextualize the various parameter regimes. (a.) illustrates $FF = 1$, $\Delta = 500$ meV and $\Delta = 100$ meV. (b.) illustrates $FF = 1$, $\Delta = 40$ meV and $\Delta = 20$ meV. (c.) illustrates $FF = 2$, $\Delta = 500$ meV. (d.) illustrates $FF = 2$, $\Delta = 100$ meV, $\Delta = 40$ meV and $\Delta = 20$ meV. In all cases $E_C = 120$ meV, $k_BT = 7$ meV and $D = 45$ meV.

the spatial distribution of the electrons spreads out over the two layers. This is captured by the FF_{upper} assuming a non-integer, non-commensurate intermediate value in Table I. This explains why the mobility does not exhibit a commensuration-induced minimum.

Finally, for even lower energy offsets $\Delta = 20$ meV and 40 meV, Δ is markedly smaller than E_C. This not only makes it possible for the electrons to leak into the upper layer, much rather it forces the electrons to do so. This is the driver of FF_{upper} actually reaching 1 as FF approaches 2. Since the filling factors of each layer reach integer values at $FF = 2$, the Coulomb blockades once again drive commensuration-induced mobility minima, as shown in Fig. 5a.

We note, that the commensuration-induced physics is markedly different for the different cases. For $FF = 1$, the upper layer does not play any role. For $FF = 2$ and $\Delta = 500$ meV, the NPs in the lower layer are doubly occupied, and the upper layer plays no role. Finally, for $FF = 2$ and $\Delta = 20$ meV and 40 meV, the upper and lower layer play a largely symmetric role. These regimes are dominated by different physics, and therefore can be identified as different dynamical phases of the BNS. The latter two, for example, are separated by a phase boundary around $\Delta \approx E_C$, where the competing energy scales are comparable. This washes out the commensuration effects, and serves as an effective phase boundary between the dynamical phases, as long as both remain large compared to D. The commensuration phenomena for the filling factor $FF = 1$ are summarized in Table I.a.

The commensuration phenomena for the filling factor $FF = 2$ are summarized in Table I.b. The complexity of the model is on full display in that the commensuration effects at $FF = 1$, as shown in Table I.a, are reversed relative to $FF = 2$ for 3 of the 4 values of Δ, as shown in Table I.b. The primary driver of these reversals is that the energy scale that is the primary competitor of Δ switched from the disorder D at $FF = 1$, to the charging energy E_C at $FF = 2$.

Up to now the model was analyzed by scanning the energy offset Δ and the filling factor FF, while keeping the charging energy E_C constant. An informative complementary parameter scan is shown in Fig. 7, where the charging energy E_C is scanned, while keeping the energy offset Δ constant. In all curves shown, $\Delta = 500$ meV. Therefore, all electrons are confined into the lower NP layer, and the physics is determined by the competition of the charging energy E_C and the disorder D. The blue curve shows the mobility at $E_C = 120$ meV, the same as the lowest curve in Fig. 5a. This parameter set was selected as it shows commensuration-induced mobility minima *both* at $FF = 1$, and at $FF = 2$. The relevant energy diagram is illustrated in Fig. 2a, showing that

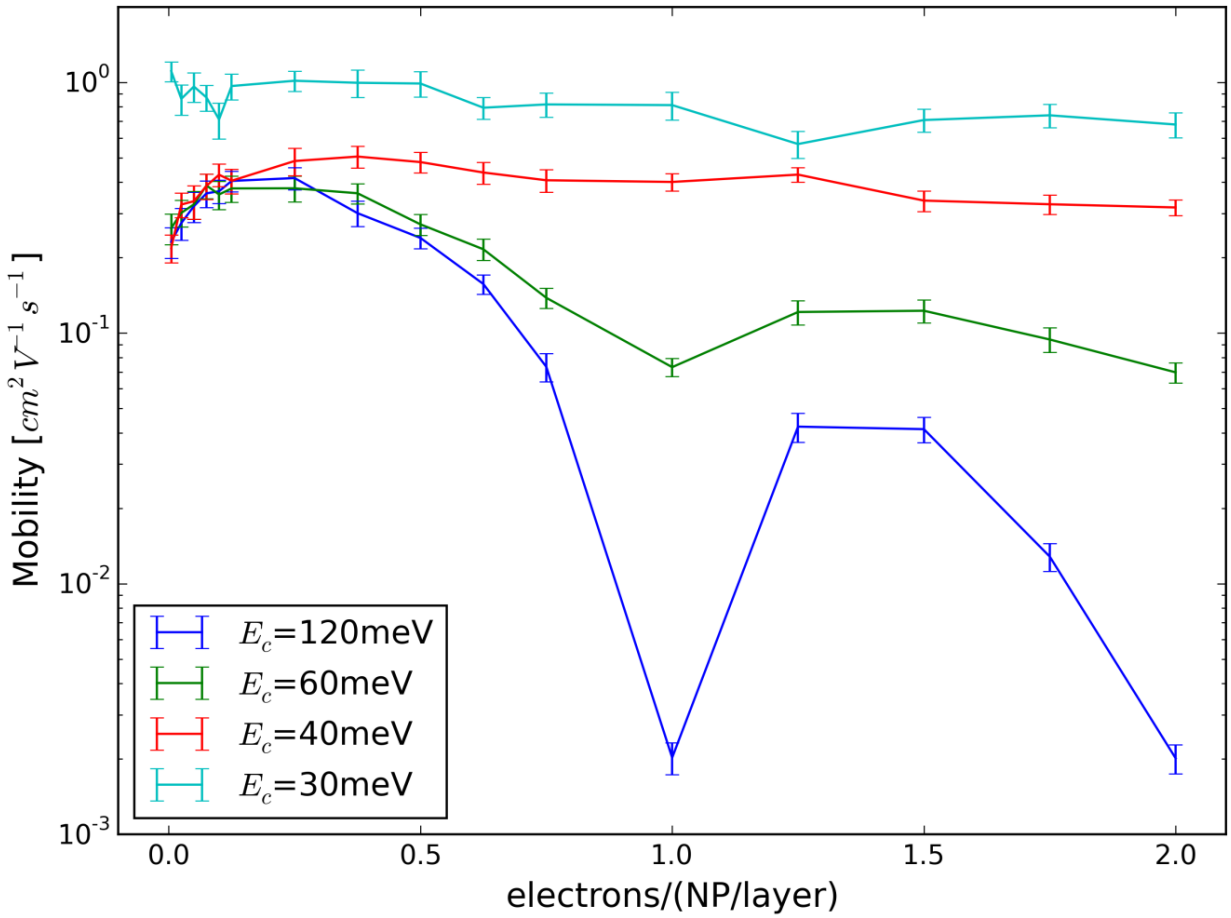

FIGURE 2.7. Fixed Δ, different E_C: $\Delta = 500$ meV, $k_BT = 7$ meV, and $D = 45$ meV.

the competing energy scale of the disorder D can not help the electrons to overcome the Coulomb blockade either at $FF = 1$ or at $FF = 2$.

As the charging energy is reduced to $E_C = 60$ meV, the depth of the mobility minima at $FF = 1$ and at $FF = 2$ are greatly reduced. Fig. 2b explains this as follows. At $E_C = 60$ meV, the disorder D, more precisely, the disorder D, augmented by the thermal energy to $D + k_BT$, becomes comparable to E_C, and thus capable of boosting the electrons to partially overcome the Coulomb blockade within the first layer. Upon further reduction to $E_C = 40$ meV and 30 meV, the mobility minima are completely smoothed out, as the disorder becomes the dominant energy scale, and the charging energy is unable to hinder transport anymore.

DCM	$FF(lower)$	$FF(upper)$
$FF = 1$		
$FF = 2$		

TABLE 2.2. Dynamic Commensuration Matrix **DCM** order parameter of the dynamical phases of the BNS model.

The above specific scans of the multidimensional parameter space demonstrate that the competition of the main physical processes gives rise to distinct dynamical phases of the model. Next, we create a comprehensive phase diagram of these dynamical phases in the D-Δ-E_C space by performing a systematic 2 dimensional raster scan of the D/E_C vs. Δ/E_C space. At each point of this raster scan we performed a scan with the filling factor FF and determined whether the BNS exhibited a well-defined mobility minimum at the two potential locations of commensuration effects: at $FF = 1$, or at $FF = 2$, or both. We adopt a "Dynamic Commensuration Matrix" **DCM** order parameter to characterize the dynamical phases through their filling factors as follows:

This **DCM** order parameter cross-references the nominal filling factor FF with the actual filling factor $FF(upper)$ of the upper layer, and $FF(lower)$, that of the lower layer at the two potential locations of commensuration effects: at $FF = 1$, and $FF = 2$. The top row of the **DCM** order parameter represents $FF(lower)$ and $FF(upper)$ at $FF = 1$ nominal filling, the bottom row the same fillings at $FF = 2$. Table II shows what the **DCM** looks like in matrix form. Since each entry is determined by position in phase space, we have left the example blank, and we note the maximum value of each entry is determined by the filling factor.

When the top row of the **DCM** contains the integers (1,0), then the nominal commensuration at $FF = 1$ indeed induces commensuration in the top and bottom layers, and thus the BNS exhibits commensuration-induced mobility minimum. In contrast, when the top row of the **DCM** contains non-integers, shown in the diagram as (1-n, n), then the competing physical processes smooth out the nominal commensuration, and the BNS does not exhibit mobility minima.

Analogously, when the bottom row of the **DCM** contains the integers (1,1) or (2,0), then the nominal commensuration at $FF = 2$ indeed induces commensuration in the top and bottom layers, and thus the BNS exhibits a commensuration-induced mobility minimum. In contrast, when the bottom row of the **DCM** contains non-integers, shown in the diagram as (2-n, n), then the

competing physical processes smooth out the nominal commensuration, and the BNS does not exhibit mobility minima.

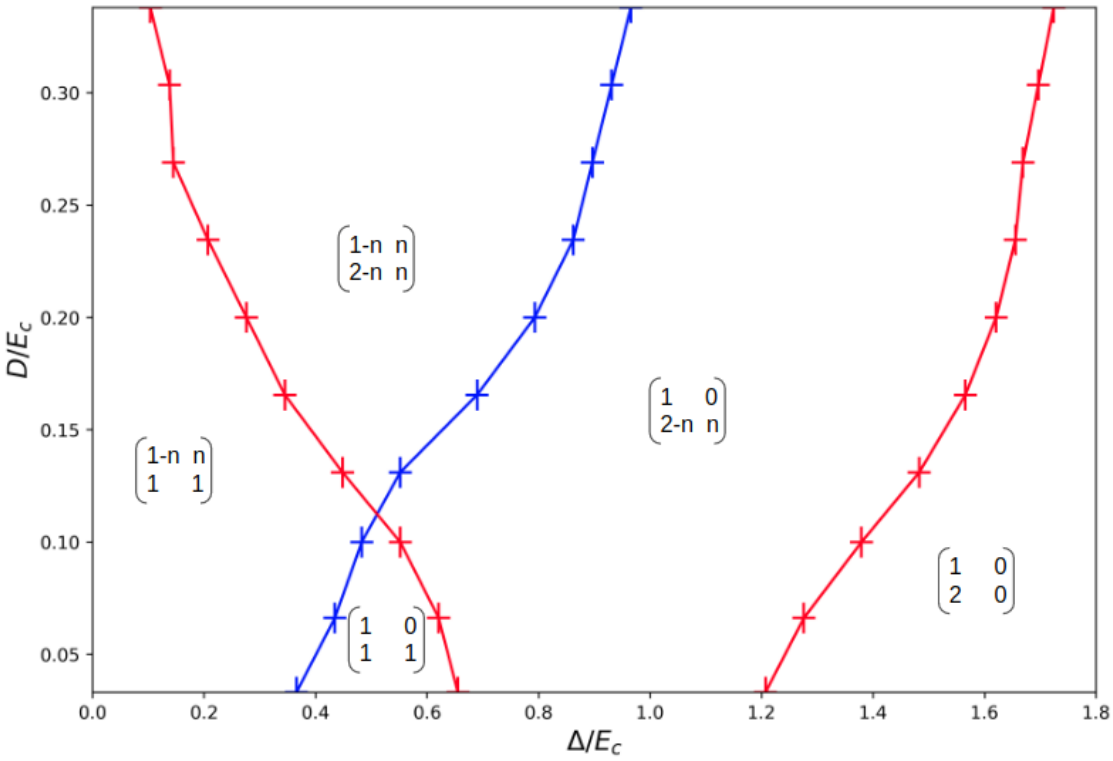

FIGURE 2.8. Dynamic phase diagram, capturing the dynamics of the BNS at the two filling factors $FF = 1$ and $FF = 2$ in terms of the Dynamic Commensuration Matrix **DCM**.

The rich information coded in the **DCM** Dynamical Commensuration Matrix order parameter can be condensed into a simpler Dynamical Commensuration Vector **DCV**. The upper element of the **DCV** only indicates whether at $FF = 1$ the dynamical phase exhibits a mobility Minimum At Commensuration: "M"; or not: "No-M". The lower element of the **DCV**, only indicates whether at $FF = 2$ the dynamical phase exhibits a mobility Minimum At Commensuration: "M"; or not: "No-M". With this convention, the five phases of Fig. 8 are the following:

(a) The left-most phase with the lowest Δ/E_C, having a **DCM** = (1-n, n)/(1, 1), where the lower row of the **DCM** matrix is shown after the "/", is described by a **DCV** = (NoM/M), the lower **DCV** vector element also shown after a "/" for consistency.

DCM	**DCV**
$\begin{pmatrix} 1-n & n \\ 1 & 1 \end{pmatrix}$	$\begin{pmatrix} NoM \\ M \end{pmatrix}$
$\begin{pmatrix} 1-n & n \\ 2-n & n \end{pmatrix}$	$\begin{pmatrix} NoM \\ M \end{pmatrix}$
$\begin{pmatrix} 1 & 0 \\ 1 & 1 \end{pmatrix}$	$\begin{pmatrix} M \\ M \end{pmatrix}$
$\begin{pmatrix} 1 & 0 \\ 2-n & n \end{pmatrix}$	$\begin{pmatrix} M \\ NoM \end{pmatrix}$
$\begin{pmatrix} 1 & 0 \\ 2 & 0 \end{pmatrix}$	$\begin{pmatrix} M \\ M \end{pmatrix}$

TABLE 2.3. The Mapping of the **DCM** Dynamic Commensuration Matrix onto the **DCV** Dynamic Commensuration Vector.

(b) The phase with higher Δ/E_C and higher D/E_C, having a **DCM** = (1-n, n)/(2-n, n), is described by a **DCV** = (NoM/NoM).

(c) The phase with similar Δ/E_C but lower D/E_C (the small upward-pointing triangle based on the $\Delta/E_C = 0.4 - 0.6$ interval), having a **DCM** = (1, 0)/(1, 1), is described by a **DCV** = (M/M).

(d) The phase with yet higher Δ/E_C, having a **DCM** = (1, 0)/(2-n, n), is described by a **DCV** = (M/NoM).

(e) The phase with the highest Δ/E_C, having a **DCM** = (1, 0)/(2, 0), is described by a **DCV** = (M/M).

It is instructive to review the phase diagram from the complementary vantage point of the phase boundaries.

(1) The blue boundary separates dynamic phases of the BNS that differ by the commensurative behavior at $FF = 1$, but not at $FF = 2$. Indeed, for low energy offset Δ/E_C, the electron fillings in the (lower, upper) layers are (1-n, n), thus the BNS is in a non-commensurate dynamic phase that does not exhibit mobility minima at $FF = 1$. For high Δ/E_C, the electron fillings in the (lower, upper) layers are (1, 0), thus the BNS is in a commensurate dynamic phase that does exhibit mobility minima at $FF = 1$. Thus, crossing the blue phase boundary by increasing Δ/E_C is a dynamic phase transition from a phase in which the BNS does not exhibit mobility minima

at $FF = 1$ to a phase in which it does. For completeness, across the blue phase boundary, the commensurative behavior of the BNS does not change at $FF = 2$.

(2) The red boundary separates dynamic phases of the BNS that differ by the commensurative behavior at $FF = 2$, but not at $FF = 1$. Indeed, for low energy offset Δ/E_C, the electron fillings in the (lower, upper) layers are (1, 1), thus the BNS is in a commensurate dynamic phase that does exhibit mobility minima at $FF = 2$. For medium Δ/E_C, the electron fillings in the (lower, upper) layers are (2-n, n), thus the BNS is in a dynamic phase that does not exhibit mobility minima at $FF = 2$. Finally, for high Δ/E_C, the electron fillings in the (lower, upper) layers are (2, 0), thus the BNS is again in a dynamic phase that does exhibit mobility minima at $FF = 2$. Thus, crossing the red phase boundary from low to medium Δ/E_C is a dynamic phase transition from a phase in which the BNS does exhibit mobility minima at $FF = 2$ to a phase in which it does not. Further, crossing the red phase boundary from medium to high Δ/E_C is a dynamic phase transition from a phase in which the BNS does not exhibit mobility minima at $FF = 2$ to a phase in which it does again. This is an intriguing case of a reentrant phase diagram. Again for completeness, across the red phase boundaries, the commensurative behavior of the BNS does not change at $FF = 1$.

(3) Broadly speaking, for a given disorder, increasing the energy offset Δ/E_C at $FF = 1$ forces more and more electrons into the lower layer, eventually cutting off their ability to escape the Coulomb blockade. This tendency led to the formation of mobility minima at commensuration (M), as it forced all electrons into the lower layer. For $FF = 2$, the filling of the lower and upper layers evolved from the evenly distributed commensurate $(FF(lower), FF(upper)) = (1,1)$ to the moderately uneven and non-commensurate $(FF(lower), FF(upper)) = (2\text{-n},n)$, eventually to the fully uneven, commensurate $(FF(lower), FF(upper)) = (2,0)$, as $\frac{\Delta}{E_C}$ was increased.

(4) While we observed that increasing Δ/E_C induced complex phase transition sequences, from more commensurate to less commensurate, followed by again to more commensurate, the trends with increasing disorder D/E_C were straightforward: more disorder moved the BNS from more commensurate towards less commensurate. Every time when either a blue or red phase boundary was crossed with increasing D/E_C (vertically), commensuration was lost either at $FF = 1$, or $FF = 2$. The physics behind this is natural: increasing disorder can smooth out the energy differences driven by Δ or E_C, thus smoothing out the mobility minima as well.

The independent energy offset model is a well defined statistical physical model, and thus worthy of study. Our extensive exploration created a comprehensive description of the phase diagram. Next, we turn our attention to the specific case of NP-based FETs, which have great potential for applications. We start by recalling that the energy offset Δ_{FET} is not a free parameter in NP-FETs, since it is induced by the transverse gate voltage, which also impacts the electron filling factor, FF as the two are related via the Poisson equation.

We use Eq. (6) of Shklovskii's 2014 paper [**50**] to represent this relationship. Broadly speaking, in the interval of interest, we take Δ_{FET} to be proportional to FF. Since additionally there are several material parameters in this equation that can vary from FET to FET, we carried out a set of simulations with varying proportionality constants.

Fig. 9 illustrates our results. We selected a set of proportionality constants between Δ and FF such that Δ_{FET} at $FF = 1$ assumed those values which we used for our fixed-Δ_{BNS} simulations in Fig. 5a. This choice created the closest analogy and thus comparability between the two sets of runs.

While the results in Fig. 9 and in Fig. 5a are not exactly the same, nevertheless they demonstrate the same paradigm. While broadly speaking, the Coulomb blockade tends to suppress the mobility at commensurate electron fillings, whether this suppression actually manifests itself depends in a non-trivial and intricate manner on the various parameters of the model. For some parameters, the NP-FET shows a suppression only at $FF = 1$, for others only at $FF = 2$, for some at both fillings, and for some at none at all.

To establish a relationship between the phase diagram of the independent Δ_{FET} BNS and the NP-FETs, we note that our BNS Dynamical Commensuration Vector **DCV** was defined by the presence or absence of mobility minima at the two filling factors $FF = 1$ and $FF = 2$ at the *same* Δ_{BNS}. In contrast, for NP-FETs, the NP-FET Dynamical Commensuration Vector **DCV** is defined by the presence or absence of mobility minima at the two filling factors $FF = 1$ and $FF = 2$ using their corresponding, *different* Δ_{FET}s. Thus, the two elements of the **DCV** have to be determined from information in the BNS phase diagram at the two different Δs that correspond to $FF = 1$ and $FF = 2$.

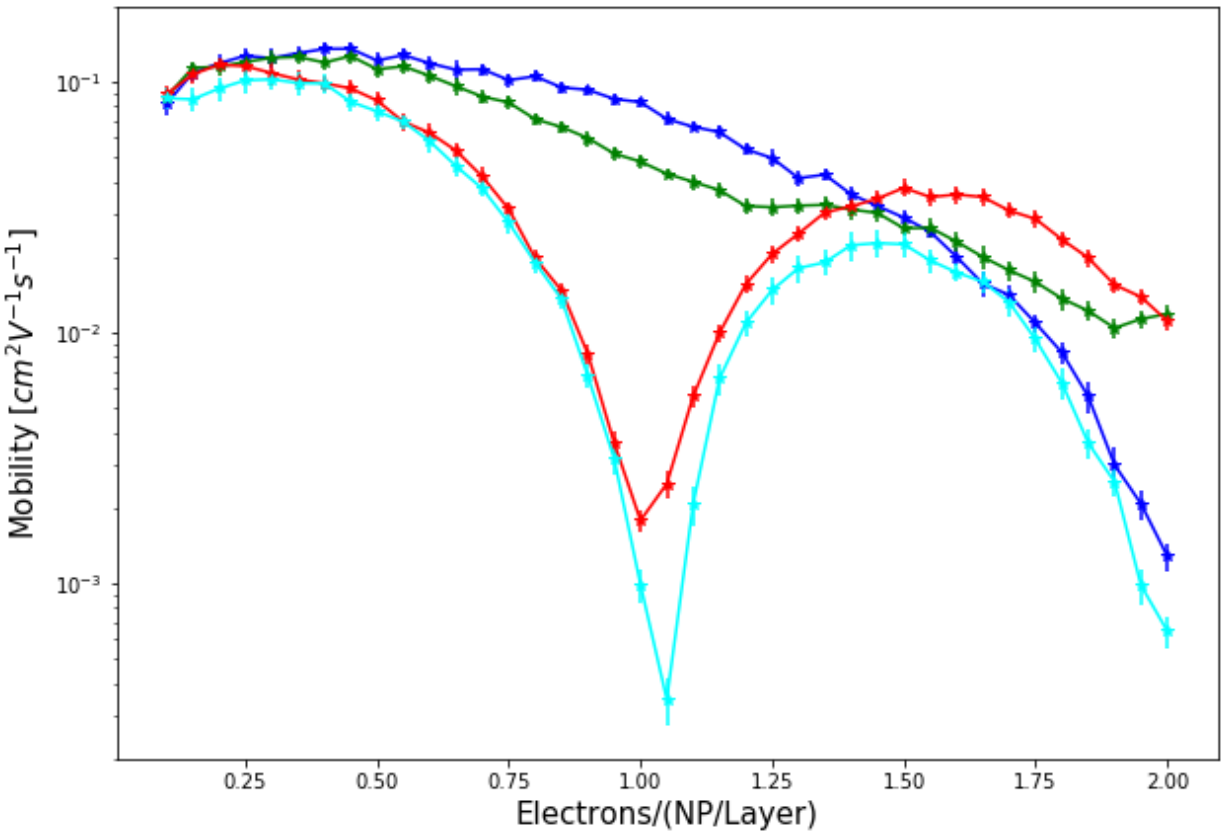

FIGURE 2.9. Mobility as a function of the electron filling factor FF. The 4 curves were generated by using 4 proportionality constants between the inter-layer energy offset Δ_{FET} and the filling factor FF such that Δ_{FET} was equal to the four Δ_{BNS} values used in Fig. 5a. at $FF = 1$

2.4. Conclusions

In this chapter, we adapted the previously developed Hierarchical Nanoparticle Transport Simulator (HiNTS) to simulate two models of interest: (1) Bilayer Nanoparticle Solids (BNSs) with an independently variable inter-layer energy offset Δ_{BNS}; and (2) Bilayer NP-FETs, where the inter-layer energy offset Δ_{FET} controlled the filling factor FF. HiNTS combines ab initio single NP modeling and NP-NP transition modeling into a Kinetic-Monte-Carlo-based simulation of the transport in BNSs and NP-FETs. Our main results included the following.

(1) We observed the emergence of commensuration effects when the electron filling factors in both NP layers reached integer values. These commensuration effects were profound as the on-site Coulomb blockade reduced the mobility exponentially close to zero, often by 2-3 orders of

magnitude. These observed reductions are to be contrasted with the limited mobility reductions observed in models with long range interactions.

(2) We noted that different classes of commensuration effects emerged for different parameter regions. The complexity of the physics was well-demonstrated by the fact that the commensuration effects were markedly different at filling factors $FF = 1$ and $FF = 2$: in some regions the mobility showed a minimum at $FF = 1$ but not at $FF = 2$, in some cases at $FF = 2$ but not at $FF = 1$, in some cases at both, and in some cases at neither.

(3) We systematically swept a two dimensional subspace $(\frac{\Delta}{E_C}, \frac{D}{E_C})$ of the parameter space to construct model's dynamical phase diagram. We introduced two order parameters, the Dynamical Commensuration Matrix **DCM**, and the Dynamical Commensuration Vector **DCV** to capture the presence or absence of mobility minima at $FF = 1$ and $FF = 2$ as the electron filling FF was swept.

We identified five separate dynamical phases of the model that demonstrate the richness of the emergent physics, driven by the competition of the several energy scales of the model. We developed an explanation for the presence or absence of mobility minima in each of these dynamic phases. We developed further insights by discussing the critical behavior as the various phase boundaries were crossed. Finally, we demonstrated the paradigmatic nature of our dynamical phase analysis by reporting that the patterns of the mobility minima and the rich commensurate behavior of the independently variable Δ_{BNS} BNS simulations were closely analogous to those of the NP-FET simulations, where the Δ_{FET} controlled the filling FF.

In closing, it is important to understand the commensuration effects in bilayer NP solids as in NP-FETs electron transport is confined to the first few NP layers adjacent to the substrate. In such confined spaces the Coulomb-blockade-induced commensuration effects tend to introduce profound blockades against electron transport. Such transport blockades can greatly hinder the usefulness and adoption of NP-FETs for opto-electronic applications. Our work intended to serve as a guide how to control, avoid and overcome transport blockades induced by the interplay of commensuration and Coulomb effects in NP-FETs and in bilayer NP solids.

2.5. HiNTS

Here we describe some of the details of the **Hi**erarchical **N**anoparticle **T**ransport **S**imulator, or HiNTS. HiNTS is, as the name suggests, a hierarchical code that starts at the atomic level and works up to the level of hundreds of nanoparticles. The *ab initio* levels (1)-(3) have been described in earlier publications in some detail [**59**, **60**], but will be briefly described as part of the fourth hierarchical layer below.

Here we describe fourth hierarchical layer, the Kinetic Monte Carlo (KMC) modelling. We introduced the KMC method to calculate mobilities of size- and lattice-disordered NP arrays. The semi-classical KMC consists of tabulating possible events and then selecting and executing events using a MC-like procedure. In particular, we decided to choose the BKL algorithm [**67**]. In the BKL method, each time step requires drawing two uniformly distributed random numbers between 0 and 1: r_1 and r_2.

The simulation is initialized and then the time-evolution starts by determining the rates Γ of possible events and then in each step we find the event j for which the below equation is satisfied.

$$\sum_{i=1}^{j-1} \Gamma_i < r_1 \Gamma_{\text{sum}} < \sum_{i=j+1}^{N} \Gamma_i$$

$$\Gamma_{\text{sum}} = \sum_{i=1}^{N} \Gamma_i$$

Then event j is executed and the time is advanced by drawing a second uniform random number:

$$\Delta t = \frac{-\ln(r_2)}{\Gamma_{sum}}$$

Finally, all of the events that may have changed are recalculated. Simulation is stopped when the measured physical observable reached a steady state value within a user-defined threshold.

We start the simulation by randomly placing charges on NPs with predefined density, and then we switch on the KMC algorithm. The mobility is measured as:

$$\mu_e = \frac{\text{harvested charges} \times L_z}{\text{t} \times \text{total number of carriers} \times F_{\text{ext}}}$$

where L_z is the length of the simulation box in the conducting direction. As stated above, we stop the simulation once the mobility reaches steady state: typically millions of time steps are needed to reach convergence. We used periodic boundary conditions in all three Cartesian directions and the number of harvested charges were measured by counting the net number of electrons crossing the $z = L_z$ plane.

For the regular hopping, we use Miller-Abrahams (MA) thermally assisted nearest-neighbor hopping or tunnelling. Other approaches include the Marcus theory of electron transfer [**68**], which also takes into account nuclear relaxation effects after the hopping, and the model developed by Nelson and Chandler that closely resembles Marcus theory. [**69**]

The validity and differences of these approaches have been analyzed in detail. [**70**, **71**]

$$\Gamma_{i\to j} = \begin{cases} \nu\beta_{ij} \exp\left(\frac{-\Delta E_{ij}}{k_b T}\right) & \text{if } E_i > E_j, \\ \nu\beta_{ij} & \text{if } E_i < E_j \end{cases} \tag{2.1}$$

The attempt frequency ν is assumed to be size and ligand independent and they set the time scale of the simulations. We chose ν in order to qualitatively match the order of magnitude mobitilies measured by the Matt Law group. [**21**] ΔE_{ij} is the energy difference between electron states of the ith and jth NPs. β is tunnelling amplitude and we evaluate it in the WKB approximation:

$$\beta_{ij}(E) = \exp\left(-2\Delta x\sqrt{\frac{2m^*(E_{\text{vac}} - E^{tunnelling})}{\hbar^2}}\right) \tag{2.2}$$

Here Δx is the NP-NP surface-to-surface distance, which in practice is chosen to be twice the ligand length. m^* is the effective mass of the tunnelling medium, which also depends on the effective mass of the barrier. Here we approximated m^* with the effective masses of electrons and holes in bulk PbSe. [**72**] An alternative approach is to use the Bardeen formula of tunnelling. [**73**] Here we refer everything to the vacuum level E_{vac} which is thus set to zero in all simulations. If the NP solid was embedded in a matrix this would represent the conduction band minimum of the embedding matrix. $E^{tunnelling}$ is the tunnelling energy. It is not immediately clear what energy should be used for $E^{tunnelling}$. In the spirit of the thermally assisted hopping approach of Chandler

and Nelson, E^{sp} was defined as an average of the energies of initial and final states of the hopping: $E^{tunnelling} = (E_a^{sp} + E_b^{sp})/2$, where E^{sp} is the single particle energy.

The energy difference ΔE_{ab} in Eq.2.1 is the barrier for hopping, which can be written as:

$$\Delta E_{ab} = \Delta E_{ab}^{sp} + \Delta E_{ab}^{F} + \Delta E_{ab}^{C}, \tag{2.3}$$

where the first term on the RHS is the difference in single particle energies of the initial and final states of the hopping:

$$\Delta E_{ab}^{sp} = E_b^{sp} - E_a^{sp}. \tag{2.4}$$

We used the energies from $k \cdot p$ perturbation theory as obtained by Kang and Wise [**62**]. We then applied a rigid shift to align the infinite diameter limit of the conduction band edge to the work function of bulk PbSe [**74**]. Figure 2.10 shows the energy levels as a function of NP diameter.

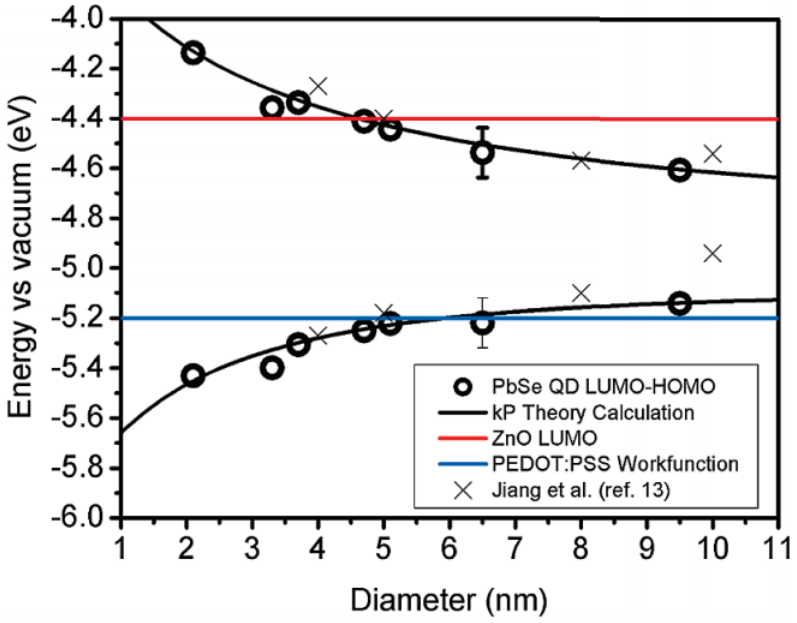

FIGURE 2.10. PbSe energy levels via $k \cdot p$ compared to experiment [**75**]

The second term on RHS of Eq. 2.3 is the contribution from the external voltage V:

$$\Delta E^F_{ab} = q\frac{V}{L_z}(z_b - z_a), \tag{2.5}$$

and

$$\Delta E^F_{ab} = \Delta \tag{2.6}$$

where L_z is the length of the NP solid in the conducting direction and z_b and z_a are the z position of the center of the NPs, and Δ is the energy difference associated with the transverse field. Care is exercised to make sure simulations are always in linear I-V regime. In particular, we set the external voltage so that $|E^F_{ab}| = 0.1kT(@30K)$. As mentioned in the main text, the disorder of the NP energies did not exactly average to zero in our samples, and thus generated an internal bias field. We eliminated this bias by always taking the pairwise average of the currents with a forward and a backward applied voltage.

Finally, the last term is due to the on-site Coulomb interaction:

$$\Delta E^C_{ab} = \Sigma^0_b + (n_b)\Sigma_b - (\Sigma^0_a + (n_a - 1)\Sigma_a) \tag{2.7}$$

where we introduced self energy, or the on-site charging energy: Σ^0 is the energy that needs to be paid upon the load of the first charge onto the neutral NP, while Σ is the energy it takes to load each additional charge. Both of them can be written in the form of $\Sigma(d_{\text{particle}}) = q^2/2C(d_{\text{particle}})$, where is C is the self-capacitance of the NP. Some groups also include here the mutual capacitance of the array further decreasing the self-energy. [**76**] The capacitance can be taken to be proportional to the diameter d. This is the approach we followed in our previous work and X_C was chosen according to the work of Zunger [**77**]. In this work, instead, we use Delerue's model [**65**], which provides a semi-analytic form for Σ and for Σ_0:

$$\Sigma^0 = \frac{q^2}{8\pi\epsilon_0 R}\left(\frac{1}{\epsilon_{\text{solid}}} - \frac{1}{\epsilon_{\text{NP}}}\right) + \frac{0.47q^2}{4\pi\epsilon_0\epsilon_{\text{NP}}R}\frac{\epsilon_{\text{NP}} - \epsilon_{\text{solid}}}{\epsilon_{\text{NP}} + \epsilon_{\text{solid}}} \tag{2.8}$$

$$\Sigma = \frac{q^2}{4\pi\epsilon_0 R}\left(\frac{1}{\epsilon_{\text{solid}}} + \frac{0.79}{\epsilon_{\text{NP}}}\right) \tag{2.9}$$

We used the Maxwell–Garnett (MG) effective medium approximation [**78**] to compute the dielectric constant of the entire NP solid. According to MG, the dielectric constant of the solid can be approximated as

$$\epsilon_{\text{solid}} = \epsilon_{\text{ligand}} \frac{\epsilon_{\text{NP}}(1+\kappa f) - \epsilon_{\text{ligand}}(\kappa f - \kappa)}{\epsilon_{\text{ligand}}(\kappa + f) + \epsilon_{\text{NP}}(1-f)} \tag{2.10}$$

where κ is 2 for spherical NPs and f is the filling factor.

Determining the dielectric constant of NPs is a field on its own [**63**, **79**]. The high frequency dielectric constant of bulk PbSe is 22.9 at room temperature, while the low frequency dielectric constant is 210 at room temperature. [**72**] It is not immediately clear whether the dielectric constant entering Eqs. 2.8,2.9,2.10 should contain ionic relaxation effects or not. Furthermore, the dielectric constant of a single NP is in principle one by definition. One can usually define an effective dielectric constant if the NP is big enough [**63**, **79**] but it turns out that such models, e.g. Penn Model [**80**], may not necessarily work for any kind of system. [**81**] In order to avoid making an uncontrolled approximation we decided to use the high frequency bulk dielectric constant of PbSe in the entire NP diameter range. [**77**]

Having defined the energetics of the NPs we can now discuss the transition, or hopping rates. The probability of an electron transferring from the initial NP a to the NP b is:

$$\Gamma_{ab} = \sum_{ij} \Gamma_{ij} g_i f_i(n_a) g_j (1 - f_j(n_b)) \tag{2.11}$$

where i/j denote kinetic energy levels, g_i/g_j are their degeneracy and f_i/f_j is the Fermi occupation function, n is the number of electrons on the respective nanoparticle.

Since we are assuming that the NP solid is weakly charged and the average charge per nanoparticle is less than the band degeneracy, the Fermi occupation functions can be replaced by their zero temperature limit and the sum over bands is limited to the first states:

$$\Gamma_{ab} = \sum_{\substack{i \in occ \\ j \in \text{unocc}}} \Gamma_{ij} g_i g_j \tag{2.12}$$

Following earlier works and assuming that our NP solid is not operating in the extremely confined size regime, the degeneracy g of the band edge states comes from the valley-degeneracy of bulk PbSe which is eight, including spin. Later work of Delerue showed that there is minor split of these states due to intervalley coupling. [**82**]

In order to investigate more realistic lattice disordered NP solids we set up random closed packed models by using an event-driven Molecular Dynamics code. [**66**, **83**] NP diameters (d) were drawn from a Gaussian distribution with an average diameter μ and standard deviation of σ:

$$f(d, \mu, \sigma) = \frac{1}{\sigma\sqrt{2\pi}} e^{-\frac{(d-\mu)^2}{2\sigma^2}} \tag{2.13}$$

In order to sufficiently capture disorder effects we averaged over one hundred different random NP lattices. Error bars in our calculations represent the standard deviation of the mean.

CHAPTER 3

TRIDENS: Transport in Defected Nanoparticle Solids

3.1. Introduction

Colloidal semiconductor nanoparticles (NPs) are singularly promising nanoscale building blocks for fabricating mesoscale materials that exhibit emergent collective properties. There is a growing interest to use NPs for numerous optoelectronic applications [**46**, **47**], including third generation solar cells [**2**, **3**] light emitting diodes [**7**], and field effect transistors (FET) [**8**, **9**].

Electron wavefunctions are localized on the individual NPs. This "quantum confinement" makes the electronic parameters tunable with the NP size, and thus makes the NP solids a very versatile platform for applications [**84**]. However, the very same quantum confinement also suppresses the transport between NPs, and thus drives NP solids insulating. As a result, without the application of specific transport-boosting fabrication steps, the electron mobility in NP solids is often in the range of $10^{-2}-10^{-1}$ cm^2/Vs [**16**,**85**]. These mobilities are typically measured in FET arrangements. This is orders of mangitude below the mobilities that would be acceptable for electronic applications. Therefore, increasing the mobility and transport in NP solids is one of the central challenges on the way to realize the promise of NP solids.

Various experimental groups managed to boost the mobility by enhancing the inter-NP transition rate with a variety of methods, including: ligand engineering [**10**, **11**, **12**], band-alignment engineering [**13**, **14**], chemical-doping [**15**, **16**], photo-doping [**17**], metal-NP substitution [**18**], epitaxial attachment of NPs [**19**, **20**], and atomic layer deposition methods [**21**]. Encouragingly, these efforts recently translated into notable progress, as NP solids were reported to exhibit band-like, temperature-insensitive mobilities, with values exceeding 10 cm^2/Vs at room temperatures [**16**,**85**]. It is important to note that some experiments reported data that can be interpreted as evidence for band-like transport. One of these is the relative temperature independence of the observed mobilities, in contrast to hopping insulators where an activated temperature dependence is expected.

However, the absolute values of the mobilities remain relatively low compared to most metals, and this makes conservative commentators stop short of identifying this transport as metallic [**16**, **85**].

On the theoretical front, there have been efforts from several groups to understand electronic transport in NP films and solids. Density functional theory (DFT)-based ab initio calculations of the energy levels of a single NP alone are already limited to only hundreds of atoms for higher-reliability methods, and a few thousands for more approximate methods by prohibitive CPU times. These translate to diameters less than 2-3 nm, whereas experimental NP diameters often exceed 5-6 nm. Next, the accurate computation of the NP-NP transition rates would require the simulation of two NPs. And even if this calculation is completed, it does not address that the NP-NP transport is not metallic but insulating; the disorder of the parameters from NP to NP; and finally the defects of the NP solids. In total, ab initio descriptions alone are very far from being capable of describing transport in NP solids. Cleary, there is a pressing need for developing mesoscopic transport simulations that somehow integrate ab initio calculations.

Shklovskii et al. have developed transport calculations for a NP array in a FET geometry, where they focused on the effects of the Coulomb interaction [**50**]. The interplay of transport and Coulomb interactions was studied in Refs. **86** and **69**, albeit on very small samples. Over the last few years, our group developed the Hierarchical Nanoparticle Transport Simulator (HINTS) platform that starts with an ab initio calculation of the energetics of individual nanoparticles, then forms a NP solid of several hundred NPs, and finally simulates transport across this NP solid by a Kinetic Monte Carlo method [**59**, **60**]. HINTS can simulate 500-2,000 nanoparticles. A reassuring validation of HINTS emerged from simulating the dependence of the mobility of PbSe NP layers as a function of the NP diameter. The results in [**59**, **60**] closely tracked the experimental results of Liu et al., who studied the electron mobility of PbSe layers in a FET geometry [**76**]. More recently, we studied commensuration effects in bilayer NP solids [**87**].

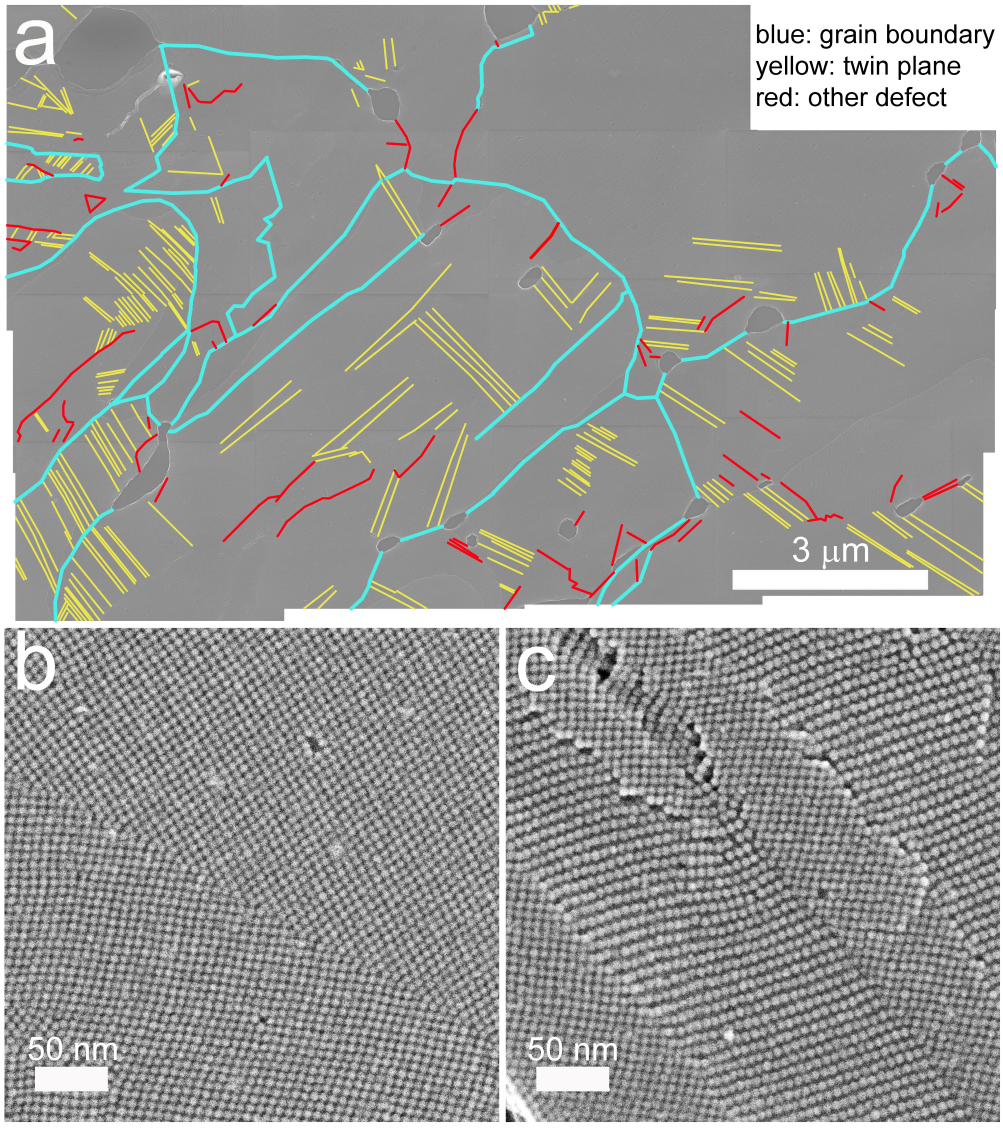

FIGURE 3.1. Common planar defects in PbSe nanoparticle superlattices. (a) Grain map of a typical region of an PbSe NP superlattice film showing the location of several types of planar defects. Blue, yellow, and red lines denote wide-angle grain boundaries, twin planes, and more complex, unclassified planar defects and defect clusters, respectively. The image is a montage of fifteen low-magnification, high-resolution SEM images. Voids, step edges, vacancies, and other types of non-planar defects are also visible in the montage. (b) Higher-magnification secondary electron image of a bicrystalline region of an epi-SL film with two (100)SL-oriented SL grains meeting at a twin plane. (c) Image of another region of the same epi-SL film showing multiple grain boundaries between (100)SL- and $(0\bar{1}1)$SL-oriented grains, as well as several other planar defects.

However, these theoretical efforts only considered NP solids with homogeneous disorder: the NPs were arranged either in a close-packed glassy/jammed structure, or on an ordered superlattice (SL) with disorder only in the NP size. In contrast, representative scanning electron microscope (SEM) images, like in Fig. 3.1, taken of NP solids with millions of NPs, conspicuously reveal that typical NP solids are also characterized by disorder on much larger length scales. These defects, often on the μm length scale, have sizes well beyond the capabilities of any published technique, including HINTS. Therefore, there is a need for transport simulation methods that are capable of capturing meso- and macro-scale defects and their effect on transport.

We performed one step in this direction previously by extending our HINTS method to include percolative effects into homogeneously disordered NP solids [**60**]. This simulation captured physics on the longer length scales of percolative clusters. Our main message was that a metal-insulator transition (MIT) occurs when a percolating path of metallic-connected NPs develops across the entire sample. We described this MIT as a Quantum Percolation Transition. However, this work still did not incorporate planar defects.

3.2. Simulation Methods

To answer the above needs, in this chapter we report our work that boosted the capability of our HINTS platform by introducing additional hierarchical layers to capture the effect of planar defects on the transport in NP solids. First, we used HINTS to individually model a NP superlattice (SL) with one planar defect that was either a generic grain boundary or a twin plane. Second, we simulated transport across a large number of such single-defect SLs, and determined the distribution of the mobilities of the single-grain-boundary NP SLs and that of the single twin-plane NP SLs. We also determined the distribution of the mobilities of undefected NP SLs with only homogeneous NP disorder. Third, to reach a simulation scale approaching the scale of the NP solids in the experiments, we built a resistor network where the individual resistor values were taken from the three mobility distributions with predetermined probabilities. Motivated by our previous work [**60**], we determined the resistance of the entire resistor network by changing the fraction of undefected NP SLs within the network. Finally, we analyzed our results by a finite size scaling method.

We call this boosted HINTS platform the TRIDENS: the "**TR**ansport **I**n **DE**fected **N**anoparticle **S**olids" Simulator. With TRIDENS, we are capable of capturing the physics from atomistic length scales up to the scale of NP solids in the experiments by integrating the simulations on several hierarchical layers. The complete hierarchical structure of TRIDENS is presented below.

(1) The energy levels of individual PbSe NPs are determined by adapting a $k \cdot p$ calculation within the NP diameter range of 5-7 nm. The valence band and conduction band values have been validated via comparison to optical experiments [**62**]. Here we focus on PbSe NPs because they are of considerable interest for solar applications due to their large Bohr exciton radius and small direct bulk bandgap [**88**], and exhibit the possibly game-changing multiple-exciton generation (MEG) [**89**]. For these reasons, PbSe NPs are often thought to have strong promise for solar applications.

(2) The electron-electron interaction is included on the level of an on-site, or self-charging energy expression, E_C, defined as:

$$E_C = n(\Sigma^0 + \frac{(n-1)}{2}\Sigma) \tag{3.1}$$

where n is the number of electrons on the NP. Σ^0 is the self-charging energy of loading the first electron onto a neutral NP. Σ is the extra energy it takes to load each additional electron onto the NP due to repulsive Coulomb interaction with the (n-1) electrons already on the NP, as well as the interaction with the induced image charge.

This self-charging energy can be calculated by a variety of methods, including the semi-empirical pseudopotential configuration interaction method of Zunger and coworkers [**64**] and the single NP empirical-perturbative hybrid calculations of Delerue [**90**]. In this chapter we report results with the latter approach. In this approach

$$\Sigma^0 = \frac{q^2}{8\pi\epsilon_0 R}(\frac{1}{\epsilon_{\text{solid}}} - \frac{1}{\epsilon_{\text{NP}}}) + 0.47\frac{q^2}{4\pi\epsilon_0\epsilon_{\text{NP}}R}(\frac{\epsilon_{\text{NP}} - \epsilon_{\text{solid}}}{\epsilon_{\text{NP}} + \epsilon_{\text{solid}}}), \tag{3.2}$$

and

$$\Sigma = \frac{q^2}{4\pi\epsilon_0 R}(\frac{1}{\epsilon_{\text{solid}}} + 0.79\frac{1}{\epsilon_{\text{NP}}}). \tag{3.3}$$

For the dielectric constant inside the NP, we assume that it equals the bulk high frequency dielectric constant of PbSe, taken to be 22.0. To model the dielectric constant of the medium surrounding the

NP, we account for both the organic ligand shell of the NP as well as the presence of neighboring NPs. We assume that the ligands themselves have a dielectric constant of 2.0. The dielectric constant of the entire solid is then calculated using the Maxwell-Garnett (MG) effective medium approximation:

$$\epsilon_{\text{solid}} = \epsilon_{\text{ligand}} \frac{\epsilon_{\text{NP}}(1+\kappa f) - \epsilon_{\text{ligand}}(\kappa f - \kappa)}{\epsilon_{\text{ligand}}(\kappa + f) + \epsilon_{\text{NP}}(1-f)} \tag{3.4}$$

where κ is 2 for spherical NPs, and f is the filling factor.

We note that the long range part of the Coulomb interaction can be easily included into the calculation. The long range interactions change the nature of transport from activated hopping to Efros-Shklovski type variable range hopping. However, many experiments show that while this Efros-Shklovskii hopping dominates at low temperatures, as the temperature is raised past 150-200K, the transport becomes dominated by nearest neighbor hopping. [**91**] Since our work focuses on temperature ranges around ambient room temperature, representing the Coulomb interactions with the on-site term only is appropriate.

(3) We modelled the electron transitions between neighboring NPs via a Miller-Abrahams phonon-assisted hopping mechanism:

$$\Gamma_{i\to j} = \begin{cases} \nu g_{ij} \beta_{ij} \exp \frac{-\Delta E_{ij}}{k_b T} & \text{if } \Delta E_{ij} > 0 \\ \nu g_{ij} \beta_{ij} & \text{if } \Delta E_{ij} <= 0 \end{cases} \tag{3.5}$$

where ν is an attempt frequency, chosen to be $10^{12}\,\text{s}^{-1}$, g_{ij} is the product of the initial density of states on NP_i and the final density of states on NP_j, and β_{ij} is the tunneling amplitude. β_{ij} is calculated using the WKB approximation as:

$$\beta_{ij} = \exp\left(-2\Delta x \sqrt{\frac{2m^*(E_{\text{vac}} - E_{ij})}{\hbar^2}}\right) \tag{3.6}$$

Here Δx is the NP-NP surface-surface separation distance. m^* is the effective mass of the electrons in the tunneling medium, approximated as $.05m_e$, the effective mass of electrons in bulk PbSe. It is noted that m^* was estimated to be $0.3m_e$ in NPs [**92**]. E_{vac} is the vacuum energy level, set to be zero as all other energy levels are defined relative to the vacuum. E_{ij} is the tunneling energy,

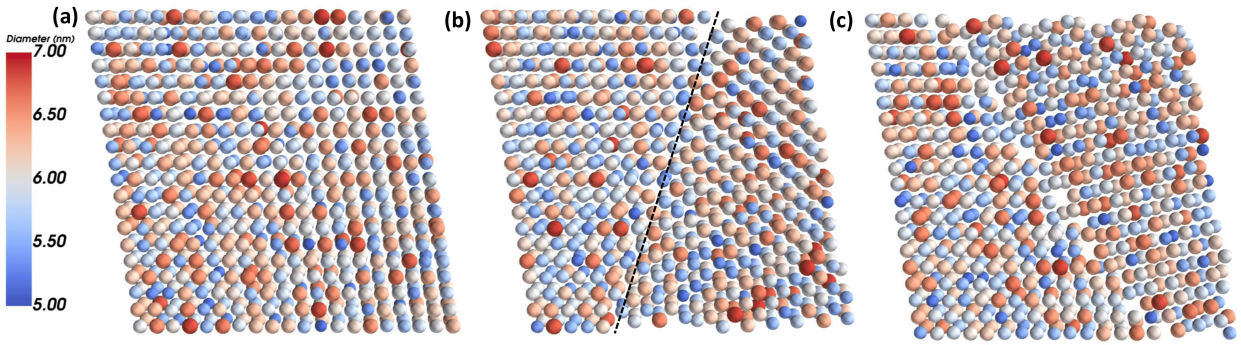

FIGURE 3.2. Top down views of the three types of the simulated NP SLs: (a) An undefected NP SL, characterized by the NPs having only size and location disorder; (b) A NP SL, containing a twin plane, as denoted by the dashed line, also with NP size and location disorder; and (c) An NP SL, containing a grain boundary, also with NP size and location disorder. NP color corresponds to NP diameter, as indicated in the colorbar on the left.

taken to be the average of the initial and final states of the hopping transition: $E_{ij} = (E_i + E_j)/2$, where E_i is the energy level of NP_i.

(4) To reach the length scale of hundreds of nanometers, we generated triclinic NP superlattices, of PbSe NPs with a 20x20x2 geometry, inspired by the 2D channel geometries of FETs used in transport experiments [**93**]. The triclinic unit cell was described with lattice constants $a_1 = a_2 = a_3 = 6.9$ nm and angles $\alpha = \beta = \gamma = 99°$. The average NP diameter was 6.0 nm. Size and location disorder were introduced by assigning the NPs a diameter and lattice displacement vector according to Gaussian distributions of widths $\sigma(diameter) = 0.4$ nm and $\sigma(location) = 0.3$ nm respectively. See Fig. 3.2a for an example of one of these SLs. In our undefected SLs, these parameters yield a $\langle \beta_{ij} \rangle \simeq 0.015 \pm .02$.

Layers (1)-(4) are the main constituents of our HINTS platform. HINTS is suitable for capturing the effects of homogeneous disorder, i.e. disorder associated with the size and location of the NPs that varies from site to site of the NP superlattice, but does not involve planar defects. Next, we describe the additional layers of the TRIDENS that enable us to access length scales well beyond the reach of HINTS.

(5) As a first step, we introduced a single planar defect into each generated NP superlattice (SL). We carefully analyzed SEM images of NP solids with millions of NPs of the type of Fig.3.1, and determined the predominant types of defects and their statistics, such as the lengths and densities

of the planar defects. Based on the SEM image analysis, the most relevant and oft-occurring planar defects were twin planes and grain boundaries.

(a) Twin planes: the NP superlattice is mirrored across a boundary plane, creating two crystallites, or grains, which have reflected in-plane unit cells. Twinned grains can also be related by a 180° rotation normal to the twin plane. The twin plane is always parallel to a possible crystal face (but not any planes of complete symmetry, e.g. it is distinct from all space group symmetries), and thus requires the two grains to share some NP lattice sites along the boundary plane. See Fig. 3.1b and Fig. 3.2b. The high symmetry nature of twin planes makes them a low disorder defect, compared to the more highly disordered grain boundaries discussed below. In our generated samples the twin planes were created in a (100) in-plane oriented SL, and the orientation of the twin plane itself was randomly selected on a sample-by-sample basis from all possible crystal planes which would span the entire NP simulation SL in the x-direction (in order to bisect the SL). As an example, one such boundary orientation is that of a $(01\bar{2})/(02\bar{1})$ twin boundary, where $(01\bar{2})$ is the orientiation of the boundary plane in grain 1, and $(02\bar{1})$ is the orientiation of the boundary plane in the mirrored grain 2.

(b) Grain boundaries: the NP superlattice is again fractured by a boundary plane. However, unlike with twin planes, the superlattice is not mirrored across the boundary plane. There are two main types of grain boundaries. 1) Tilt grain boundaries, where the in-plane SL orientation is the same in the two grains, but they are spatially rotated in-plane relative to each other. The angle of rotation can be divided into "low angle" and "high angle" regimes, where the higher the angle of rotation, the more disordered the grain boundary (with large areas of poor fit). 2) Twist grain boundaries, where the in-plane superlattice orientations of the two grains are different (rotation occurs along an axis perpendicular to the boundary plane). Such grain boundaries will result in two crystallites/grains with different in-plane superlattice orientations (e.g. a boundary between a $(100)_{\mathrm{SL}}$ in-plane orientation and a $(101)_{\mathrm{SL}}$ in-plane orientation).

In our generated samples, we simulated grain boundaries with a combination of tilt and twist mismatching. Specifically, the boundary plane separated grains of $(100)_{\mathrm{SL}}$ in-plane orientation and $(01\bar{1})_{\mathrm{SL}}$ in-plane orientation respectively, with the relative in-plane spatial orientation of the two grains depending on the angle of the boundary plane (chosen at random on a sample-by-sample

basis). The boundary plane was always limited to angles which would span the entire NP simulation SL in the x-direction (in order to bisect the SL). This results in grain boundaries which are much more extensively disordered than twin planes, particularly when the boundary plane results in a high-tilt grain boundary. See Fig. 3.1c and Fig. 3.2c. Hereafter, we will refer to our specific combination of boundary mismatching as simply a "grain boundary".

In total, we generated 30,000 NP superlattices, containing either one or two grains, where we varied the disorder of the NP diameters (see color code in Fig. 2), the on-site NP location disorder, and the orientation of the planar defects as viewed out-of-plane. Of these 30,000 NP SLs, 10,000 NP SLs had no planar defects, the next 10,000 NP SLs contained one twin plane, and the last 10,000 NP SLs contained a grain boundary.

Fig.3.1 shows other types of defects as well. We determined that point vacancies have minimal effect on the mobilities in the insulating phase. One can also see tears/rips/voids/cracks in the SEM image. NP superlattice fabrication technologies will be ready for technical application when they can minimize or eliminate such disruptive tears. For these reasons, we did not model either of these defects.

(6) Next, we determined the electron mobility across each of the 3x10,000 defected NP SLs. To do this, each NP SL was populated with electrons, randomly placing them on NPs, using the Mersenne Twister, until a predetermined electron density was reached. The chance of an electron being placed on any particular NP was uniform, independent of electron occupation and NP parameters. Data was only taken well after the system achieved equilibrium. A small voltage was applied across the sample to induce transport in the linear I-V regime, with periodic boundary conditions. Finally, the electron transport was simulated by evolving time via a kinetic Monte Carlo (KMC) algorithm. The so-determined mobilities of the 3x10,000 NP SLs were used to create the mobility distributions for the homogeneously disordered NP SLs, the twin-plane-supporting NP SLs, and the grain-boundary-supporting NP SLs. The first class of NP SLs will also be referred to as "undefected NP SLs", the latter two classes as "defected NP SLs".

(7) To simulate NP solids on mesoscopic length scales of the order of 10 μm or longer, we generated a classical resistor network, with resistors chosen at random from the distributions determined in step 6. Which distribution the resistors were chosen from was also randomly determined,

according to a parameter that describes the fraction of defected resistors. Random numbers were generated using standard numpy libraries. Each resistor represents an NP SL with an $L = 20$ length planar defect. One notes that in Fig.3.1 many of the planar defects are considerably longer than $L = 20$. Representing planar defects with longer lengths is possible in TRIDENS by placing defected NP SLs correlated along the lines of the network. Such longer range defect-correlations were not pursued in the present work, but will be included in future work.

With these preparations, the mobility of the overall NP solid was determined by treating this NP SL network as a resistor network. We used the Laplacian method of F. Y. Wu et al. to calculate the overall resistance across the entire network [**94**]. The electrodes were modeled as equipotential metallic strips spanning the entire length of the sample edge, thus making them equivalent to a single node on a resistor network. These electrodes were coupled to the sample by contact resistors that were chosen according to the same rules as the bulk resistors.

(8) Having determined the overall mobility of the network of defected NP SLs, we adapted finite size scaling methods to analyze whether this resistor network model built from defected NP SLs had a phase transition, or a crossover, and if so, what are the properties of this transition. To this end, we repeated step (7) for resistor networks of various sizes, including 32x32, 64x64, and 128x128. As detailed below, our finite size scaling found a percolation transition that separates a low mobility insulator from a high mobility insulator. We used finite size scaling to determine the critical properties of this transition, including the critical point, the critical exponents and the universal scaling function.

3.3. Experimental Methods

Materials: Lead oxide (PbO, 99.999%), oleic acid (OA, technical grade, 90%), diphenylphosphine (DPP, 98%), 1-octadecene (ODE, 90%), ethylene glycol (EG, 99.8%, anhydrous), acetonitrile 99.99%, anhydrous, hexanes ≥99%, anhydrous, toluene 99.8%, anhydrous, and 3-mercaptopropyl trimethoxysilane (3-MPTMS, 95%) were purchased from Sigma Aldrich and used as received. Trioctylphosphine (TOP, technical grade, >90%) and selenium (99.99%) were acquired from Fluka and mixed for 24 hours to form a 1 M TOP-Se stock solution. Ethylenediamine (EDA, >98.0%,

anhydrous) was purchased from TCI and mixed with acetonitrile in a 1:1 volume ratio to make a 7.5 M EDA stock solution, this is a slight modification to a published procedure [**93**].

Quantum Dot Synthesis: In this experimental section we adopt the alternative terminology of "quantum dots" to refer to the nanoparticles, to accommodate alternative terminologies preferred by different communities. PbSe QDs were synthesized and purified air-free using a slight modification of a published procedure [**93**]. Briefly, PbO (1.50 g), OA (5.00 g), and ODE (10.00 g) were mixed and degassed in a three-neck round-bottom flask at room temperature. The mixture was heated to 120 C under vacuum to form dissolved Pb(OA)2 and dry the solution. After 1 hour at 120 C, the Pb(OA)2 solution was heated to 180 C under argon flow and 9.5 mL of a 1 M solution of TOP-Se containing 200 μL of DPP was rapidly injected into this hot solution. An immediate darkening of the solution was observed, and the QDs were grown for 105 seconds at $\sim$160 C. The reaction was quenched with a liquid nitrogen bath and injection of 10 mL of anhydrous hexanes. QD purification and SL fabrication were performed in glove boxes with $<$0.5 ppm O2 content. The QDs were purified by two rounds of precipitation/redispersion using acetonitrile/toluene and stored as a powder in the glove box.

Substrate preparation: Following and slightly modifying the procedure seen in [**93**] a single-side polished Si substrate was cleaned using 10 minutes of sonication in acetone, Millipore water, and then isopropanol, followed by drying in a stream of flowing air. The cleaned substrate was immersed in a 100 mM solution of 3-MTPMS in toluene for 1 hour to functionalize its native SiOx surface for improved QD film adhesion, then rinsed with neat toluene and dried in flowing air.

Superlattice fabrication, electron microscopy imaging: Quantum dot superlattice films were fabricated and imaged using (modified) published procedures [**93**]. An oleate-capped superlattice was prepared in a glovebox ($<$2 ppm O2) by drop casting 60 μL of 20 g/L dispersion of PbSe QDs in hexanes onto 7 mL of ethylene glycol (EG) in a Teflon well (3.5 x 5 x 1 cm). After depositing the QD solution, the well was immediately covered with a glass lid. The hexane evaporated over 30 minutes, resulting in a smooth, dry QD film floating on the EG surface. The glass lid was then removed and 0.1 mL of a 7.5 M solution of EDA in acetonitrile was slowly injected (5-10 sec) into the EG under the QD film using a 1 mL syringe. After 30 seconds of exposure to EDA, the resulting

epi-SL film was stamp transferred to the Si substrate using a vacuum wand, rinsed vigorously with acetonitrile, and dried under flowing N2.

Scanning electron microscopy (SEM) imaging was performed on an FEI Magellan 400 XHR SEM operating at 10 kV. Grain maps were produced by stitching together fifteen 6,144 x 4,415 pixel images acquired at 50,000x magnification, providing the ability to resolve individual QDs in the sample. Image stitching was performed in Adobe Photoshop. Grain boundaries, twin planes, and other planar defects were then located by eye and drawn in manually.

Superlattice samples for TEM analysis were prepared by stamping QD films from the EG surface onto holey carbon TEM grids without a carbon film coating. The use of TEM grids free of a carbon film was critical for high-quality secondary electron imaging (SEI) in the TEM. SE imaging was performed on a JEOL JEM-2800 TEM operating at 200 kV using a probe size of 1.0 nm.

3.4. Results and Discussion

TRIDENS simulations: We laid the foundation of our simulation by carrying out steps (1)-(4), as done in a standard HINTS study. To carry out step (5), we generated 3x10,000 defected NP SLs by starting with homogeneously disordered but undefected 20x20x2 NP SLs whose shape broadly corresponded to FET geometries, and then inserted a twin plane planar defect into 10,000 NP SLs, and a grain boundary planar defect into another 10,000 NP SLs. The latter sometimes involved removing a few NPs to keep the shape of the NP SLs largely unchanged.

Next, we executed step (6) by determining the mobility distribution of the defected NP SLs. The mobility distribution for the homogeneously-disordered, undefected NP SLs is shown in Fig.3.3a. The mobility distribution of the twin-plane NP SLs is shown in Fig.3.3b. Finally, the mobility distribution of the grain-boundary NP SLs is shown in Fig.3.3c. All three distributions were approximately normal, and could be well characterized by a mean and a standard deviation. The mobility of the undefected NP SLs was 0.42 ± 0.1 cm^2/Vs, the mobility of the NP SLs containing twin planes was 0.16 ± 0.06 cm^2/Vs, and the mobility of the NP SLs containing grain boundaries was 0.09 ± 0.05 cm^2/Vs, as shown.

We then performed step (7) by assembling a resistive network whose individual links had mobilities selected from the above determined mobility distributions. To identify the paradigmatic

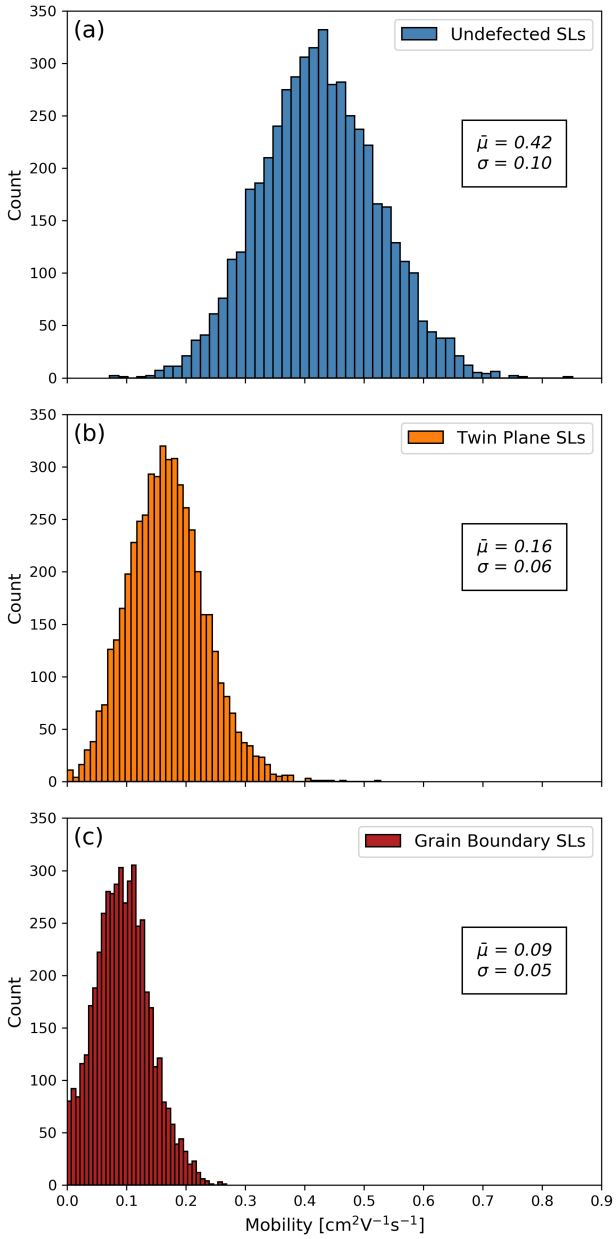

FIGURE 3.3. Mobility distributions of the 3 types of NP SLs: (a) Undefected NP SLs, the NPs having size and location disorder; (b) NP SLs, each containing a twin plane, also with NP size and location disorder; (c) NP SLs, each containing a grain boundary, also with NP size and location disorder. Displayed in each panel is the average mobility and standard deviation of Gaussians fitted to the distributions. All simulations were performed at a temperature of $T = 300K$.

aspects of the behavior of the mobility of the NP solid, we selected the links from the highest mobility undefected NP SL distribution with a probability p, and from the lowest mobility grain

boundary NP SL distribution with a probability $(1-p)$. We used this p, the fraction of the high mobility undefected NP SLs/links as the control parameter of our study. Initially we expected that when the probability $(1-p)$ of the low mobility defected NP SLs becomes small, then the electrons will be able to "flow around" the low mobility links through the high mobility links. Put differently, the high mobility links will be able to approximately short out the low mobility links. Had this expectation been true, then the mobility of the NP solid should have exhibited a saturation as p approached 1.

Fig.3.4 shows the evolution of the mobility of NP solids with p. Visibly, our initial expectation was not confirmed as the mobility did not show a saturation as the fraction p of the undefected NP SLs approached 1.0. The high mobility links did not "short out" the low mobility links. A possible explanation is that the mobilities of the different NP SLs were not different enough for such a short-out. We checked the robustness of this result, and found the same characteristic non-saturating shape in other 2D geometries, as well as in 3D bulk networks.

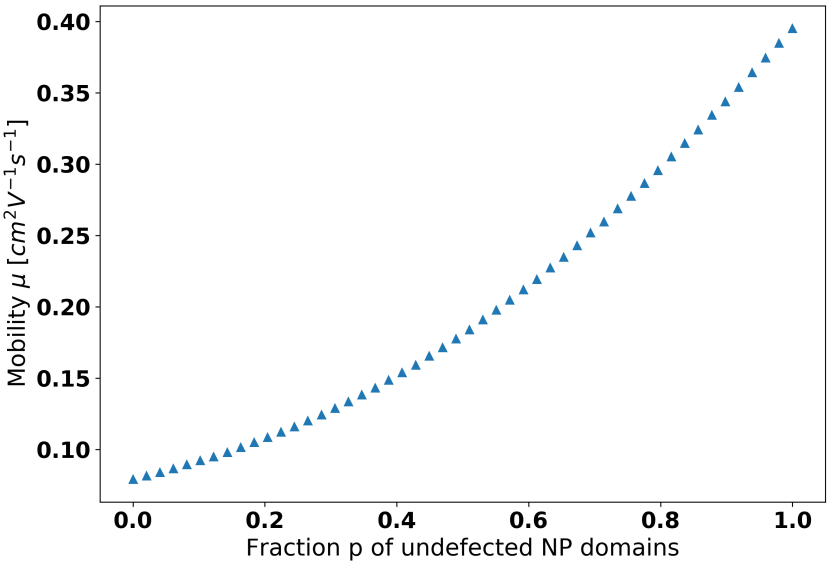

FIGURE 3.4. Mobility of a 32x32 resistor network whose resistors/links are chosen from two distributions, the low mobility grain boundary NP SLs mobility distribution and the high mobility undefected NP SLs mobility distribution. The fraction p of the high mobility NP SLs sweeps the 0 to 1 region. The error bars are smaller than the data points.

Bimodal percolation transition: Next, we investigated whether there is a percolative critical behavior as the p fraction of high mobility links is varied. The simple case of a resistor network, where the links either have a finite (electronic) mobility μ with probability p, or a non-conductive zero mobility with probability $(1-p)$, has been extensively analyzed. The conductivity of such a resistor network exhibits a critical behavior across the percolation critical point p_c with a power law dependence $\mu \propto (p-p_c)^t$, where the critical exponent $t > 1$ is universal, and p_c is the percolation threshold.

Remarkably, the closely related bimodal problem of the links of a network having a high conductivity $\sigma(high)$ with probability p, or a low but finite conductivity $\sigma(low)$ with probability $(1-p)$ has been rarely analyzed. Efros and Shklovskii (ES) established the broad framework for the analysis, when they made the analogy between this bimodal distribution problem and the problem of how the critical behavior of a spin system gets modified by the presence of a symmetry breaking magnetic field [**95**]. They hypothesized a power law critical behavior for the network conductivity, where the universal scaling function at the critical point $p = p_c$ is anchored by the ratio of the high and low conductivities. However, they did not determine either the critical exponents, or the universal scaling function.

Finite size scaling: Next, we attempt to adapt the ES bimodal framework to describe our TRIDENS-simulated results. The finite size L of the simulated samples makes it necessary to analyze the results by finite size scaling. Normally this is handled by the introduction of a scaling function with a single variable: the ratio of the sample size L to the correlation length $\xi = \xi_0 P^{-\nu}$, where $P = \frac{|p-pc|}{pc}$ that smoothes over the non-analytic critical behavior.

However, for the present, bimodal mobility distribution problem ES argued that the ratio of conductivities plays the role similar to an external magnetic field in a critical magnetic system: $\frac{\sigma_{low}}{\sigma_{high}} = h$, and already smoothes over the critical behavior. Therefore, the model needs to be analyzed by a two variable finite size scaling form, where the ratio L/ξ is a second factor that smoothes the critical behavior:

$$\mu(P, L, h) = P^{-\alpha}\mu(hP^{-\Delta}, LP^{\nu}) \tag{3.7}$$

where $\mu(x, y)$ is the universal finite size scaling function, and α, ν and Δ are critical exponents. The analysis is more tractable if the singular P dependence is absorbed by factoring out $hP^{-\frac{\alpha}{\Delta}}$ from μ, leaving us with:

$$\mu(P, L, h) = h^{-\alpha/\Delta}\mu'(hP^{-\Delta}, LP^{\nu}) \tag{3.8}$$

Since $\mu'(x, y)$ is a two-variable function, the full testing of the finite size scaling hypothesis would require a quite extensive computational effort. Therefore, we narrowed our analysis of the finite size scaling assumption to the first variable, $hP^{-\Delta}$, while keeping the second variable, LP^{ν}, constant. As the lattice sizes were varied from $L = 32$ to $L = 128$, keeping LP^{ν} constant required the appropriate modification of P. We then chose the h values so that the critical regime on either side of the critical point p_c was well sampled.

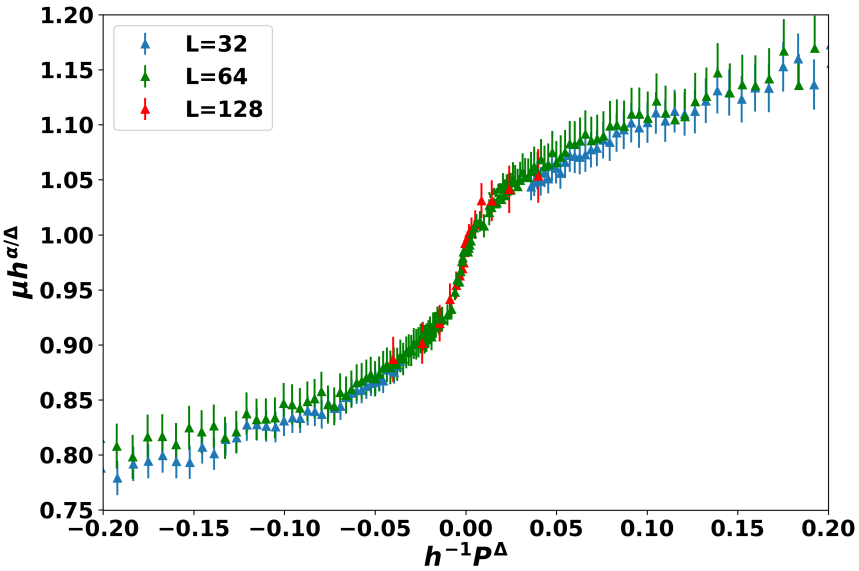

FIGURE 3.5. Scaled data of $\mu h^{\alpha/\Delta}$ vs. $h^{-1}P^{\Delta}$ for 3 different lattice sizes. The product LP^{ν} is held constant.

Fig. 3.5 shows the scaled mobility $h^{\alpha/\Delta}$ as a function of $h^{-1}P^{\Delta}$ for a fixed value of LP^{ν}, for three lattice sizes, varying from $L = 32$ to $L = 128$. Reassuringly, we were able to achieve very good data collapse within the $(-0.1, 0.1)$ critical regime around the critical point at $P = 0$, which

remained acceptable out to $(-0.2, 0.2)$. Using the literature values of $\nu = \frac{4}{3}$ and $p_c = 0.5$, the best collapse was reached with exponents $\alpha = -0.99 \pm .02$ and $\Delta = 2.02 \pm .02$.

The success of the finite size scaling shows that the Efros Shklovskii analogy to critical spin systems in an external magnetic field is indeed appropriate for this bimodal percolation problem: as the fraction p of the high mobility undefected NP SLs increases, one can think of the evolution of the overall mobility as a modified percolation transition, rounded by the finiteness of the mobility of the low mobility NP SLs. As far as the authors know, this is the first report of the critical exponents and the universal scaling function of the bimodal distribution resistor network problem.

The following points are worth making. Fig. 3.5 shows that the overall network electron mobility, or conductivity, displays a marked transition from a low mobility insulator behavior when the high mobility NP SLs do not percolate yet, to a high mobility insulator behavior once the high mobility NP SLs percolated. Of course, both of these regimes are insulators, so while the geometry of the NP solid undergoes a genuine percolation transition, the conductive properties exhibit only a low mobility insulator-to-high mobility insulator transport crossover, not a genuine phase transition.

We have studied a version of this problem recently on the level of our HINTS code [**60**], where the NPs were connected with either low mobility activated insulating links, or high mobility, non-activated metallic links. In that version of the problem, the underlying percolation transition of the metallic links of the NP solid drove a genuine metal-insulator-transition (MIT), as the percolation of the metallic links created a genuine metallic phase. We conceptualized that MIT as a Quantum Percolation Transition, and adapted the ES bimodal mobility distribution percolation model for its description, as at any fixed temperature that version of the problem also consisted of a bimodal mobility distribution with low mobility links and high mobility links. Whether the high mobility phase is a metal or a high mobility insulator can be identified from the temperature dependence of its conductivity. In the absence of the present detailed finite-size scaling study, in Ref. [**60**] we developed a simple, mean-field model form for the scaling function that described the mobility's evolution from the low mobility insulator to the high mobility metal. With the notation of the present chapter, the mean field exponents were $\alpha = -1$ and $\Delta = 1$. This enabled us to create the dynamical phase diagram of the model on the electron filling – disorder plane, where

the MIT separated the insulating phase with activated conductivity from the metallic phase with non-activated conductivity.

The present bimodal TRIDENS study scales up our previous bimodal HINTS work to much larger length scales. The key distinction is that the building blocks of the HINTS network were the individual NPs, whereas in TRIDENS the building blocks are the NP SLs with around a thousand NPs (in the present work, with 800 NPs). Further, in HINTS the origin of the bimodal mobility distribution was the presence or absence of metallic links between individual NPs, whereas here the origin of the bimodal mobility distribution is the presence or absence of an planar defect across the individual NP SLs. Obviously, the HINTS transport modeling that tracks individual electrons transitiong between individual NPs is more detailed than the resistor network of the present TRIDENS work. Nevertheless, since the building blocks of both the bimodal HINTS and the bimodal TRIDENS are low mobility links and high mobility links, we expected that the same ES bimodal percolation model with the same universal scaling function and exponents will capture the critical behavior of the bimodal TRIDENS results. The success of the data collapse with the ES finite size scaling form validated this expectation. While, of course several different analytic forms can be fitted to the universal scaling function that emerged in Fig. 3.5, nevertheless it was reassuring that in particular the mean-field function of the bimodal HINTS study:

$$\mu'(hP^{-\Delta}, LP^{\nu} \to \infty) = 1/(1 + P/h) \tag{3.9}$$

was also consistent with it. Further, the $\alpha = -0.99$ exponent of the TRIDENS scaling is approximately equal to the $\alpha = -1$ mean field value within the margin of error. We noted that there was a difference regarding the Δ exponent: TRIDENS gave a $\Delta = 2.02$, whereas in the mean field theory $\Delta = 1$. However, such differences occur typically between mean-field and numerically determined exponents. All in all, the substantial correspondence between our HINTS and TRIDENS works demonstrated that the ES bimodal percolation model is a good, quantitative description of how the underlying percolation transition of the NP solid drives a low-mobility insulator-to-high-mobility insulator transport crossover.

For completeness we mention that we implemented TRIDENS with randomly selecting high or low mobility NP SLs for the links. This corresponds to planar defects with a length of tens of NPs. However, the sample in Fig.3.1 has many defects that are much longer. Such long defects can be modelled by selecting defected SLs along lines of links in TRIDENS, in a correlated manner. Such correlated TRIDENS models will be pursued in a future work.

3.5. Conclusions

Transport in nanoparticle solids must be simulated on extremely large length scales, corresponding to millions of NPs, because NP solids exhibit spatial structures on several length scales, from the subtleties of individual NPs through the sensitive modeling of inter-NP transitions and through transport across homogeneously disordered SLs all the way to transport in NP SLs with large planar defects. Single-level computational methods are manifestly unable to span these length scales. This is why in our previous work we developed the multi-level HINTS method that was capable of simulating transport across NP solids with up to a thousand NPs. However, even HINTS is unable to capture the effect of planar defects on transport in NP solids of the size of tens of microns.

In this chapter, we reported the development of the TRIDENS method that adds three further hierarchial layers on top of the HINTS method. In TRIDENS, we first introduced planar defects into individual NP SLs that comprised the order of about a thousand NPs. Then we used HINTS to simulate the transport across these defected NP SLs. We performed these HINTS transport simulations for tens of thousands of defected NP SLs, and constructed the distribution of the NP SL mobilities with planar defects. Second, the defected NP SLs were assembled into a resistor network with more than 10^4 NP SLs, thus representing about 10^7 individual NPs. This translated to length scales of tens of microns, approaching the experimental scales for NP solids. Third, and finally, the TRIDENS results were analyzed by finite size scaling to explore whether the percolation transition, separating the phase where the low-mobility-defected NP SLs percolate from the phase where the high-mobility-undefected NP SLs percolate, drives a low-mobility-insulator-to-high-mobility-insulator transport crossover that can be extrapolated to genuinely macroscopic length scales.

Our extensive TRIDENS analysis generated the following results. On the level of individual NP SLs, we found that the average of the mobility for undefected NP SLs was 0.42 ± 0.1 cm^2/Vs, for twin-plane-defected NP SLs 0.16 ± 0.06 cm^2/Vs, and for grain-boundary-defected NP SLs 0.09 ± 0.05 cm^2/Vs. On average, grain boundary defects hinder transport about twice as much as twin planes. This result makes sense, as grain boundaries are more disruptive to lattice periodicity than twin planes, and transport across the grain boundaries involves longer hops between more distant NPs, whereas transport across twin planes proceeds across many NPs shared by the grains on the two sides of the twin plane, and thus it involves regular hop lengths. It is noteworthy that the introduction of planar defects into NP SLs reduced their mobility by a factor of up to 5. On one hand, this is a substantial suppression of the mobilities that drives a transport crossover, and thus demonstrates the imperative of minimizing the density of planar defects in NP solids to help their suitability for applications. On the other hand, this is not a qualitative, order-of-magnitude suppression of the transport that indicate a Metal-Insulator-Transition: those are driven by the loss of phase coherence.

On the highest, resistor network-level analysis of TRIDENS, we observed that the introduction of the planar defects immediately started to reduce the network mobility. This finding suggests that even small concentrations of planar defects are not shorted out in NP solids, and thus every reduction of the density of planar defects will lead to further improvements of the transport in NP solids. Among the planar defects, the elimination of grain boundaries pays more dividends than that of twin planes.

For the theoretical description, we adapted the Efros-Shklovskii bimodal mobility distribution percolation model. We performed a finite size scaling analysis of the TRIDENS network mobilities. We demonstrated that increasing the density of the undefected NP SLs drives an underlying, structural/geometric percolation transition in the NP solid, which in turn drives a low-mobility-insulator-to-high-mobility-insulator transport crossover. We demonstrated that our adaptation of the ES bimodal theory's two-variable scaling function is an effective tool to quantitatively characterize this low-mobility-insulator-to-high-mobility-insulator transport crossover. For context, we discussed the analogies with the Quantum Percolation Transition we developed in our earlier, MIT-focused work [**60**].

CHAPTER 4

Disordered Mott-Hubbard Physics in Nanoparticle Solids:Transitions Driven by Disorder, Interactions, and Their Interplay

4.1. Introduction

Nanoparticle (NP) solids are aggregates of nanometer scale particles with interesting and potentially useful emerging electronic functionalities. In NP solids, the wavefunctions are typically "Quantum Confined" to the NPs, making their electronic properties tunable with the NP size. [**47**] This tunability makes them attractive for a wide variety of opto-electronic applications, [**46**] including photovoltaics, [**2**, **3**] light-emitting diodes, [**7**] and field-effect transistors (FETs). [**8**, **9**] However, the same Quantum Confined localization also drives the NP solids insulating, hindering charge transport and thus their utility. Therefore, driving NP solids from their insulating phase across a Metal-Insulator Transition (MIT) into a conducting, metallic phase is a top priority to boost their utility. Recent experimental attempts to cross the MIT included atomic layer deposition (ALD), [**21**] substitutional percolation, [**18**] chemical doping, [**15**, **16**] and photodoping. [**17**] ALD infilling with metal oxides already enhanced mobilities above 7 cm^2/Vs. [**21**] Whether these enhanced-mobility NP solids support coherent metallic transport is still debated. Building on these advances, NP solar cells were developed with impressive 13-16% power conversion efficiencies, [**96**, **97**, **98**].

There is a vast literature on the theory of the disorder-driven, "Anderson"-type MIT of non-interacting electrons. [**99**] The disorder of the site energies breaks up the site-to-site phase coherence of the originally extended wavefunctions, thereby localizing the electrons. Introducing interactions into Anderson localizaton makes the physical scenarios more complex, as revealed by scaling methods. [**100**, **101**, **102**] Implications for transport were studied, e.g., via the concept of the "Coulomb

blockade/gap", the energy cost of the attraction between the moving electron and the hole it leaves behind, thus suppressing transport at all fillings. [**103**] These ideas were adapted to NP solids e.g. in Ref. **15**. Transport has been described as nearest neighbor hopping at high T, [**104**, **105**] and as Efros-Shklovskii (ES) variable range hopping at low T. [**106**]

Interactions are especially important at commensurate fillings. An electron already on an NP blocks the transport of additional electrons through that same NP because of the Coulomb cost of double occupancy. This was referred to as a Mott-gap, or Coulomb blockade. This blockade fully blocks transport only at integer fillings. [**69**, **86**, **87**]

In recent years, the analysis of the interplay of disorder and interactions was re-energized by adaptating the Dynamical Mean Field Theory (DMFT) for analogous Hubbard models. [**107**, **108**, **109**] A surprising prediction of DMFT was that at n=1, at intermediate repulsion, increasing disorder first dissolved the Mott-localized phase into a metal, which then transformed into a Anderson-localized phase only at a higher disorder. Accordingly, the gap of the Mott-localized phase did not persist into the Anderson-localized phase with increasing disorder. [**108**,**109**] Fillings $n \neq 1$ were not yet investigated with DMFT.

Remarkably, despite all this progress, profound unmet needs remain. (1) In spite of inviting analogies, the vast amount of knowledge developed for the disordered Mott-Hubbard physics has not yet been adapted for NP solids, beyond some early suggestions. [**110**, **111**, **112**, **113**, **114**, **115**, **116**] For example, even though the mobility of some NP solids exhibits maxima and minima as the filling is tuned, these features were not attributed to Mott-Hubbard commensuration. [**55**] Adapting Hubbard-based knowledge to nanomaterials could inspire new pathways to improve the transport properties of NP solids. In reverse, articulating these connections could make nanoparticle solids a rich and well-controlled testing ground for Hubbard-based research.

(2) We are not aware of a theory of the MIT that starts from the insulating phase either in NP solids, or in the Mott-Hubbard field. Notably, both the scaling and the DMFT techniques are built with extended wave functions, and thus indicate Anderson/disorder localization only as the boundary where their applicability breaks down. Therefore, they are ill-suited to describe the Disorder-localized phase itself. Thus, developing a theory of the MIT out of the insulating

phase would complement the MIT theories from the metallic phase, thus creating a comprehensive characterization of the MIT.

In response to these needs, here are the main messages of this chapter. (1) We advocate that adapting disordered Mott-Hubbard ideas for NP solids, and viewing NP solids as well-controlled experimental platforms for Mott-Hubbard models, provides extensive benefits for both fields. (2) To start this adaptation, we developed a Hierarchical Nanoparticle Transport Simulator to reach the MIT from the localized phase; and we analyzed a multi-orbital Hubbard model with DMFT to reach the MIT from the delocalized phase. Using the combination of these complementary methods we determined the comprehensive phase diagram of Nanoparticle solids that consists of two distinct localized phases defining two distinct MITs, which can be crossed by tuning various control parameters. (3) Tuning the filling n towards integer values drives a Disorder-localized–to–Mott-localized transition. (4) For n=1 and large interactions, decreasing disorder drives a direct Disorder-localized–to–Mott-localized transition without an intervening metallic phase, characterized by a persistent gap. (5) For $n \neq 1$, decreasing disorder drives a Disorder-localized–to–Metal, Anderson-like MIT. (6) The DMFT-determined filling-dependence of the mobility at low disorder shows striking similarities to that at high disorder, demonstrating the internal consistence of our analysis.

4.2. Simulation Methods, Results, and Discussion

The HINTS method: Our **HI**erarchical **N**anoparticle **T**ransport **S**imulator HINTS is a Kinetic Monte Carlo transport simulator that is extended by an additional metallic transport channel. This extension makes HINTS capable of reaching the MIT from the insulating phase. In an introductory analysis at generic fillings, we reported reaching the MIT and interpreted it as a Quantum Percolation Transition. [**60**] However, we did not connect this MIT to Mott-Hubbard phenomena, did not consider its interplay with Anderson localization, and did not analyze the model at commensurate fillings.

HINTS simulates NP solids by a multi-level hierarchical approach. We start with computing the electronic energy levels by using a parameterized band structure of individual PbSe NPs with diameters in the 3-8 nm range. [**62**] On the next level, we account for the Coulomb interaction via

the on-site charging energy E_c:

$$E_C = n(\Sigma^0 + \frac{(n-1)}{2}\Sigma). \tag{4.1}$$

Here, n is the number of electrons on the NP after the electron is added. Σ^0 is the total electrostatic energy cost of loading an electron onto a neutral NP, while Σ is the energy cost of the Coulomb repulsion with the (n-1) electrons already on the NP. We calculate E_C with the hybrid empirical-perturbative method of Ref.**117**.

We proceed by generating a superlattice of PbSe NPs with diameters selected from a Gaussian distribution. We randomly fill this superlattice with electrons to reach the filling n electron/NP. As described below, the electrons will move from these random initial NPs to the energetically favorable NPs once their dynamics are simulated.

In our extended HINTS, the NP-NP transition rates are either Miller-Abrahams phonon-assisted hoppings, or non-activated metallic transitions, depending on whether the energy difference between the initial and final states was larger or smaller than a hybridization energy:

$$\Gamma_{i\to j} = \begin{cases} \nu g_{ij}\beta_{ij}\exp\left(\frac{-\Delta E_{ij}}{k_bT}\right) & \text{if } \Delta E_{ij} >= E_{\mathrm{H}} \\ \nu g_{ij}\beta_{ij} & \text{if } \Delta E_{ij} < E_{\mathrm{H}} \end{cases} \tag{4.2}$$

The attempt frequency ν is chosen to be $10^{12}\,\mathrm{s}^{-1}$ to match experimental data, g_{ij} is the product of the initial density of states on NP_i and the final density of states on NP_j, and β_{ij} is the WKB tunneling amplitude. The hybridization energy E_H is determined by the overlap of the electron wavefunctions of NPs i and j. The energy difference between the initial and final configurations ΔE_{ij} is:

$$\Delta E_{ij} = \Delta E_{ij}^{sp} + \Delta E_{ij}^{F} + \Delta E_{ij}^{C} \tag{4.3}$$

where ΔE_{ij}^{sp} is the difference in single-particle band energies; ΔE_{ij}^{C} is the difference in charging energies; and ΔE_{ij}^{F} is the difference of the potential energy from the external electric field.

Finally, we compute the mobility of the NP solid by an Extended Kinetic Monte Carlo (KMC) algorithm with a sufficiently small voltage bias. In particular, we measure the mobility only after the transients, driven by the initial conditions, have decayed and the flow of electrons reached a steady state. See SI for the full details of the HINTS method. We move to presenting the results of the HINTS simulations.

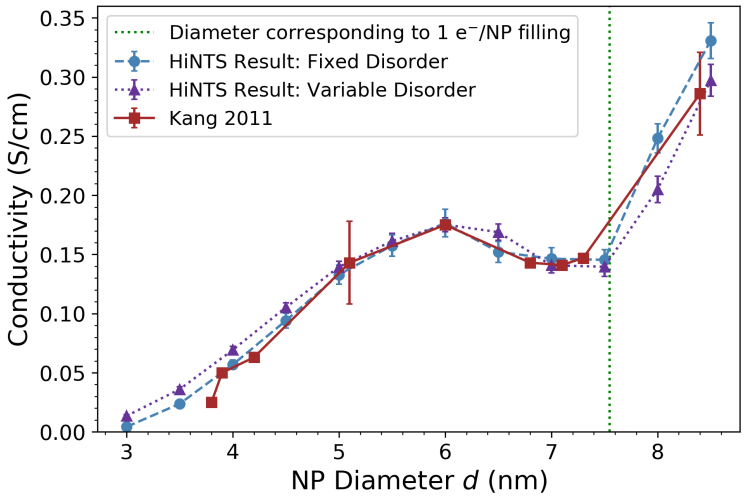

FIGURE 4.1. Conductivity v. NP diameter. HINTS simulations of PbSe NPs overlaid with exp. data. Volumetric electron density .0016 e/nm^3, ligand length 0.5 nm, $T = 200\text{K}$.

Disorder-localized–to–Mott-localized transition with a scan of the filling n: Experimentally, the electron/NP filling n can be scanned by increasing the average NP diameter at a fixed volumetric charge density. Two experimental groups measured the dependence of the mobility on the NP diameter in NP-FETs, and reported an initial rise followed by a maximum. [**55**, **76**]

We now use HINTS to compute the conductivity of PbSe NP solids as a function of NP diameter d. Fig. 1 shows the HINTS-computed conductivities with increasing d for two representations of the disorder: fixed diameter disorder of ± 0.3 nm, and variable diameter disorder of $\pm 5\%$. These results are overlaid on the experimental data of Kang *et al* [**55**]. The HINTS conductivities and the Kang *et al.* data exhibit remarkable agreement.

The broad rising trend of the mobility/conductivity is driven by two factors: (i) larger d means that the electrons can traverse a fixed length by fewer hops; and (ii) since the electron

energy-diameter relationship flattens with increasing d, the energy disorder induced by the diameter disorder decreases with increasing d.

The Kang experiments and our simulations both display a non-monotonic pattern overlaid on this broad rising trend. Conspicuously, the conductivity maximum at d=6 nm is observed to be only the beginning of a maximum-minimum-resumed rise pattern, centered on $n = 1$. The utility of adapting Mott-Hubbard ideas to analyze NP solids is compellingly demonstrated here by recognizing that such a conductivity minimum also arises when n is scanned across $n = 1$ in the repulsive Hubbard model, as the Coulomb repulsion opens a Mott gap at $n = 1$, and thus suppresses transport through the occupied NPs.

For context, we mention that earlier experiments [**76**] reported only a mobility maximum/ plateau, which we reproduced by simulation. [**59**]. However, neither works observed the maximum-minimum pattern, and correspondingly did not recognize that Mott-Hubbard commensuration physics drives all these phenomena.

Changing d also varies site energies and hopping rates, and thus convolutes the transition into the Mott-localized phase with other trends. Therefore, next we isolate the mobility's dependence on n in *fixed diameter* NP solids. Experimentally this can be achieved by varying the FET gate voltage applied to a NP solid.

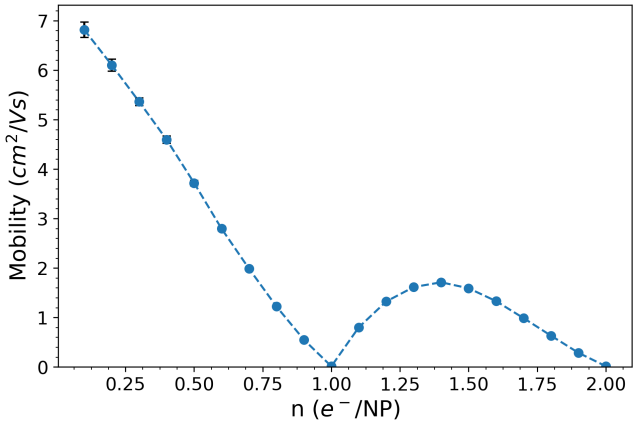

FIGURE 4.2. Electron mobility as a function of carrier filling in the disorder-localized Phase of PbSe NPs with diameters of 6.6 ± 0.3 nm. $T = 80$K. Average charging energy $E_c = 100$meV, average hopping energy $t = 7$meV.

Fig. 2 shows the HINTS-simulated mobility of a PbSe NP solid as n is varied. Visibly, the mobility exhibits minima at integer fillings, accompanied by maxima close to half-integer fillings, just as with increasing d. These features are much more pronounced than in Fig. 1.

The temperature dependence of the mobility/conductivity is activated for all fillings in Figs. 1 and 2, having a smaller, disorder-induced gap away from $n = 1$, that is boosted by the Coulomb blockade to a larger gap at $n = 1$. Thus, scanning with n through $n = 1$ crosses from a Disorder-localized phase into a Mott-localized phase, and then back to a Disorder-localized phase for $n > 1$, as expected from adapting the Hubbard model for these NP solids. And in reverse, the fact that the experimental data and our simulations show such a remarkable correspondences is compelling evidence that NP solids are well-controlled and tunable experimental realizations of the disordered Hubbard model.

Experimentally, such filling-driven Disorder-localized–to–Mott-localized phase transitions have been reported in Si quantum dot arrays, where the gate voltage was used to tune the filling, [**112**] and in InAs quantum dot solids [**118**].

Mott-localized–to–Disorder-localized transition with a scan of disorder W at n=1:

Next, we explore the robustness of the Mott-localized phase as the disorder $W/2t$ is varied at fillings around $n = 1$. Here the Hubbard t kinetic energy was determined by mapping our tunneling probabilities to Fermi's golden rule. W was determined from the sum of the disorder of the band and charging energies. We conduct this study on PbSe NP solids with a mean diameter of 6.5 nm by scanning the diameter dispersity up to 10%.

Fig. 3 shows the dependence of the activation energy/ gap Δ on the disorder $W/2t$ at n=1 (scan 3a), and at $n = 1+\delta$ where $\delta = 0.001$ (scan 3b). At n=1 and small disorder the gap Δ is Mott-like, as its value is set by the charging energy E_c: $\Delta/E_c \approx 1$. This Mott gap suppresses transport, and creates a Mott-localized phase. With increasing disorder, the gap Δ gets renormalized to a lower value $\Delta(W)$. The physics of this lower gap region is clarified by scan 3b of $\Delta(W)$ at the filling $n = 1 + \delta$. The gap $\Delta(W)$ is the same for $n = 1$ and $n = 1 + \delta$ above a critical value $W_c(Mott)/2t \approx 3.5$. This insensitivity of the gap to the charging energy and to commensuration identifies this phase as a Disorder-localized phase, into which the Mott-localized phase of n=1 transitions as W exceeds $W_c(Mott)$. Clearly, the transition at $n = 1$ across $W_c(Mott)$ is direct,

in the sense of having a persistent gap across the transition and no intervening gapless metallic phase. An analogous direct Mott-to-Anderson transition was reported by DMFT studies with a disorder scan in the Hubbard model at n=1 at around $W_c(Mott) = 3$, in good agrement with our result. Both studies worked in the $U/t = 10 - 14$ range. [**108**] It is noteworthy that the gap is relatively insensitive to W in the Disorder-localized phase. This is explained by the charging energy E_c screening the disorder W.

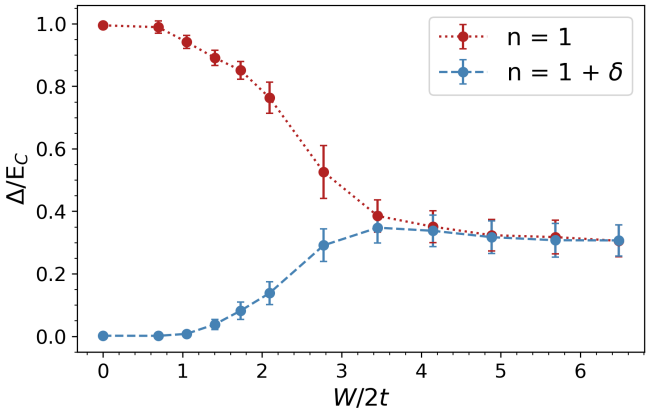

FIGURE 4.3. The disorder dependent gap Δ (W) for PbSe NPs: (a) $n = 1$; (b) $n = 1 + \delta$. $W_c(Mott)/2t \approx 3.5$; $W_c(MIT)/2t \approx 1.5$.

Beyond the remarkable disorder driven Mott-localized–to–Disorder-localized transition at n=1, scan 3b also reveals that as the disorder W is reduced at $n = 1 + \delta$, the gap shrinks to zero at $W_c(MIT)/2t \approx 1.5$. The vanishing of the gap indicates the disorder below which the wavefunctions become delocalized again. In this regime, the phases of the wafunctions become important, and the metallicity of transport is restored. HINTS does not track the phases of the electron wavefunctions, and thus can describe the transport with decreasing disorder only down to $W = W_c(MIT)$, but cannot enter the metallic phase itself. We identify $W_c(MIT)$ as indicating a Disorder-localized–to–Metal Transition, taking place at $n \neq 1$. This MIT at $W_c(MIT)$ at $n = 1 + \delta$ is disorder-driven, and is therefore distinct from the interaction-driven Mott transition at $W = W_c(Mott)$ at $n = 1$.

For context, we comment on the expectation that all electronic states are localized in 2D. This expectation, however, was demonstrated only in non-interacting systems. [**99**]. In interacting systems, the complex interplay of interactions and disorder has been shown to drive Metal-Insulator

delocalization transitions starting from the extended phase even in 2D. [**102**,**119**,**120**] Our results, building from the insulating phase, are consistent with and complement these claims.

These results have direct experimental relevance for NP solids beyond just PbSe NPs. Ref. **16** developed strategies to cross the MIT and induce band-like transport with the high mobility of 27 cm^2/Vs in CdSe NP FETs by increasing the kinetic energy t and decreasing the disorder W. Ref. **16** increased the wavefunction overlap, and thus t, by switching to the compact ligand thiocynate, and by annealing at the elevated temperatures of T=200C-250C. They eventually reached values of $t = 6 - 8$meV. They also reduced W by doping the CdSe NP FETs with Indium that filled up traps and thus reduced the trap-related disorder, eventually giving rise to an effective gap of $\Delta = 6 - 7meV$.

Our simulations provide a firm foundation for these strategies. To establish a quantitative correspondence, one would need to redo our PbSe simulation for CdSe NP solids to determine the additional disorder from polydispersity. Without the benefit of this calculation, we only make the qualitative observation that the $W/2t$ ratio where Ref. **16** reports an MIT is of the order 1, and thus consistent with our $W_c(MIT)/2t = 1.5$.

An additional strategy emerges from our simulations: the reduction of the charging energy E_c. We showed that E_c sets the Mott gap and screens the gap in the Disorder-localized phase, thus reducing E_c is yet another strategy to cross the MIT in NP solids.

Disordered-metal–to–Mott-localized transition as a function of n: We already established that the physics of NP solids is analogous to a disordered Hubbard model whose sites represent the individual NPs. We take into account the 8-fold degeneracy of the electronic states of the PbSe NPs [**121**] by adopting a four orbital (labeled by $a, b = 1, 2, 3, 4$) Hubbard model with diagonal disorder. [**122**] The Hamiltonian reads:

$$H = \sum_{\langle i,j\rangle,a,\sigma} t_{ij} d^{\dagger}_{i,a,\sigma} d_{j,a,\sigma} + \sum_{i,a,\sigma} (w_i - \mu) n_{i,a,\sigma} + \sum_{a} U n_{a,\uparrow} n_{a,\downarrow} + \sum_{a \neq b,\sigma,\sigma'} U n_{a,\sigma} n_{b,\sigma'}. \tag{4.4}$$

Here $\langle i, j\rangle$ label nearest neighbor sites, $n_{i,a,\sigma} = d^{\dagger}_{i,a,\sigma} d_{i,a,\sigma}$ is the density of electrons of spin σ in orbital a on site i, μ is the chemical potential, t_{ij} is the nearest neighbor hopping, and U is

the Coulomb repulsion. The disorder is introduced through the random site potential energy w_i, independent of orbital and spin index. For further details, see the SI.

The NP solid is on a regular lattice to start from a bona fide metallic state. We explore the combined effect of Coulomb repulsion and site energy disorder. We simulate PbSe NPs by associating the on-site Hubbard repulsion U with the NP charging energy by taking $U = E_c = 100$ meV, and the kinetic term with the NP-NP hopping amplitude of $t = 7$ meV, making $U/2t = 7$. These parameters match those of Fig. 2, and thus our Hubbard model is to be viewed as a quantitative modeling of the PbSe NP solid.

Since $t/U << 1$, the Hubbard model is in strong coupling. Therefore, we adopt the Dynamical Mean Field Theory (DMFT), extended to include disorder effects. [**107**, **108**, **109**, **123**]

The DMFT approach maps the original lattice model onto an auxiliary quantum impurity model supplemented with a self-consistency condition. The quantum impurity problem is then tackled by numerical simulations that we performed using the continuous-time quantum Monte Carlo (CTQMC) method, [**124**, **125**] described in Ref.**126**. That method samples a diagrammatic expansion of the partition function in powers of the impurity-bath hybridization. For simplicity, for the non-interacting electrons we adopt a semi-circular density of states (DOS) of bandwidth $4t$, since single-site DMFT is not sensitive to the shape of the non-interacting DOS. DMFT is exact in infinite dimensions, and it has been shown to remain a good approximation for lower dimensional systems whose physics is local, as is the case for the present Mott system. The disorder is introduced through a random site energy with a uniform distribution in the interval $[-W, W]$ (see SI for details).

Fig. 4 shows the electron mobility and the chemical potential μ of this Hubbard model as a function of the filling n for the clean and disordered cases, at T/t=0.02. In the clean case, μ shows a jump at $n = 1$: this indicates the emergence of a Mott gap that localizes the electrons. [**122**] This is a remarkable result, as our DMFT technique finds this Mott-localized phase at the band filling of 1/8, whereas band structure calculations for PbSe, or traditional Hubbard mean-field theories would not find such a Mott insulator below the customary band filling of 1/2. So, our DMFT work establishes PbSe as a Mott system, where correlation effects play out in 4-fold degenerate orbitals.

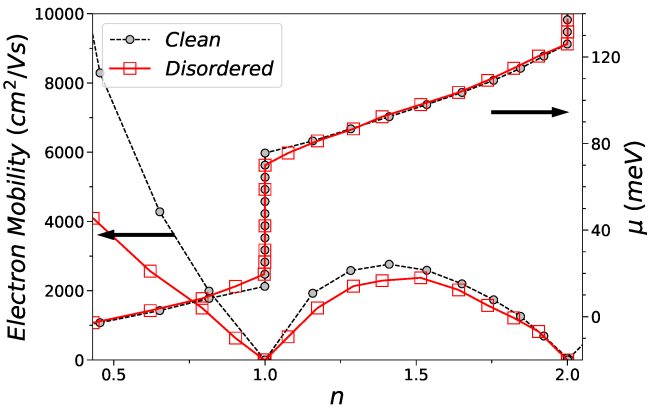

FIGURE 4.4. Mobility and chemical potential μ as filling scans from the Metallic Phase through the Mott gap.

At finite temperatures, this Mott gap makes the mobility exhibit a minimum as the filling crosses n=1. Clearly, DMFT established that the Mott gap/Coulomb blockade also suppresses the mobility in the metallic phase when the filling is scanned across $n = 1$, just like in the insulating phase (cf. Fig. 2).

A main result of the DMFT study is that the clean trends persist even for a substantial disorder $W/2t = 1$. Indeed, the Mott gap (jump of μ) at $n = 1$ only decreases by a small amount and remains robust. This is reasonable since $W/2t = 1 << W_c(Mott)/2t = 3.5$. At the same time, the mobility away from $n = 1$ is reduced much more notably because the $W/2t = 1$ disorder is relatively closer to the off-commensuration MIT at $W_c(MIT)/2t = 1.5$. Finally, Fig. 4 shows that the relative reduction of the mobility by the disorder is strongest at small n. This makes physical sense, since at small n the Fermi energy becomes comparable to the disorder, and thus the relative importance of the disorder grows. To our knowledge, the present DMFT study is the first one done for a multi-orbital model with disorder as a function of electron filling.

The here-used coherent potential CPA-DMFT method does not capture Anderson localization. While "typical medium" DMFT theories were proposed to capture a Mott-Anderson transition, this issue remains debated. [**108**, **127**, **128**, **129**, **130**, **131**, **132**, **133**]

4.3. Conclusions

: We now bring together all the scans of our complementary HINTS and DMFT work and construct the phase diagram of PbSe NP solids on the filling–disorder plane, shown in Fig. 5.

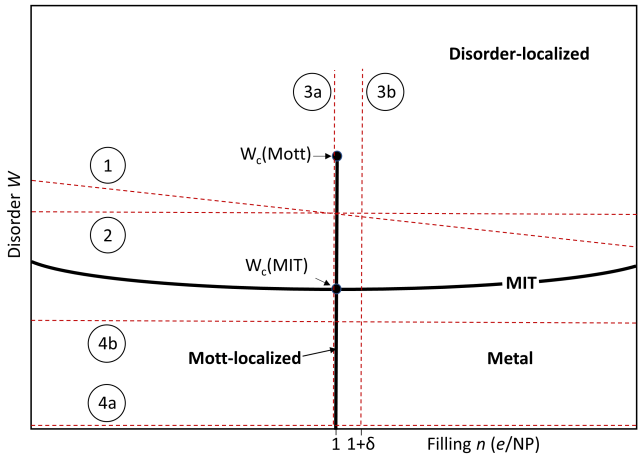

FIGURE 4.5. Qualitative phase diagram of NP solids in the (disorder W–filling n) space, for $U >> W$. The red dashed lines report the scans in the correspondingly labeled figures.

We distinguished a Disorder-driven MIT at $n \neq 1$, and an Interaction-driven MIT at $n = 1$. In particular, at $n = 1$, HINTS showed that at large interactions the Mott-localized–to–Disorder-localized transition occurs with a persistent gap. We complemented the studies building from the localized phases with studies building from the extended phase. Reassuringly, the complementary studies produced the same qualitative scenarios, as illustrated by the strikingly similar behavior of the mobility in Figs. 2 and 4.

The totality of our studies demonstrated that adapting the vast body of knowledge developed for the disordered Mott-Hubbard model for NP solids can and will produce many new insights into the physics of NP solids, and thus can be used to develop strategies to improve their optoelectronic properties.

CHAPTER 5

Structural Characterization of a Polycrystalline Epitaxially-Fused Colloidal Quantum Dot Superlattice by Electron Tomography

5.1. Introduction

Colloidal semiconductor quantum dots (QDs) exhibit intriguing photophysical properties relevant to next-generation solar cells, [**134**, **135**, **136**, **137**] field-effect transistors, [**138**, **139**] photodetectors [**140**, **141**] and lasers. [**142**, **143**] While improvements in QD processing, electronic performance and stability are ongoing, the use of QDs in many optoelectronic devices is limited by poor charge transport relative to bulk semiconductors. Poor transport is in part caused by energetic disorder arising from variations in QD size, spacing and other types of spatial disorder. [**20**, **91**, **144**] Epitaxially-fused PbX (X = Se, S) QD superlattices (epi-SLs) consist of PbX QDs that are arranged in a periodic lattice and epitaxially interconnected (necked or partially fused) to form a porous single crystal of "confined-but-connected" QDs. Epi-SLs promise to combine the tunable optical properties and processability of QDs with the high-efficiency band-like transport of bulk semiconductors. [**145**] However, charge transport studies have so far failed to demonstrate band-like transport in epi-SLs, probably because structural defects from the atomic scale to the mesoscale disrupt the SL periodicity and localize charge carriers. [**146**, **147**]

Making PbX QD epi-SLs with larger lateral grain sizes is important for reducing the density of inter-grain structural defects (*e.g.*, grain boundaries, amorphous regions, and voids), but it is the several types of intra-grain defects that conspire to degrade spatial order within the grains, destroy mini-bands, and prevent the emergence of delocalized states. [**20**,**91**,**146**] Intra-grain defects include variations in QD and neck size and shape, missing necks, missing QDs (vacancies), misaligned QDs (edge dislocations, screws dislocations, and zig-zag jitter), larger-scale wave-like oscillations in QD position that result from flow of the QD film on the liquid surface (meander), and variations

in the surface coverage of ligands, ions, and traps, all of which will scatter carriers and disrupt SL periodicity to some degree. Most of these defects have been observed in 2D epi-SLs (QD monolayers), which are readily imaged by conventional transmission electron microscopy (TEM) and scanning transmission electron microscopy (STEM). [**20**,**147**,**148**,**149**,**150**,**151**,**152**,**153**,**154**, **155**, **156**, **157**, **158**] Transport measurements of 2D epi-SLs show that carriers are localized, and several groups have proposed that missing necks are a primary cause of carrier localization in these materials. [**20**, **149**] Furthermore, the electronic coupling of necked QDs is expected to be sensitive to neck polydispersity (length, width, atomic coherence, and faceting) and the number of nearest neighbor QDs. [**20**]

While 2D epi-SLs can be structurally characterized using traditional electron microscopy, imaging the internal details of 3D epi-SLs is more challenging. [**153**, **159**, **160**, **161**] Neck connectivity and projected neck size in 2D epi-SLs have been directly imaged by (S)TEM, [**20**,**149**,**157**] and the three-dimensional structure of these necks was deduced from single images by high-angle annular dark-field (HAADF) STEM atom counting reconstruction. [**153**] To date, structural characterization of 3D epi-SLs has been almost exclusively limited to X-ray scattering and conventional electron microscopy imaging/diffraction methods, [**147**, **161**, **162**, **163**] neither of which can visualize the intra-grain neck network or internal structural defects that are so important for understanding carrier delocalization in these materials. Electron tomography (ET) is a suitable tool for the near-atomistic structural characterization of 3D epi-SLs. The Vanmaekelbergh group has previously used ET to establish the basic unit cell of non-fused 3D binary [**164**, **165**] and ternary [**166**] QD SLs, 2D honeycomb epi-SLs, [**151**] and thin multilayer honeycomb epi-SLs. [**167**] Savitzky *et al.* reported a tomogram of a fused 3D PbS QD SL made at high pressure, but no assessment of necks or structural defects was presented. [**168**]

Here we present an in-depth and quantitative structural analysis of a 3D PbSe QD epi-SL using electron tomography. We show that with a full-tilt HAADF ET reconstruction of a disc-shaped epi-SL film (120 nm in diameter $\times$ 38 nm tall), we are able to achieve sufficient spatial resolution (0.65 nm) to determine the position of all 1,846 QDs and the size and shape of all necks in the sample. From the center-of-mass coordinates of the QDs, we find that the sample consists of three SL grains and assign the unit cell and in-plane crystallographic orientation of each grain

as well as the 3D structure of the grain boundaries. The epi-SL grains have a distorted simple cubic structure with lattice parameters in agreement with our previous results. [**162**] Maps of the neck locations and diameters reveal that the sample has an average of 3.7 necks per QD (giving an overall network connectivity of 72%) and an average neck diameter of 4.1 nm (64% of the QD diameter). The three grains show similar distributions of neck number (necks per QD) but very different distributions of average neck diameter, reflecting significant inhomogeneity between the adjacent grains. We discover a weak positive correlation between neck number and diameter and a strong negative correlation between neck number and both the average and standard deviation of the nearest neighbor QD distance, indicating that QDs with more necks tend to have more ordered local environments. Kinetic Monte Carlo charge transport simulations show that the SL grain boundaries have little impact on carrier mobility because the three grains are interconnected by many necked QDs. The detailed and comprehensive understanding of various structural features gained from our statistical analysis of this relatively disordered polycrystalline sample can potentially inspire synthesis of 3D PbX QD epi-SLs of better structural perfection for realizing delocalized charge transport.

5.2. Experimental

5.2.1. Materials. Lead oxide (PbO, 99,999%), Lead iodide (PbI_2, 99.9985%, purchased from Alfa Aesar), oleic acid (OA, technical grade, 90%), diphenylphosphine (DPP, 98%), 1-octadecene (ODE, 90%), ethanol (99.5%, anhydrous), ethylene glycol (EG, 99.8%, anhydrous), acetonitrile (99.99%, anhydrous), hexanes (≥99%, anhydrous), toluene (99.8%, anhydrous), (3-mercaptopropyl) trimethoxysilane (3-MPTMS, 95%), and N,N-dimethylformamide (DMF, 99.8%, anhydrous) were purchased from Sigma Aldrich and used as received. Trioctylphosphine (TOP, technical grade, >90%) and selenium (99.99%) were acquired from Fluka and mixed for 24 hours to form a 1 M TOP-Se stock solution. Ethylenediamine (EDA, >98.0%, anhydrous) was purchased from TCI and mixed with acetonitrile in a 1:1 volume ratio to make a 7.5 M EDA stock solution.

5.2.2. Quantum Dot Sythesis. PbSe QDs were synthesized and purified using standard air-free techniques. PbO (1.50 g), OA (5.00 g), and ODE (10.00 g) were mixed and degassed in a three-neck round-bottom flask at room temperature. The mixture was heated to 120 °C under

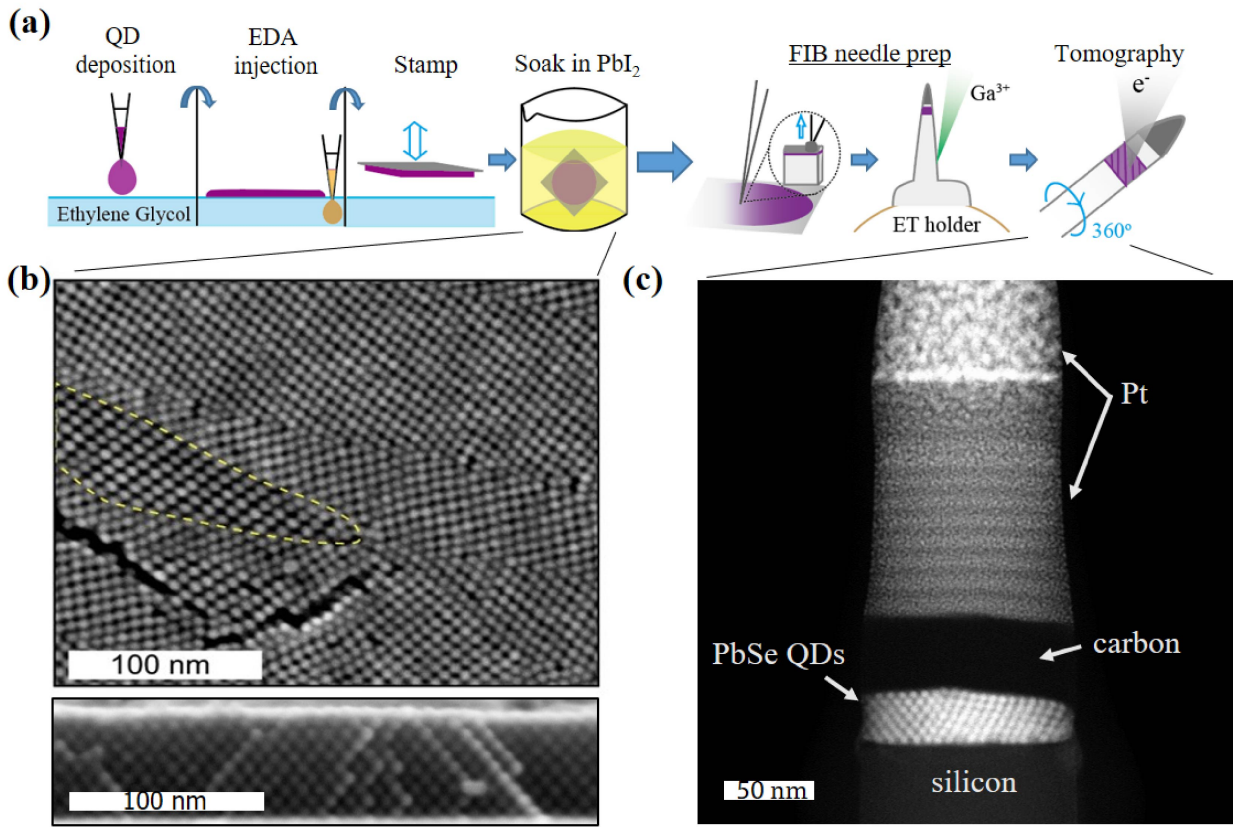

FIGURE 5.1. Fabrication of the PbSe QD epi-superlattice tomography sample. (a) Sample fabrication. (b) Plan-view and cross-section SEM images of a different region of the epi-SL film. The film is a polycrystalline SL with SL grains of two different in-plane orientations, previously assigned to the $(100)_{SL}$ and $(01\bar{1})_{SL}$ projections of a distorted simple cubic SL. [**162**] Most of the SL grains in this image have a $(100)_{SL}$ orientation. The dashed yellow line encircles a $(01\bar{1})_{SL}$-oriented grain. Scale bars are 100 nm. (c) HAADF-STEM image of the needle-shaped tomography sample with disc-shaped epi-SL layer and all layers labeled. Scale bar is 50 nm.

vacuum to form dissolved $Pb(OA)_2$ and dry the solution. After 1 hour at 120 °C, the $Pb(OA)_2$ solution was heated to 180 °C under argon flow and 9.5 mL of a 1 M solution of TOP-Se containing 200 μL of DPP was rapidly injected into this hot solution. An immediate darkening of the solution was observed, and the QDs were grown for 105 seconds at ∼160 °C. The reaction was quenched with a liquid nitrogen bath and injection of 10 mL of anhydrous hexanes. QD purification and SL fabrication were performed in glove boxes with ¡0.5 ppm O_2 content. The QDs were purified by two rounds of precipitation/redispersion using ethanol/hexane and stored as a powder in the glove box.

5.2.3. Substrate preparation. A single-side polished Si substrate was cleaned using 10 minutes of sonication in acetone, Millipore water, and then isopropanol, followed by drying in a stream of flowing air. The cleaned substrate was immersed in a 100 mM solution of 3-MTPMS in toluene for 1 hour to functionalize its native SiO_x surface for improved epi-SL adhesion, then rinsed with neat toluene and dried in flowing air.

5.2.4. Superlattice fabrication. An oleate-capped superlattice was prepared in the glovebox by drop casting 70 μL of a 4 g/L dispersion of PbSe QDs in hexanes onto 6 mL of ethylene glycol (EG) in a Teflon well (3.5 $\times$ 5 $\times$ 1 cm). After depositing the QD solution, the well was immediately covered with a glass slide. The hexane evaporated over 30 minutes, resulting in a smooth, dry QD film floating on the EG surface. The glass slide was then removed and 0.1 mL of a 7.5 M solution of ethylenediamine in acetonitrile was slowly injected (5-10 sec) into the EG under the QD film using a 500 μL Hamilton syringe. After 30 seconds of exposure to EDA, the resulting epi-SL film was stamp transferred to the Si substrate using a vacuum wand, rinsed vigorously with acetonitrile and dried under flowing N_2. The epi-SL film was then immediately immersed in a 10 mM solution of PbI_2 in DMF for 5 minutes, rinsed thoroughly with acetonitrile and dried under flowing N_2. This procedure is nearly identical to the one used in our previous report [**162**] and yields epi-SL films with similar SL unit cell, grain size, and homogeneity, including degree of QD necking, coverage of the substrate, and density of cracks. However, the film for this tomography study is somewhat thinner (40 nm *vs.* 50-80 nm) and have a higher density of intra-grain extended defects (e.g., partial twins) because it was prepared in a glove box with a higher O_2 concentration (5 ppm *vs.* ¡ 0.1 ppm).

5.2.5. Basic characterization. Optical absorbance measurements of QDs dispersed in TCE were performed with a PerkinElmer Lambda 950 spectrophotometer. Neat TCE served as the background for the solution measurements. Scanning electron microscopy was performed on both an FEI Magellan 400L XHR SEM operating at 10 kV and 25-50 pA and a JEOL JEM-2800 TEM (with a secondary electron detector) operated in STEM mode with a 1.0 nm probe size.

5.2.6. Grazing incidence small-angle X-ray scattering. GISAXS measurements were performed on Beamline 7.3.3 of the Advanced Light source (ALS) at Lawrence Berkeley National

Laboratory using 10 keV monochromatic X-rays (λ = 1.24 Å) with an energy bandwidth of 1%. For GISAXS measurements, SL films were prepared on Si substrates and transported with the QD suspensions to the ALS under nitrogen to minimize air exposure prior to measurement. However, measurements were performed in air. A Dectris Pilatus 2M detector with a pixel size of 0.172 × 0.172 mm and 1475 × 1679 pixels was used to record the 2D scattering patterns. A silver behenate standard was used to determine the sample-to-detector distance and beam center. Exposure times ranged from 0.2 to 30 s. The grazing angle of incidence was varied from 0.2° to 0.3°. Manual pattern fitting was performed using the IndexGIXS software package provided by Detlef Smilgies of the Cornell High Energy Synchrotron Source. The critical angles of the films were fit empirically (0.195° for the oleate-capped SLs and 0.21° for the epi-SLs) to capture the breadth of the Yoneda band.

5.2.7. Tomography needle sample preparation. An area of the epi-SL film suitable for FIB milling was located by SEM and tagged with a Pt fiducial marker deposited by electron-beam induced deposition (EBID) in an FEI Quanta 3D FEG DualBeam microscope. The sample was then coated with 50 nm of carbon using the pulse plasma mode of a Leica ACE200 evaporator and returned to the DualBeam for FIB milling, lift-out, and final needle preparation. Prior to milling, a ∼200 nm Pt capping layer was deposited onto the carbon-coated sample by EBID, followed by an additional ∼2000 nm of Pt deposited by ion beam induced deposition (IBID). The carbon layer serves primarily to enhance STEM imaging contrast by separating the epi-SL layer from the high-Z protective Pt capping layer. The area of interest was then FIB milled into a wedge shape (10 μm × 6 μm × 2 μm), lifted-out with an OmniProbe 400 nanomanipulator, ion welded to the tip of a sample holder for needle tomography samples (Single Point Tip, Hummingbird Scientific), and FIB milled again into a ∼130 nm diameter needle (Fig. S2). Milling was performed in several stages. The wedge was first milled into a pillar shape (1 μm diameter) using a 0.3 nA ion beam at 30 keV accelerating voltage, then thinned to a ∼200 nm diameter needle using 50 pA at 16 keV. Finally, a 5 minute ion beam shower (25 pA at 5 keV) was employed to sharpen the needle to ∼130 nm and remove surface damage. The finished needle contained a disc-shaped epi-SL layer (38 nm tall × 128 nm in diameter) for tomographic analysis.

5.2.8. HAADF-STEM Electron Tomography. The needle sample was mounted on the rotation axis of a Hummingbird Scientific single-tilt tomography holder (1000 Series) and imaged in a double aberration corrected JEOL JEM-ARM 300F TEM operated at 300 keV in STEM mode ($\sim$25 mrad semi-convergence angle). Two series of images were acquired, with HAADF and bright-field data recorded simultaneously (2k $\times$ 2k images) at each tilt angle. The first series consisted of 145 HAADF images spanning tilt angles over -78 to 67 degrees in 1 degree steps. The sample was then removed from the microscope, manually rotated on the sample holder by 86 degrees, and re-imaged from -68 to 78 degrees in 2 degree steps (resulting in 73 additional images). All 2D and 3D image processing was conducted in MATLAB unless otherwise noted. The two tilt-series were then merged using cross-correlation comparison (Fig. S4). The merged tilt-series include 181 images covering tilt angles from 0° to 226°. The image stack was then aligned vertically (along the rotation axis) by iteratively shifting the images to maximize the value of the 2D normalized cross-correlation function between adjacent images in the stack. Pixels outside of the epi-SL film were excluded from this cross-correlation calculation in order to maximize the quality of the vertical image alignment. Horizontal alignment of the images (normal to the rotation axis) was accomplished by converting each image to a 1D intensity profile and shifting the images to maximize the match between the 1D curves. The aligned image stack was then processed through two iterations of a Wiener image filter to remove noise. Tomographic reconstruction was carried out on the aligned and de-noised tilt-series using 200 iterations of the simultaneous iterative reconstruction technique (SIRT) in the ASTRA toolbox. [**169**, **170**] The raw reconstructed volume consisted of 2048 $\times$ 2048 $\times$ 700 voxels with edge lengths of 1 Å. The spatial resolution of this reconstruction was evaluated by the Fourier shell correlation (FSC) method to be 6.5 Å (Fig. S5).

The raw reconstruction was processed in two different ways. For analysis of the QD necks, the reconstruction was simply smoothed by a nonlinear anisotropic diffusion filter. Image processing for analysis of the QD positions was more involved. The raw tomogram was first filtered with a morphological 3D top-hat filter to minimize reconstruction intensity attenuation and enhance contrast. A top-hat filter was used to retain edge contrast instead of the more common Fourier filter [**171**] because Fourier filtering would erroneously remove necks between QDs and other important structural features present in the raw tomogram. To better emphasize the QD positions, the filtered

tomogram was convolved with a spherical 6.0 nm diameter QD kernel with a homogeneous intensity profile to obtain a 3D map of normalized cross-correlation (NCC) coefficients indicating the center of mass of each QD in the sample. Use of the 6.0 nm QD template is justified by the analysis of the average QD size and polydispersity from conventional dark-field STEM images (pixel size of 0.2 nm) of a different area of the same sample (Fig. S6). Prior to data analysis, the outer 6 nm of the cylinder-shaped tomogram was digitally removed to exclude QDs near the surface of the sample that were potentially deformed by the FIB milling process. To automate the measurement of neck dimensions, a script was written that defines a plane normal to each inter-QD axis and slides this plane along the axis to locate the minimum neck area. The neck diameter was then determined as the diameter of a circle of the same area.

5.2.9. Mobility Simulation. Mobility simulations were performed utilizing the Hierarchical Nanoparticle Transport Simulator (HiNTS) kinetic Monte Carlo code, developed by some of us previously. [**60**, **172**] HiNTS simulates transport by developing several modeling layers and then integrating them into a hierarchical scheme. After the energetics of the individual QDs is computed by *ab initio* methods, the QD-to-QD transitions of the charges are described by the following two mechanisms:

(1) Miller-Abrahams single phonon-assisted hopping between nearest neighbor QDs:

$$\Gamma_{\mathrm{i}\to\mathrm{j}} = \begin{cases} \nu g_{\mathrm{ij}} \beta_{\mathrm{ij}} \exp\left(\frac{-\Delta E_{\mathrm{ij}}}{k_b T}\right) & \text{if } \Delta E_{\mathrm{ij}} > 0, \\ \nu g_{\mathrm{ij}} \beta_{\mathrm{ij}} & \text{if } \Delta E_{\mathrm{ij}} \leq 0 \end{cases} \tag{5.1}$$

where ν is an attempt frequency, chosen to be $10^{12}\mathrm{s}^{-1}$, g_{ij} is the product of the initial density of states on $\mathrm{QD_i}$ and the final density of states on $\mathrm{QD_j}$, and β_{ij} is the tunneling amplitude evaluated using the WKB approximation as $\beta_{\mathrm{ij}} = \exp\left(-2\Delta x\sqrt{\frac{2m^*\left(E_{\mathrm{vac}}-E_{\mathrm{ij}}\right)}{\hbar^2}}\right)$. Here Δx is the minimal surface separation of the QDs. m^* is the effective mass of electrons in the tunneling medium, approximated as $.05m_{\mathrm{e}}$, the effective mass of electrons in bulk PbSe. $\mathrm{E_{vac}}$ is the vacuum energy level that is set to be zero as all other energy levels are defined relative to the vacuum. $\mathrm{E_{ij}}$ is the tunneling energy, taken to be the average of the initial and final states of the tunneling transition: $E_{\mathrm{ij}} = \frac{E_{\mathrm{i}}+E_{\mathrm{j}}}{2}$, where $\mathrm{E_i}$ and $\mathrm{E_j}$ are the energy levels of $\mathrm{QD_i}$ and $\mathrm{QD_j}$. ΔE_{ij} is the total energy difference associated

with an electron transitioning from QD_i to QD_j: $\Delta E_{ij} = \Delta E_{ij}^{band} + \Delta E_{ij}^{charging} + \Delta E_{ij}^{voltage}$, where ΔE_{ij}^{band} is calculated using the one-electron band energies of the QDs determined by *ab initio* methods, [**173**] $\Delta E_{ij}^{charging}$ is calculated using the charging energies of the QDs as determined by a hybrid empirical-perturbative method, [**174**] and $\Delta E_{ij}^{voltage}$ is the energy difference due to the applied voltage. In general, the QD-QD hopping can be nearest neighbor or variable range hopping. Either hopping process can involve an elastic reorganization of the QD atoms, or processes other than Miller-Abrahams, such as that described by Marcus theory. Finally, the long-range part of the Coulomb interaction may or may not be included. Of the eight possible combinations, for example, [**175**] we investigated the intriguing process of variable range hopping with long-range Coulomb interactions and the Marcus reorganization process. HiNTS is capable of accommodating any of these eight combinations. We chose the simplest Miller-Abrahams process because both variable range hopping and Marcus processes have been shown to become important only at low temperatures, whereas our experiments were performed at room temperature. Indeed, experiments on QD lattices regularly report the standard activated, Miller-Abrahams temperature dependence around room temperature. [**104**]

(2) Tunneling through the neck of epitaxially-fused QDs:

$$\Gamma_{i\to j} = \begin{cases} \frac{2\pi}{\hbar}|t|^2 g_{ij} \exp\left(\frac{-\Delta E_{ij}}{k_b T}\right) & \text{if } \Delta E_{ij} > OE, \\ \frac{2\pi}{\hbar}|t|^2 g_{ij} & \text{if } \Delta E_{ij} \leq OE \end{cases} \tag{5.2}$$

where $|t|$ is the QD-QD tunneling matrix element, and OE is an overlap energy. This transition channel represents that when a neck is formed between two QDs, their electronic states overlap and therefore hybridize. This hybridization induces a perturbation of the energy levels of the individual QDs, which we model by an overlap energy OE that is proportional to the neck diameter. The electronic states of those pairs of QDs whose energy level difference is less than OE: $\Delta E_{ij} \leq OE$, hybridize to such a degree that they support a metallic QD_i-to-QD_j transition instead of a hopping one, paving the way toward the formation of a mini-band. The tunneling matrix element $|t|$ depends on the wavefunction overlap between the necked QDs. For its calculation, we adopt the

approximation of Fu *et al.*: [**176**]

$$|t| = \frac{9\hbar^2 n\rho^3}{m^* d^2} \tag{5.3}$$

where n is the average electron volume density of the two quantum dots, ρ is the neck radius, m^* is the effective electron mass, and d is the average QD diamter. HiNTS simulates nearest neighbor transitions and interactions; it does not include transitions to and interaction with farther neighbors.

On the next HiNTS modeling layer, a QD epi-SL, is constructed. Simulations were performed on three types of epi-SL samples. First, the replica of the tomography sample was generated using the experimentally determined center-of-mass coordinates, QD diameters, and neck map of all three SL grains. Since the circular shape and uneven periphery of the tomography sample would make it harder to set up controlled transport simulations, QDs at the periphery of the sample were removed to reduce the simulation volume to the well-defined central cuboid of the tomography sample. To develop a comparative analysis of the transport of this tomography sample, we next generated two ensembles of over a thousand samples each to form a comparison basis. The first ensemble consisted of monocrystalline epi-SLs with the lattice parameters and neck statistics of grain I of the tomogram. The second ensemble consisted of bicrystalline epi-SLs with the same lattice parameters and neck statistics of grain I, but bisected by a plane of missing necks normal to the transport direction to create a necking grain boundary. The QDs in the latter two types of samples were assigned a diameter and lattice displacement vector according to the experimentally-determined Gaussian distributions.

Electron transport was simulated by first randomly placing electrons on QDs to fill the samples with a predetermined density of electrons. Based on our previous work, we chose the electron density to be 0.5 electrons per QD, remaining far from commensuration to avoid Coulomb blockade effects. [**172**] A small voltage of 1 mV was then applied across electrical contacts on opposite sides of each sample to induce electron transport. Periodic boundary conditions were used. Throughout the simulation, we checked and ensured that the current-voltage characteristic stayed in the linear regime. Finally, the mobility was determined according to the following equation:

$$\mu = \frac{\text{electrons collected at drain electrode} \times l}{\text{total number of electrons} \times t \times E} \tag{5.4}$$

TABLE 5.1. Lattice constants of SL grains I and II as determined from statistical analysis of the tomogram. GISAXS data is from refrence **31**.

Grain	**a/nm**	**b/nm**	**c/nm**	α	β	γ
I	6.4±0.6	6.4±0.6	5.9±0.7	102±8°	95±7°	96±7°
II	6.3±0.6	6.5±0.6	6.2±0.7	103±9°	107±5°	97±7°
GISAXS		6.6 ± 0.2			99 ± 2°	

where l is the length of simulation box normal to the electrodes, t is the simulation time, and E is the applied electric field. The transport across every sample in both ensembles was simulated.

5.3. Results and Discussion

5.3.1. SL Unit Cell and Disorder. Oleate-capped PbSe QDs with a diameter of 6.4 ± 0.3 nm were used to fabricate a 3D polycrystalline epi-SL film via self-assembly and ligand exchange on a liquid ethylene glycol substrate (Fig. 5.1a and Methods). [**147**,**148**,**177**,**178**] After triggering epitaxial fusion of the QDs with EDA, the epi-SL film was stamped onto a silicon substrate, immersed in a solution of PbI_2 to remove additional oleate ligands, and milled by focused ion beam (FIB) into a 128 nm diameter disc embedded in a nanoscale needle for full-tilt electron tomography studies (Fig. 1a). Scanning electron microscopy (SEM) images of the epi-SL film and the finished tomography needle are presented in Fig. 1b and 1c, respectively. An optical extinction spectrum of the QDs in solution and additional details about the preparation of the tomography sample are provided in the Supporting Information (Figs. S1-S2).

We acquired a ±113° single-axis tilt-series of 181 images of the sample using high-angle annular dark-field scanning transmission electron microscopy (HAADF-STEM) in a double aberration-corrected microscope (see Methods and Figs. S3-S4). Tomographic reconstruction of the sample was accomplished using the SIRT algorithm after careful image alignment and noise filtering. The final tomogram (Fig. 5.2a and Movie S1) has a spatial resolution of 6.5 Å (∼1 unit cell of PbSe) as determined by the Fourier shell correlation (FSC) method (Fig. S5). This resolution is sufficient to unambiguously identify the center of mass (CoM) coordinates of all 1,846 QDs in the sample volume, as illustrated in Fig. 5.2e and f.

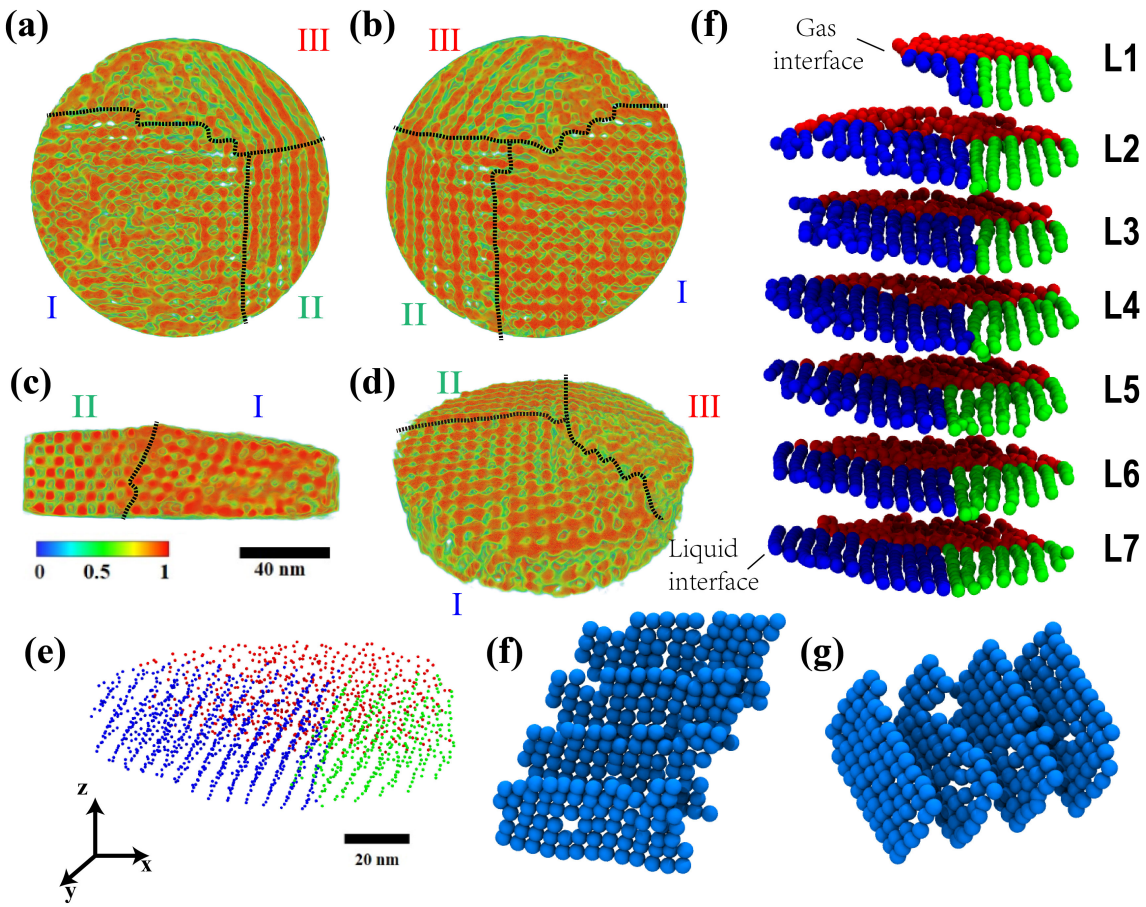

FIGURE 5.2. The epi-SL tomogram and QD positions. (a) Top, (b) bottom, (c) cross-section, and (d) perspective views of the tomogram of the epi-SL film. The color scale denotes the normalized electron density in units of e^-/nm^3. Dashed lines represent grain boundaries between the three SL grains (labeled grain I, II, and III). The scale bar is 40 nm. (e) Perspective image of the center of mass coordinates of all QDs in the sample. Each QD is represented by a sphere with a diameter of 1 nm (for ease of viewing). The QDs are color coded according to their location in grain I (blue), grain II (green), or grain III (red). The scale bar is 20 nm. (f) Exploded view of the seven QD layers of the sample to illustrate the internal structure of the epi-SL film. Each QD is represented by a 6 nm diameter sphere (Fig. S6). Layer 1 (L1) is the top layer of the originally floating film (at the QD/gas interface), while layer 7 (L7) is the bottom layer of the film (at the liquid/QD interface). The QDs are color coded according to panel e. (f-g) Representative monolayers in grain I seperated along direction x and y, representing SL lattice planes of (f)$(100)_{SL}$ and (g)$(010)_{SL}$.

The CoM data were used to determine the size, shape, crystallographic orientation, and lattice parameters of the constituent SL grains as well as the presence of inter-grain defects (grain boundaries, amorphous domains, voids) and intra-grain defects. Visual inspection of Fig. 5.2 shows that

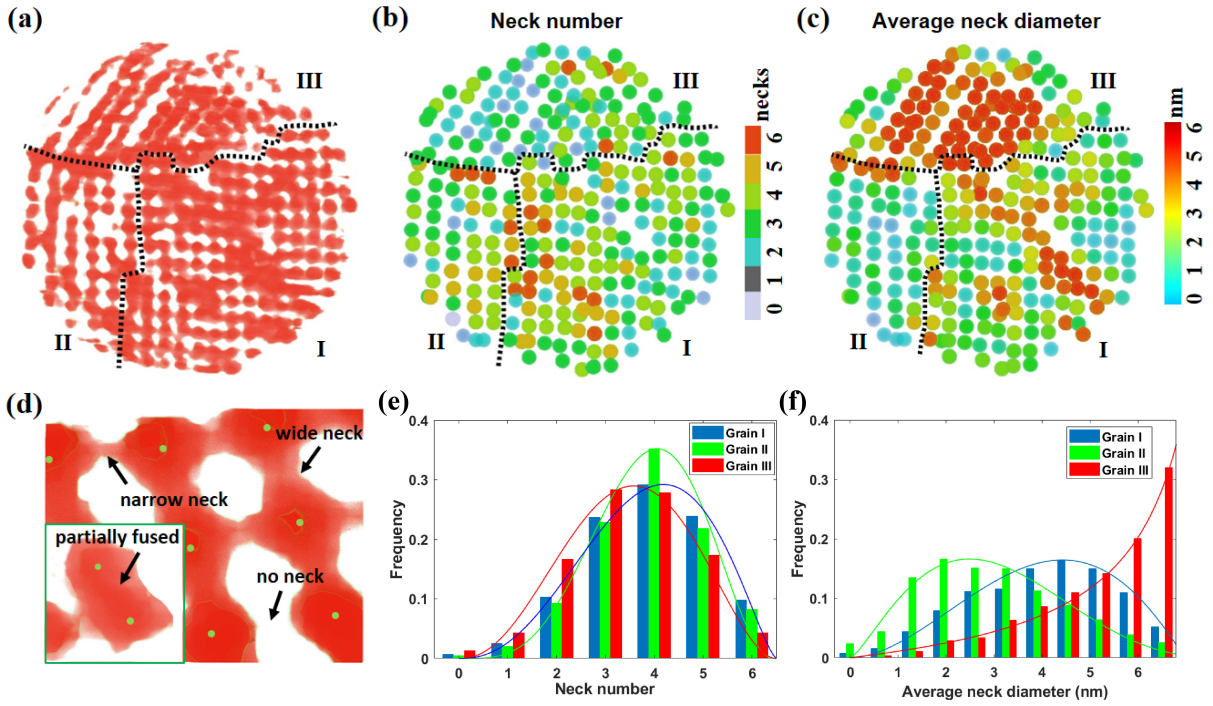

FIGURE 5.3. Analysis of the QD necks. (a) A slice of the tomogram through the middle of L4, showing in-plane necks between the QDs. (b) Heat map of the total number of necks for each QD in L4. The color scale is labeled. (c) Heat map of the average neck diamer for each QD in L4, including both in-plane and out-of-plane necks. The color scale is labeled. (d) Magnified isosurface views of two regions of the sample to illustrate typical neck polydispersity (narrow, wide, and missing necks) and a highly-fused pair of QDs (inset). The green dots denote the CoM of each QD. (e) Histograms of neck number for all QDs in grain I, II and III (inclusive of L1-7, not just L4). The solid curves are fitted beta distributions. (f) Corresponding histograms of average neck diameter. Fitting beta distributions are shown as solid curves. See Fig. S15 for histograms of the diameter of every neck in each grain.

the sample is seven QD layers thick and consists of three cylindrical sector-shaped (pie slice) SL grains that meet at a grain boundary triple junction near the center of the tomogram (dashed lines in Fig. 5.2a-d). While it is possible to assign the SL grain crystallography *a priori* from the CoM coordinates, we utilized the known unit cell of similarly-prepared PbSe QD epi-SLs [**162**] (distorted simple cubic with a = 6.6 ± 0.2 nm and $\alpha = 99 \pm 2°$; Fig. S7) to help interpret the tomogram. Grain I has a square-like lattice of QDs in each QD layer parallel to the substrate, so it is assigned as a $(100)_{SL}$-oriented SL grain, which is the most common grain orientation in this sample (see Fig. 1b). Grains II and III have 1D chains of QDs in each layer parallel to the substrate, with

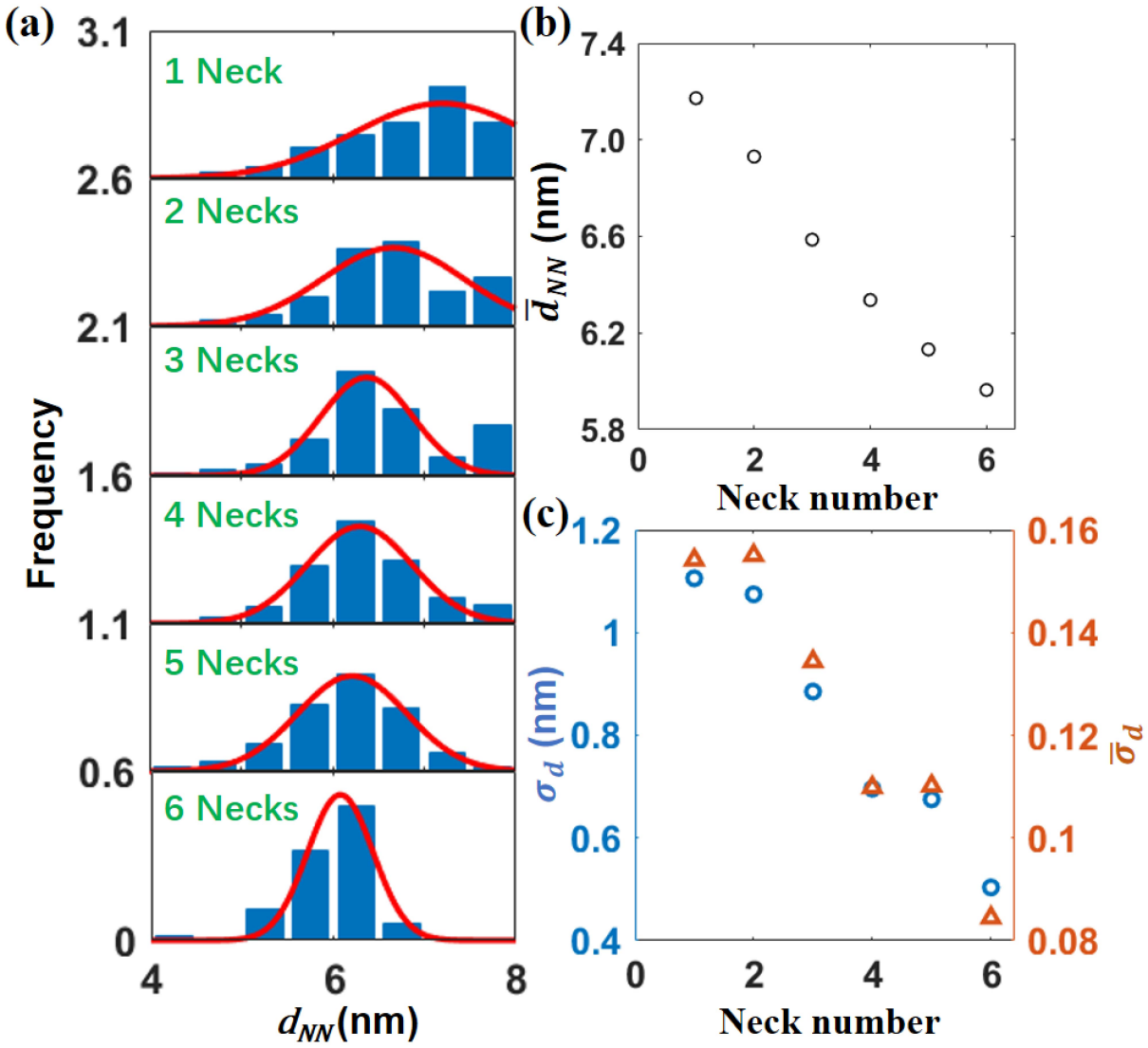

FIGURE 5.4. Correlation of neck number with nearest neighbor QD positional disorder. (a) Histograms of NN distance (d_{NN}) at each neck number for all of the QDs in grains I and II. Overlaid red curves are Gaussian fits. (b) Plot of the average NN distance ($\bar{d}_{\mathrm{NN}}$) versus neck number. (c) Plot of the standard deviation of the NN distance (σ_d) and the normalized standard deviation of the NN distance ($\bar{\sigma}_{\mathrm{d}} = \sigma_{\mathrm{d}}/\bar{d}_{\mathrm{NN}}$) versus neck number. $\bar{\sigma}_{\mathrm{d}}$ is a measure of the local disorder that is independent of differences in unit cell size.

an average QD spacing of a along the chains and approximately $\sqrt{2}a$ between the chains. This arrangement is consistent with the $(01\bar{1})_{\mathrm{SL}}$ projection of the distorted simple cubic SL unit cell, so grains II and III are assigned as $(01\bar{1})_{\mathrm{SL}}$-oriented SL grains (again, see Fig. 5.1b). Grains II

and III intersect at a planar coherent twin boundary indexed as 39°[001],(010) (most easily seen in Fig. 5.2a-b). Between grains I and II, it is harder to define a grain boundary inferface as we observe in Fig. 5.2c a relatively smooth change in the $[001]_{SL}$ lattice vector from grain II on the left side to grain I on the right side. A possible mechanism for such an inter-grain orientational transition is proposed in Fig. S8 involving a small rotation and a subsequent glide of the $(100)_{SL}$ plane. Grains I and III meet at a highly-corrugated boundary. All three grain boundaries are normal or nearly normal to the substrate and span the entire thickness of the QD film. SEM images of similar grain boundaries are presented in Fig. S9. In Fig. 5.2g and h, we show representative separated layers in grain I along two other SL lattice vectors showing QD vacancies from different perspectives. The randomness in the QD positional order is shown to occur in all directions. We also note that there is no significant difference in the vacancy rate for layers normal to different lattice vectors. Several slice views of the tomogram taken at different angles are shown in Fig. S10 emphasizing the orientational differences between SL unit cells of grain I and II and also how the lateral and vertical monolayers are connected through necks. See Movies S2 and S3 for additional continuous slices of this sample.

We determined the lattice parameters of grains I and II by compiling nearest-neighbor QD distances and bond angles from the CoM data (see Fig. S11 for labeling conventions). Grain III was excluded from this analysis due to its poor spatial order. Histograms of the QD distances and angles (Figs. S12-S13) show Gaussian distributions with average and standard deviation values summarized in Table 1. The lattice constants of grains I and II are in good agreement with the unit cell parameters of similar epi-SL films derived from ensemble GISAXS measurements, [**162**] so we conclude that these epi-SLs have essentially the same crystal structure, validating the recent GISAXS results. However, grains I and II also exhibit broad distributions of distances and angles indicative of a relatively large amount of positional disorder, as is apparent from Fig. 5.2. The spatial order of this sample is likely limited by the structural disorder of the original oleate-capped SL, the presence of several nearby grain boundaries, variability in QD neck number and diameter (*vide infra*), and (possibly) mechanical strain caused by sample preparation. Two additional aspects of the data are noteworthy. First, while grains I and II have very similar triclinic unit cells, they differ slightly in their β angle (Table 1). Such grain-to-grain variability is expected in polycrystalline

SLs due to local differences in grain nucleation and growth, especially when the SL grains are small and experience non-uniform stress. Electron tomography is one of the few techniques capable of detecting such minute structural differences between individual QD SL grains. Second, grain I is slightly compressed along the film normal with a smaller average lattice spacing in the c direction shown in Table 1. This is commonly seen for nanocrystal films prepared by solvent evaporation. [**179**, **180**, **181**, **182**]

5.3.2. Characterization of Neck Disorder. In addition to the positions of the QDs, the tomogram provides rich information about the crystalline connections (necks) between the QDs. Previous TEM studies have shown that the QDs in these SLs are epitaxially fused across their {100} facets. [**153**, **158**, **161**, **163**, **183**, **184**] The epitaxial necks likely dictate the strength and uniformity of electronic coupling within the epi-SLs, [**144**] so mapping the location and size of the necks is essential for understanding and optimizing the electronic properties of these materials. Electron tomography can directly visualize the necks and map the 3D neck network inside each SL grain. Fig. 5.3a shows a slice of the tomogram through the middle of L4 with the necks between the QDs clearly visible. We implemented an automated program to measure the cross-sectional area of every neck in the sample and assign each an effective diameter (Fig. S14). In our approach, any connection with an area smaller than the tomogram spatial resolution (0.43 nm^2, or about one PbSe unit cell) was considered to be absent (a "missing neck"). An example of a missing neck is shown in Fig. 5.3d.

Heat maps of the average neck diameter and the total number of necks for each QD in L4 are presented in Fig. 5.3b-c. Maps for all seven layers of the sample are compiled in Figs. S16 and S17. The 1,846 QDs in the sample have a maximum of 4,865 possible epitaxial necks (considering the six {100} facets of each QD and sample edge effects, vacancies, and voids). We observe a total of 3,471 necks, giving an overall network connectivity of 72%, well above the bond percolation threshold (p_c) of 25% for simple cubic lattices. [**185**] This estimate of neck connectivity is conservative because, as mentioned above, any neck smaller than the tomogram resolution ($\leq$3 Pb atoms wide) is not counted by our algorithm. Overall, the average number of necks per QD is 3.7 and the average neck diameter is 4.1 nm (64% of the QD diameter). Table 2 summarizes the neck statistics for the sample.

Figs. 5.3e and f show histograms of neck number and diameter for the three epi-SL grains in this sample. The neck number for all three grains follows a beta distribution (solid curves) with a peak at 3.5-4 necks per QD. Grain I has the largest fraction of QDs with high connectivity (five and six necks), while grain II has the largest fraction of QDs with intermediate connectivity (four necks) and the smallest fraction of QDs with low connectivity (three or fewer necks). Overall, grains I and II are quite similar with respect to neck number. In contrast, grain III has much poorer neck connectivity than grains I and II, with the smallest fraction of high-connectivity QDs and the largest fraction of low-connectivity QDs. Grain III is also dominated by QDs with very large neck diameters (see the J-shaped distribution in Fig. 5.3f). The low neck number and large fraction of heavily-fused QDs contribute to the poor spatial order of grain III. The average neck diameters of grains I and II also follow a beta distribution and are similarly polydisperse. These two beta distributions (grain I: $\alpha = 2.90$, $\beta = 2.25$; grain II: $\alpha = 2.10$, $\beta = 3.18$) are approximately mirror images of each other (Fig. 5.3f). Grain I has a larger fraction of thicker necks (¿4 nm) while grain II has a larger fraction of thinner necks (¡4 nm). The reason for these differences in neck diameter and number in adjacent epi-SL grains is unclear, but probably related to variability in the spatial order of the parent oleate-capped SL and the kinetics of the epi-SL phase transition. We attempted to determine a correlation between neck number and diameter to measure whether the number of necks on each QD determined the neck thickness. Supporting Information Fig. S18a shows this correlation for the full sample and for each of the grains, indicating little correlation between the number of necks and the neck thickness for each QD, but also clearly showing that the average neck thickness is consistent throughout the grain regardless of the number of necks. Understanding the origin of such differences between grains will require systematic study of many tomograms to establish statistical relationships.

We also investigated whether there are trends in the necking that depend on the position of the layer within the SL. Fig. S18b-c plot the average neck number and diameter for each of the seven QD layers of the film. We find that the neck number is essentially constant in the middle five QD layers of grains I and II, while the neck number is significantly lower in grain III. However, there is a reduced neck number in L1 (the top of the film) for grains I-III and L7 (the bottom of the film) for grain II and III, despite taking into account edge effects. We conclude that the top and

TABLE 5.2. Neck statistics.

Parameter	Grain I	Grain II	Grain III	Total
number of QDs	903	389	554	1846
QD number density ($\times 10^{18}$ cm^{-3})	3.9	3.7	3.5	3.7(3.5*)
space filling fraction	0.53	0.51	0.48	0.51
possible necks	2343	1028	1494	4865
observed necks	1760	774	959	3493
connectivity	75%	75%	64%	72%
average number of necks	3.8	4.0	3.4	3.7
average neck diameter(nm)	4.0	3.5	5.0	4.1

* from reference 31.

bottom monolayers of the epi-SL tend to have fewer necks per QD. For all three grains, the neck diameter is smaller in L1 and L7 and increases in the middle of the film(Fig. 5.4c). Interestingly, while neck number and neck thickness are not in general correlated, the number and thickness of necks is lower at the QD/liquid and QD/gas interfaces, which suggests that out-of-plane forces from adjacent layers are important for necking formation and order. One might also expect to observe a monotonic decrease in neck number and diameter along the film normal due to ligand (glycoxide and oleate) concentration gradients since the ligands diffuse into the SL from the QD/liquid interface. Our neck diameter profile suggests that no such concentration gradients exist in this sample, in agreement with recent infrared spectroscopy measurements showing homogeneous ligand exchange in films of similar thickness. [**162**]

We also explored the relationship between neck number and the local spatial order of the epi-SL. In the ideal averaged epi-SL unit cell (Fig. S7), each QD is necked to six nearest neighbors (NNs) located at a common center-to-center distance and fixed lattice angles. In contrast, QDs in real epi-SLs have distributions of neck number, NN distance, and lattice angles. These distributions provide a measure of the local (nanoscale) spatial disorder of the QD array. We reasoned that the distribution of NN distances and lattice angles should depend strongly on neck number because necks can form over only a narrow range of QD positions. Thus, QDs with high (low) connectivity should have more (less) ordered local environments. To assess the impact of neck number on local spatial order, we compiled histograms of the nearest neighbor distance (d_{NN}) as a function of neck number for all of the QDs in grains I and II (Fig. 5.4a). Grain III was again excluded from analysis

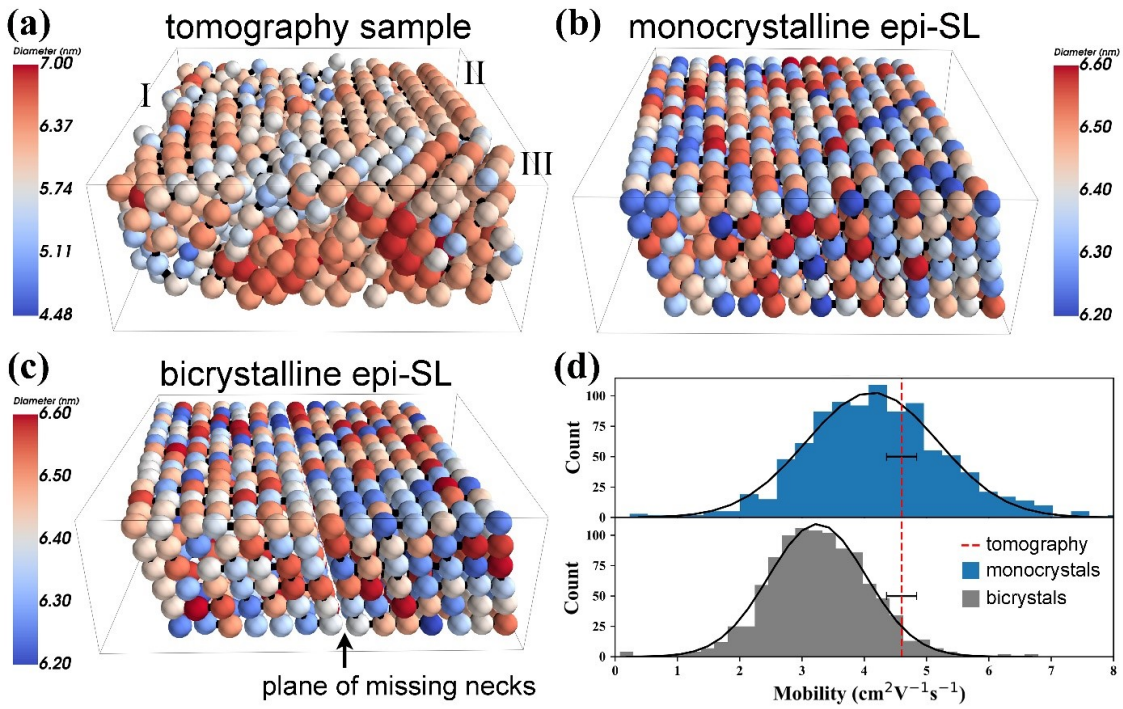

FIGURE 5.5. Transport simulation results. (a-c) Perspective views of the three types of simulated samples. (a) The tomography sample (trimmed from a disc into a cuboid). Grains I, II, and III are labeled. (b) A monocrystalline epi-SL. (c) A bicrystalline epi-SL. The monocrystalline and bicrystalline epi-SLs were generated using the lattice parameters, QD size distribution, QD positional disorder and neck statistics of grain I. The bicrystalline samples are bisected by a plane of missing necks (a necking grain boundary), which limits transport across this plane to hopping. Virtual electrical contacts are placed at the left and right sides of each sample. All simulation boxes are approximately 92×92×39 nm. (d) Comparison of the calculated electron mobility of the tomography sample (dashed red line), monocrystalline epi-SLs (blue bars) and bicrystalline epi-SLs (gray bars). The horizontal error bar represents the error in the mobility estimate for the tomography sample. Overlaid black curves are Gaussian fits of the histograms. The mobility for the monocrystalline and bicrystalline samples is 4.25 ± 1.25 cm^2/Vs and 3.28 ± 0.8 cm^2/Vs, respectively.

due to its poor order. We find that as neck number increases, the average NN distance ($\bar{d}_{NN}$) and standard deviation of the distance (σ_d) decrease in a linear fashion. As Fig. 5.4b and c shows, d_{NN} decreases from ~7.2 nm for QDs with one neck to ~6.0 nm for QDs with six necks, while σ_d decreases from 1.1 nm to 0.5 nm (a 55% reduction). Although this simple metric is limited to NNs and neglects the propagation of disorder across longer length scales, [**161**] it demonstrates the importance of neck connectivity to the structural order of QD epi-SLs: high neck number is

associated with high local spatial order. Future tomograms of more perfect monocrystalline samples will be used to map, understand, and ultimately minimize the multiscale spatial disorder of these QD solids.

5.3.3. Charge Transport Simulation. Charge transport in the epi-SL tomography sample was simulated with the HiNTS code. As described in the Methods section, the simulated tomography sample was generated using the QD CoM coordinates and neck network of the experimental tomogram and trimmed into a cuboid shape with electrodes on opposite faces (Fig. 5.5a). In this geometry, electrons must cross the grain boundary between grains I and II, or I and III, to traverse the sample. The tomogram shows that grains I, II, and III are connected by many necks across these grain boundaries. The mobility of the tomography sample was found to be $\sim$4.6 cm^2/Vs (Fig. 5.5d).

To probe the relative importance of the necking versus the conventional SL grain boundaries, and the disorder for the electron transport across the tomography sample, mobility simulations were also performed on the two ensembles of its monocrystalline and bicrystalline analogues. First, we compared the mobility of the tomography sample to that of the ensemble of monocrystalline (single-grain) epi-SLs with the same lattice parameters and neck statistics as grain I (Fig. 5.5b). Relative to the monocrystalline samples, the tomography sample has three grains separated by SL grain boundaries, but these grain boundaries are bridged by a large number of inter-QD necks. In spite of these differences, the mobility of the tomography sample remains typical of the mobility distribution of the ensemble of monocrystalline epi-SLs, as shown in the upper panel of Fig. 5.5d. Next, we also calculated the carrier mobilities of the ensemble of bicrystalline (double-grain) epi-SLs, generated by removing a bisecting plane of necks from the monocrystalline samples (Fig. 5.5c). Electrons can move across this "necking grain boundary" only by hopping, which is significantly slower than direct tunneling through necks. We find that the computed average mobility decreases by $\sim$25% as a consequence of splitting the neck network in two (lower panel of Fig. 5.5d). The introduction of the necking grain boundary makes the mobility of the tomography sample largely inconsistent with the bicrystalline mobility distribution.

The most natural explanation of these results is that the mobility in these strongly disordered epi-SLs is primarily determined by transport across the inter-QD neck network, while SL grain

boundaries impact the mobility only to a limited degree as long as inter-QD necks continue to connect the SL grains across the SL grain boundary with a reasonable density. The tomography sample falls into this category: this explains why its mobity is consistent with the mobility distribution of the monocrystalline samples. In contrast, when a sample is bisected with a neck grain boundary, so that the two grains cease to be connected by inter-QD necks, electrons are forced to thermally hop across no-neck boundaries rather than tunnel through necks, thereby reducing the mobility by a substantial amount. Our analysis suggests that the formation of necks between QDs across conventional SL grain boundaries is an efficient way to substantially increase carrier transport across those grain boundaries. Strategies to enhance the mobility in SLs were already discussed in earlier works, wherein the importance of reducing the disorder of SLs to form mini-bands was emphasized. [**21**] A key message of the present chapter is that the mobility of QD SLs can also be substantially improved by forming sample-spanning neck networks. In a single-grain sample, charge transport should be improved by regulating intra-grain necking conditions such as decreasing neck size dispersity and increasing connectivity. This is particularly true for QD SL based photovoltaics, where the charge carriers are collected along the through-plane (film normal) direction of the multilayer instead of in-plane direction. We did observe a higher through-plane connectivity of QDs in Grain I that might suggest anisotropic necking conditions in a 3D epi-SL film. However, further investigations should be conducted to look into the effect of the degree of anisotropy of connectivity on the mobility, and will more rely on structural statistics from single-grain tomography samples, which is beyond the scope of this chapter.

5.4. Conclusion

We analyzed a full-tilt electron tomographic reconstruction of a disc-shaped region of a 3D epitaxially-connected PbSe QD SL film. This tomogram provides (i) sufficiently high spatial resolution (0.65 nm) to accurately determine the position and size/shape of the QDs and their necks and (ii) sufficiently large volume (4.3×10^5 nm^3) to enable meaningful statistical analysis of structural disorder in the sample. We showed that the sample consists of three SL grains and assigned the unit cell and in-plane crystallographic orientation of each grain as well as the structure of the three grain boundaries. Maps of the neck locations and diameters revealed that the sample has an

average of 3.7 necks per QD (overall network connectivity of 72%) and an average neck diameter of 4.1 nm (64% of the QD diameter). In testing correlations between neck number, neck diameter, inter-QD distance, and QD location in the film, we discovered a strong association between neck number and both the average and standard deviation of the nearest neighbor QD distance, demonstrating that QDs with more necks tend to have more ordered local environments. Achieving more complete, uniform necking will require fabrication of more perfect oleate-capped SLs and greater control of the kinetics of the phase transition from the oleate-capped SL to the epi-SL.

We also simulated the combined nearest-neighbor hopping/tunneling transport in this SL film. Simulations of monocrystalline and bicrystalline analogues showed that SL grain boundaries have limited impact on the electron mobility as long as the grains remain interconnected by necked QDs that form percolating neck networks. An encouraging message of this result is that high mobilities can still be achieved in QD SLs even if they have a high density of grain boundaries, and thus small grain sizes, by increasing the QD attachment density, or neck connectivity, across the SL grain boundaries. To complete the picture, it is natural to expect that once the neck networks connect most of the QDs of the epi-SL to the point that carriers delocalize into mini-bands, further mobility enhancements can be achieved by reducing the density of conventional SL grain boundaries as well.

Our study sets a baseline for the quantitative structural characterization of 3D QD epi-SLs. Looking forward, electron tomography will likely be an important tool for elucidating processing/structure/property relationships and guiding the fabrication of increasingly perfect 3D epi-SLs. Higher-quality epi-SLs will in turn encourage more in-depth analysis of the tomograms, particularly with regard to disorder across length scales longer than those emphasized in this chapter. [**161**] Finally, we note that improving the tomogram resolution by a factor of two would allow visualization of QD facets and atomic-scale defects such as edge dislocations, [**186**] thereby providing a comprehensive near-atomistic picture of the 3D structure of these mesoscale QD films.

CHAPTER 6

SolDeg: Solar Degradation in Silicon Heterojunctions

6.1. Introduction

6.1.1. Solar Cell Degradation. Heterojunction (HJ) Si solar cells have world record efficiencies approaching 27%, due to the excellent surface passivation by their amorphous Silicon (a-Si) layer that leads to low surface recombination velocities and high open circuit voltages V_{OC}. In spite of the impressive efficiency records, HJ Si cells have not yet been widely adopted by the market because of the perceived challenge that HJ cells may exhibit accelerated performance degradation, possibly related to their a-Si layer. Traditional crystalline Si (c-Si) modules typically exhibit about a 0.5%/yr efficiency degradation, primarily via their short circuit current I_{sc} and the fill factor FF, typically attributed to external factors, such as moisture ingress and increased contact resistance. In contrast, in 2018 two papers reported studies of the degradation of fielded Si HJ modules over 5-10 years [**27**, **28**]. They reported degradation rates close to 1%/yr, about twice the rate of traditional cells. These papers pointed to a new degradation channel, the decay of V_{OC}, at a rate of about 0.5%/yr. The decay of V_{OC} suggests that the degradation is possibly due to internal factors, increasing recombination either at the a-Si/c-Si interface, or in the a-Si layer. Such increased recombination is typically caused by the increase of the electronic defect density.

These initial reports on fielded panels were followed up by in-laboratory analysis. The Bertoni group has studied the surface recombination velocity (SRV) at the a-Si/c-Si interface in HJ stacks. By applying a model for the recombination at the a-Si/c-Si interface to their temperature- and injection-dependent SRV data, they analyzed the degradation of the carrier lifetime and were able to attribute it to a loss of chemical passivation [**29**]. More recently, Holovsky et al. investigated ultrathin layers of hydrogenated amorphous silicon (a-Si:H), passivating the surface of crystalline silicon (c-Si) [**30**]. These authors applied highly sensitive attenuated total reflectance Fourier-transform infrared spectroscopy, combined with carrier lifetime measurements. They manipulated

the a-Si/c-Si interface by applying different surface, annealing, and aging treatments. Electronic interface properties were discussed from the perspective of hydrogen mono-layer passivation of the c-Si surface and from the perspective of a-Si:H bulk properties. They concluded that both models have severe limitations and called for a better physical model of the interface [**30**].

Understanding the degradation of the passivated c-Si surface is important not only for understanding a-Si/c-Si heterojunction solar cells. The PV industry roadmap shows that among newly installed modules, the fraction of advanced Passivated Emitter/Rear Contact (PERC) modules will rapidly rise above 50% in the next 3 years. One of the advanced features of these PERC cells is the improved interface passivation with the application of elevated levels of hydrogen. However, the increased efficiency was accompanied by notable levels of degradation [**31**, **32**, **33**]. By experiments and by including all three charge states of hydrogen in their modeling, the authors speculated that the PERC cell degradation both in the dark and under illumination could be explained by the migration of and interaction between hydrogen ions in different charge states.

To summarize, the accelerated degradation of V_{OC} slows the market acceptance of the world-efficiency-record holder HJ Si modules, and impacts the introduction of the advanced PERC cells, thereby impacting the entire PV industry roadmap. Therefore, analyzing and mitigating this degradation process is of crucial importance.

6.1.2. Defects in Amorphous Si. Photoinduced degradation of a-Si under prolonged exposure to intense light was first studied, measured and modeled by Staebler and Wronski [**34**]. They reported that the degradation is characterized by a remarkably universal $t^{1/3}$ power-law temporal growth of the defect density. This behavior has become known as the Staebler-Wronski effect (SWE).

The SWE was analyzed by different methods. Some groups performed electron spin resonance (ESR) measurement on a-Si (a-Si:H) to experimentally detect the increase of the density of dangling bonds induced by light exposure [**35**, **36**, **37**]. Some of these papers also developed a phenomenological model to predict the SW defect-increase as a function of exposure time and light intensity. Other groups used the photocurrent method (PCM) to detect the change of defect density of a-Si under light exposure. In agreement with ESR experiments, PCM also revealed the increase of defect density under light exposure. While the ESR and PCM defect density measurements yielded

analogous results, it is recalled here that they capture different type of defect states [**38**, **39**]. ESR detects all neutral defect states that only include dangling bonds (DBs), while PCM detects both neutral and charged defect states that include DBs and other types of defect states. Therefore PCM measurements revealed that the origin of defect states might be a result of different type of general structural disorders beyond DBs. [**40**, **41**]

Recently, Wronski argued that three distinct defect states, A/B/C, are needed to account for all the data, instead of the standard single "midgap dangling bond" defect [**42**]. The A/B states are efficient electron recombination centers, while the C states recombine holes efficiently. Wronski speculated that these states are differentiated by their different structures: dangling bonds, mono- and divacancies, as also advocated by Smets. Other groups also analyzed their data in terms of three distinct states [**29**,**32**]. However, they focused on the alternative picture that the defect states may be the three charge states H+, H0, and H- of hydrogen. In addition to these experimental works, recent theoretical and computational papers also analyzed the defect states in a-Si, and they concluded that besides dangling bonds, highly strained bonds also contribute to midgap states significantly [**43**, **44**].

To summarize, while a fair amount of progress has been achieved in characterizing defect generation in a-Si, its underlying mechanism and connection to the different types of structural disorder and defects is far from being settled and understood. The problem is still open to question. For this reason, in this chapter we analyze the above problem of defect generation in a-Si/c-Si heterojunction solar cells, with a possible relevance for PERC cell passivation.

6.2. Methods and Results

6.2.1. The SolDeg Platform. To address the above-described *Sol*ar cell *Deg*radation, we have developed the SolDeg platform to model electronic defect generation in a-Si/c-Si heterojunctions, which consists of the following hierarchical stages. (1) Creating a-Si/c-Si stacks. (2) Generating shocked clusters as likely hosts of electronic defects. (3) Identifying shocked clusters that actually host electronic defects. (4) Determining the energy barriers that control the generation of

these electronic defects; and determining their distribution. (5) Determining the temporal evolution of the defect density from the energy barrier distribution. This SolDeg platform is described next in detail.

6.2.2. Creating the Amorphous/Crystalline Si Stacks: Machine-Learning Driven Molecular Dynamics. The SolDeg platform starts with creating a-Si/c-Si heterojunction structures, or stacks. We first created pure a-Si structures, which were carefully optimized in order to match lab-grown a-Si as closely as possible. Second, we placed these optimized a-Si structures on top of slabs of c-Si, and then annealed the interface region. This approach was chosen in order to create the most realistic a-Si atomic structures possible, while still yielding a reasonable aSi/cSi interface region. The details of this approach are as follows.

To create pure amorphous Si structures, one performs melt-quench molecular dynamics (MD) simulations. In a melt-quench MD simulation, a crystalline Si structure is heated past its melting point to generate liquid Si, which is then quenched down to low temperatures at an appropriate rate. This method is widely used for generating amorphous Si networks. It is known that the choice of the interatomic potential used for these MD simulations has a substantial effect on the results. Classical parametric interatomic potentials, such as the Tersoff [**187**] and Stillinger-Weber (SW) [**188**] potentials, have a limited number of parameters/descriptors, and are typically fitted against experimental structural data under a specific set of conditions such as a particular material composition and temperature range. As such, their accuracy in reproducing a wider variety of structural properties of the specific material, or in simulating different temperature ranges or material structures than they were fitted to, often limits the precision of the results.

For example, the excess energy (energy compared to diamond-type Si) of the a-Si resulting from melt-quench simulations performed with these interatomic potentials is typically > 0.20 eV/atom, falling outside of the lab-grown a-Si excess energy range of $0.07 - 0.15$ eV/atom [**189**, **190**, **191**]. The defect densities, e.g. the density of dangling and floating bonds, also differ from typical lab-grown a-Si data. MD simulations with these interatomic potentials are also unable to reach DFT-level accuracy in determining elastic constants and defect formation energies. For all the above reasons, the MD-created a-Si systems need to be further optimized by Density Functional Theory

(DFT) [**44**]. However, the need to use DFT slows down the computational time substantially, and thus limits the accessible system sizes substantially.

To improve the accuracy of our MD simulations in all aspects compared to using these standard interatomic potentials, we instead adopted a Machine-Learning driven general-purpose interatomic potential which has been created for Si [**192**]. This machine-learning driven approach uses the framework of the Gaussian approximation potential (GAP) with a smooth overlap of atomic positions (SOAP) kernel, and has been specifically developed so that GAP-based MD simulations yield DFT-level accuracy, even though they are 10x more efficient, thus enabling the faster simulation of larger systems [**193**, **194**]. Hereafter, we will refer to this potential simply as the Si GAP. It has been shown that the Si GAP captures more than a dozen experimentally measured quantities significantly better than any of the other available interatomic potentials [**192**]. We show below that adopting the Si GAP for our MD simulations yield superior a-Si structures after only a minimum level of DFT optimization. Now we proceed with the technical simulation details.

We generated the a-Si/c-Si stacks by MD simulations, carried out using the LAMMPS software package [**195**]. The simulation time step was 1 fs. Our melt-quench simulations started with crystalline Si cubic supercells containing 216 Si atoms, with three dimensional (3D) periodic boundary conditions. The lattice constant a_0 was chosen to be 5.43 Å, and the dimensions of the supercell $a = b = c = 3a_0$. This lattice constant was chosen to ensure that the mass density of the resulting a-Si structures was 1-3% lower than the mass density of corresponding c-Si structures, consistent with the mass density measured by experiments on a-Si/c-Si stacks.

The crystalline Si was first heated to 1800K to yield liquid Si. The liquid Si was subsequently re-solidified by cooling down to 1500K at a rate of 10^{13} K/s before being equilibrated at 1500K for 100 ps. This solid Si was quenched further down to 500K at a rate of 10^{12} K/s, following previous studies [**192**, **196**, **197**, **198**]. The first quench was performed in the constant-volume and variable-pressure (NVT) ensemble, while the second quench was performed in the variable-volume and constant-pressure (NPT) ensemble with fixed x and y cell-dimensions (to match the dimensions of the c-Si unit cell in the later steps), both using a Nosé-Hoover thermostat and barostat. We minimized the structural energy using a GAP-driven Hessian-free truncated Newton (HFTN) algorithm to relax all atomic positions into their local minima.

These relaxed a-Si structures were further optimized with DFT, specifically making use of the Quantum Espresso 6.2.1 software package [**199**, **200**]. We used the Broyden-Fletcher-Goldfarb-Shanno (BFGS) quasi-newton algorithm, based on the trust radius procedure, as the optimization algorithm.

The Perdew-Burke-Ernzerhof (PBE) exchange-correlation functional [**201**] was used in both the ionic relaxation and the electronic structure calculations using periodic boundary conditions. The core and valence electron interactions were described by the Norm-Conserving Pseudopotential function. Unless otherwise stated, an energy cutoff of 12 Ry was employed for the plane-wave basis set and a 2×2×2 k-point mesh was used with the Monkhorst-Pack grid method for the Brillouin-zone sampling in all the calculations. Methfessel-Paxton smearing [**202**] of width 0.05 Ry was applied to determine the band occupations and electronic density of states.

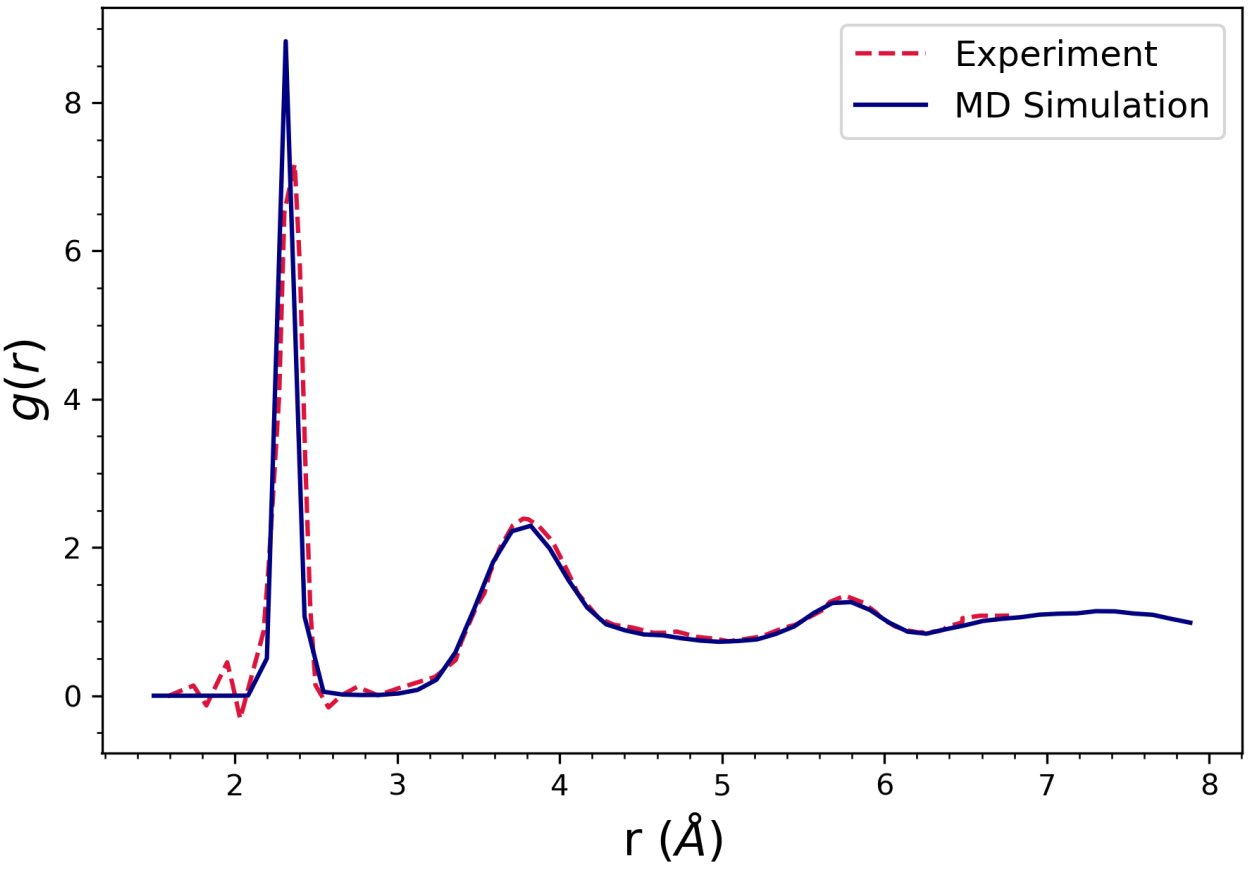

FIGURE 6.1. Radial distribution function $g(r)$ characterizing a typical melt-quench MD a-Si structure, plotted against the experimental values of ref. **203**

Motivated by Pedersen et al., we use the excess energy, the bond angle distribution, and the radial distribution function (RDF), as the most compelling criteria to validate our generated a-Si structures against a-Si experiments [**204**]. In our structures the typical excess energies were around $0.13-0.14\,\text{eV/atom}$, well within the experimentally acceptable range of $0.07-0.15$ eV/atom. These remarkably low excess energies strongly validate the superiority of the Si GAP over traditional potentials, which yield excess energies above 0.20 eV/atom. The bond-angle distribution was centered at 109.1° with a width of $\pm 10.5^\circ$. These values are also consistent with typical experimental values [**205**]. The average Si-Si bond length was $2.38\,\text{Å} \pm .04\,\text{Å}$. Assuming a Si-Si bond-length cutoff of $2.58\,\text{Å}$, slightly less than 10% longer than the average bond-length, the average number of dangling bonds in each supercell was 2.2, and the average number of floating bonds was 0.8. Dangling (floating) bonds are missing (extra) bonds of a Si atom relative to the standard number of 4. Finally, the structures were further validated by calculating the radial distribution function (RDF). The RDF measures the probability of finding the center of an atom at a given distance from the center of another atom as a function of their radial separation. For a-Si, the typical RDF exhibits a strong peak centered at $2.3\,\text{Å}$, and two weak peaks centered around $3.8\,\text{Å}$ and $5.4\,\text{Å}$ (the next-nearest and next-next-nearest neighbor distances in c-Si). As shown in Fig. 1, the RDFs calculated from our GAP-MD generated structures track the experimental data compellingly.

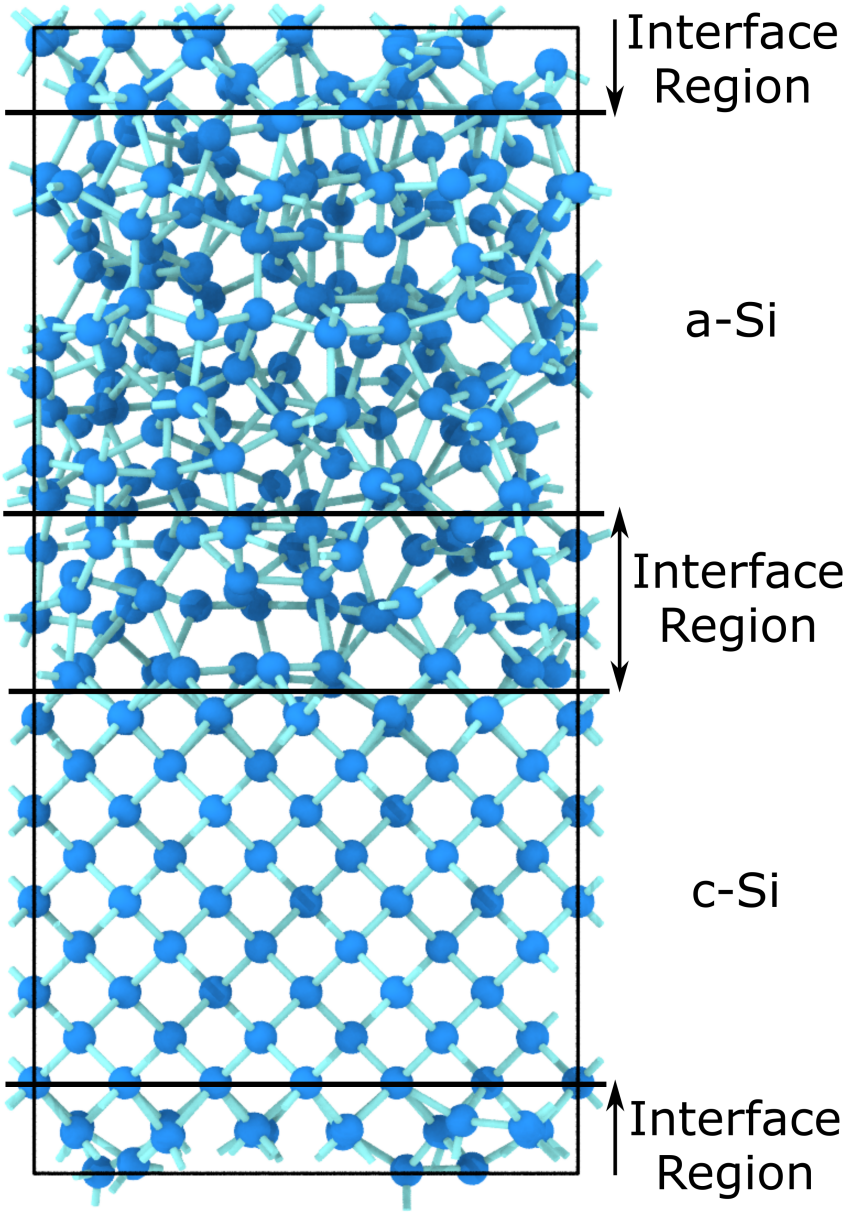

FIGURE 6.2. Rendering of a simulated Si-heterojunction structure. Periodic boundary conditions result in the presence of two distinct interface regions.

We created the Si-heterojunction structures by placing the DFT-optimized a-Si on top of c-Si slabs (of the same dimensions and number of atoms as the a-Si structures). See Fig. 6.2. Note that requiring periodic boundary conditions for the a-Si/c-Si stacks forces two a-Si/c-Si interfaces into the structure, as shown. At both interfaces, the a-Si was placed 1.36 Å ($a_0/4$) away from the edge

of the c-Si slab. This distance was chosen by calculating the total energy of a series of structures where this distance was systematically varied, and choosing the distance which yielded the lowest total energy.

The resulting a-Si/c-Si interfaces are highly strained. For this reason, we relax each interface via thermal annealing. To avoid altering the structure of the carefully optimized a-Si layers, we only annealed a strip of width a_0 centered symmetrically at each a-Si/c-Si interface. The annealing was performed at 450K for 25 ps, and was followed by cooling down to 270K at a rate of 10^{13} K/s. Both steps were performed in the NVT ensemble with a timestep of 1 fs. In total, we created 50 a-Si/c-Si structures.

6.2.3. Defect Generation: Shocked Cluster Generation by the Cluster Blaster. Our overarching theory is that the HJ cell performance degradation is driven by the generation of electronic defects that act as recombination centers. We further posit that most of the electronic defects are generated by a small group of Si atoms in the a-Si transitioning from their moderately disordered cluster into a highly disordered cluster by thermal activation over an energy barrier. The transition into this highly disordered cluster can strain or break the Si bonds, thereby creating electronic defects, such as strained or dangling bonds.

We decided to create highly disordered, "shocked" clusters by heating the cluster very quickly to excessive temperatures, followed by a comparably quick cooling: a procedure we refer to as the "cluster blaster". Using LAMMPS [**195**] and the ML-based Silicon Gaussian Approximation Potential (GAP) [**192**], described in the previous section, we blasted clusters of 5 atoms in our a-Si/c-Si stack, centered at the crystalline/amorphous interface to a temperature of $T = 5000$K while keeping the rest of the structure frozen. We chose $T = 5000$K, because we found that temperatures significantly below this value were not efficient at generating electronic defects in our systems, to be described below. We allowed the shocked clusters to evolve at this elevated temperature for 20 ns so that they could explore their configuration space extensively. After 20 ns, the shocked clusters were quenched quickly, so that they could not escape whichever highly disordered metastable configuration they were nearest to. We then performed a Hessian-free truncated Newton optimization of the quenched shocked clusters, again using the Si GAP. This cluster blaster process was repeated

at the interfaces of all of our 50 a-Si/c-Si stacks at about 30 different locations each, eventually creating about 1,500 shocked clusters with the cluster blaster.

6.2.4. Defect Generation: Analysis of the Shocked Clusters for Electronic Defects. The cluster blaster does not always induce electronic defects in the shocked clusters. To identify which cluster blasting induced electronic defects as well, the next stage of SolDeg is to measure the orbital localization of the electronic states in the a-Si/c-Si stacks with shocked clusters.

We determined the localization of the Kohn-Sham electronic orbitals in the a-Si/c-Si structures before and after the cluster blasting by using the inverse participation ratio (IPR) method. The IPR for an eigenstate Ψ_n is given as:

$$IPR_n = \frac{\Sigma_{i=1}^{I} a_{ni}^4}{(\Sigma_{i=1}^{I} a_{ni}^2)^2} \tag{6.1}$$

where a_{ni} is the coefficient of i^{th} basis set orbital in n^{th} Kohn-Sham orbital Ψ_n ($\Psi_n = \Sigma_{i=1}^{I} a_{ni}\phi_i$) and I is the total number of basis set orbitals used in the DFT calculation. The higher the IPR, the higher the degree of localization. The IPR for a state extended equally over all atoms is close to zero (O(1/N)), and for a state completely localized state on only one atom is one.

Fig. 6.3(a) shows the IPRs, calculated for all Kohn-Sham orbitals obtained by DFT as a function of their energy for a typical a-Si/c-Si stack. Visibly, the majority of the electronic states are localized in the energy region of 5.5-7 eV, lying between the conduction band and the valence band. This region can be identified as a mobility gap because the electronic states are localized within. In contrast, the majority of the states are delocalized inside the conduction and valence bands. It is recalled that the mobility gap often differs somewhat from the density of states (DOS) gap, since the electronic states in the tails of the conduction and valence bands can be localized, separated from the delocalized continuum of band states by a "mobility edge".

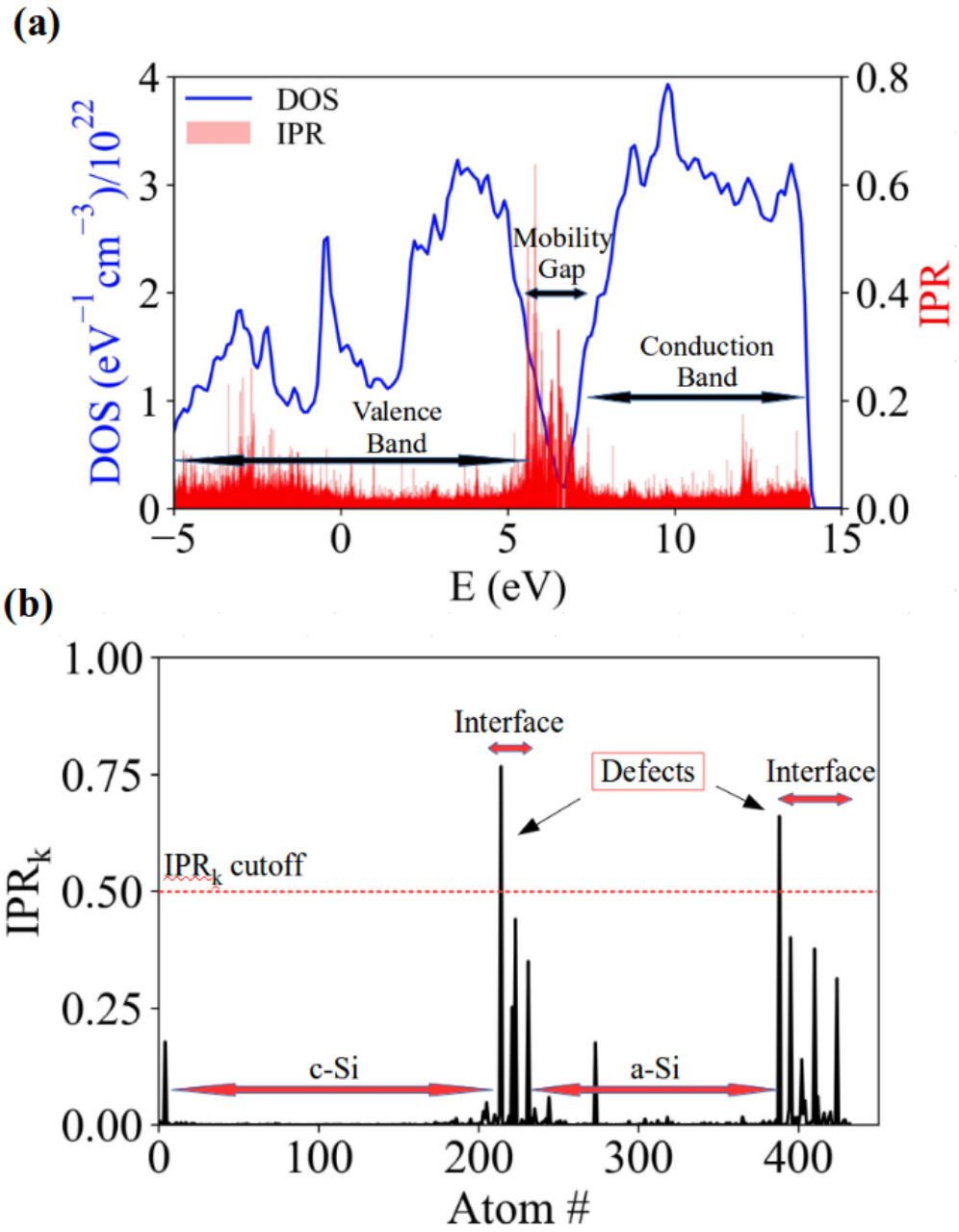

FIGURE 6.3. (a) IPR and (b) IPR_k of typical a-Si/c-Si structures.

In order to determine the localization of the electronic orbitals more we rearrange Eq. 6.1 as follows:

$$IPR(\Psi_n) = \frac{\Sigma_{k=1}^{K}\Sigma_{j=1}^{J} a_{nkj}^4}{(\Sigma_{k=1}^{K}\Sigma_{j=1}^{J} a_{nkj}^2)^2} \tag{6.2}$$

where a_{nkj} is the coefficient of j^{th} atomic orbital belonging to the k^{th} atom in the n^{th} Kohn-Sham orbital. J is the total number of atomic orbitals used in DFT calculations, which belong only to the k^{th} atom in the supercell, and K is the total number of atoms inside the supercell. We introduced the concept of Eq. 6.2 because it is capable of identifying not only that an electronic state is localized, but the location of the atom where it is localized as well by defining a quantity IPR_{nkj} as follows: [**44**]

$$IPR_{nkj} = \frac{a_{nkj}^4}{(\Sigma_{k=1}^{K}\Sigma_{j=1}^{J} a_{nkj}^2)^2} \tag{6.3}$$

Here IPR_{nkj} is the contribution of the k^{th} atom through its j^{th} atomic orbital in the localization of the n^{th} Khon-Sham orbital. One notes that the denominator of Eq. 6.3 is the same for the all IPR_{nkj} for a given n. Thus, the number of IPR_{nkj} values for a given k atom for each Kohn-Sham orbital is J. Denoting the number of Kohn-Sham orbitals as N, each atom in the supercell has NJ IPR_{nkj} values. In order to assign only one IPR value to each atom k, we choose the maximal IPR_{nkj} from among the NJ IPR_{nkj} values for a fixed k. We name this maximal value IPR_k:

$$IPR_k = MAX_{n,j}^{k}\{IPR_{nkj}\} \tag{6.4}$$

Fig. 6.3(b) shows IPR_k for a typical a-Si/c-Si structure, as a function of the atom number k, approximately translating into the z-coordinate of the atoms. As expected, almost all of the localized states are located at the interfaces. There are no localized states in the c-Si, and only one localized state in the a-Si. This localized state distribution is reasonable given the high degree of strain at the interface, in contrast to the low strain in the a-Si, and minimal strain in the c-Si. We identify electronic states as genuine electronic defects as long as they are mostly localized on

a single atom, This is captured by their IPR_k value exceeding a threshold which we take as 0.5. With this threshold convention, visibly there is only one defect at each interface in Fig. 6.3(b).

Once the IPR calculations have been completed, we can determine whether electronic defects have been successfully created in the shocked clusters by the cluster blaster. As somewhat of a surprise, we found that quite often the cluster blasting in fact did the opposite: it annealed out an already existing electronic defect instead of creating one. Therefore, we broadened the scope of our search to identify pairs of initial and final states of the cluster blasting in which the number of electronic defects differed by precisely one. This protocol picked up both the creation and the annihilation of electronic defects in the shocked clusters. We chose to only track initial-final state pairs that differed by a single defect to avoid the need of tracking defect-defect interactions that may affect our results.

6.2.5. Determining Energy Barriers and Their Distribution with the Nudged Elastic Band Method. In the next stage of SolDeg, we determined the energy barriers that control the creation and annihilation of the identified electronic defects because thermal activation across these barriers controls the temporal increase of the overall electronic defect density in a-Si/c-Si stacks, aged in the dark. We will return to light-induced defect generation in future work.

Once pairs of initial and final states have been identified where a single electronic defect was either created or annihilated, we employed the nudged elastic band (NEB) method [**206**, **207**, **208**, **209**] to determine the energy barrier heights between these initial and final states. The nudged elastic band method connects two different local energy minima with several intermediate replica states, each connected to its nearest state neighbor with a "spring" that is nudged perpendicular to the path through state space to allow the "band" to find a saddle point. The NEB method is a standard tool for determining minimum energy paths between states in some fields, but to our knowledge, the NEB method has not been used in the solar field yet, so we will describe the method in some detail here.

NEB starts with an initial guess of a sequence of intermediate "replica" states between an initial and a final state. NEB then postulates an abstract "spring" between the adjacent replica states, to generate a tendency for sequence of replica states to evolve towards a compact, possibly lower energy path between the initial and final state.

The NEB method uses two force components to cause the replica sequence to evolve toward the sought-after minimum energy path (MEP). One of these, the longitudinal component of spring force that connects adjacent replica states is given by:

$$F_i^S = [k(\mathbf{R_{i+1}} - \mathbf{R_i}) - k(\mathbf{R_i} - \mathbf{R_{i-1}})] \cdot \hat{\tau}\hat{\tau} \tag{6.5}$$

where $\mathbf{R_i}$ represents the position of the i^{th} replica in the energy landscape, k is the spring constant, and $\hat{\tau}$ is the "longitudinal" unit vector, parallel with the "spring" at replica i.

The other, lateral force component is perpendicular to the "spring", exerted by the gradient of the energy surface. As such, this force component nudges the spring towards the MEP. In our SolDeg platform, the energy surface was computed with the Si GAP.

$$F_i^V = -\nabla V(\mathbf{R_i}) + \nabla V(\mathbf{R_i}) \cdot \hat{\tau}\hat{\tau} \tag{6.6}$$

where V is the potential energy landscape. The advantage of the NEB method over a standard elastic band method is that artifacts involved with the band cutting corners off the MEP are not a problem for the NEB method.

Our NEB simulations were performed in LAMMPS using the Si GAP [**192**]. We used 32 replicas for each simulation. In our simulations we kept the non-heated atoms fixed: only the heated atoms were allowed to move replica-by-replica. The energy stopping tolerance was 10^{-6} (unitless), and the force stopping tolerance was 10^{-6} eV/Å. The simulation timestep was 10 fs. We used the *fire* minimization algorithm, a damped dynamics method with a variable time step [**210**].

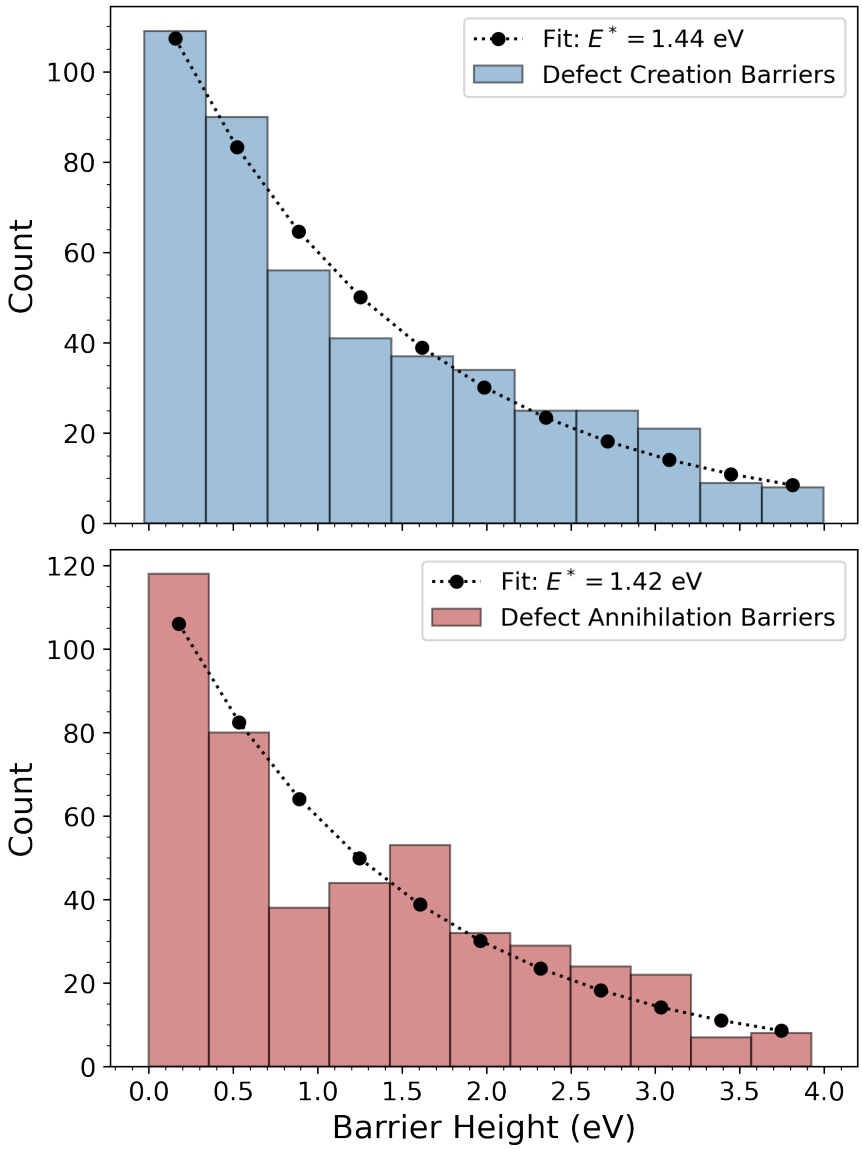

FIGURE 6.4. Energy barrier distributions for: (a) defect creation; and (b) defect annihilation. Black symbols and lines: exponential fit with: $P(E) = (1/E^*)\exp(-E/E^*)$

The results of our NEB calculation are shown in Fig. 6.4. The distribution of the barriers for the defect creation processes is shown in panel (a), while the distribution of the barriers for defect annihilation processes (a reverse transition across the defect creation barrier) is shown in panel (b). Because of the similarity of the two distributions, both the creation and the annihilation processes will impact the time evolution of the defect density. Importantly, Fig. 6.4 reveals an extremely

broad distribution of barriers, from meV to 4 eV. Such an extremely broad barrier distribution is the hallmark of glassy phenomena, and is the driving force behind the defect density growing not only on microscopic time scales but also on the time scale of years.

6.2.6. Determining the Temporal Evolution of the Defect Density N(t) From the Barrier Distribution. In the last stage of the SolDeg platform, we determined the temporal evolution of the defect density from microscopic times scales to 20 years, the standard length of solar cell performance guarantees.

In order to determine the defect density as a function of time, we turned to kinetic Monte Carlo methods. We begun by creating samples with 20,000 individual two-state "clusters" that each could transition from a non-defected state to a defected state by overcoming a defect creation energy barrier, and transition from a defected state to a non-defected state by overcoming a defect annihilation energy barrier. For each cluster transition, the energies for these creation and annihilation processes were drawn from the two barrier distributions determined in the previous section. We eliminated artificial fluctuations induced by the discrete binning of the barriers by representing the distributions with their smooth fitted forms, as shown in Fig. 6.4. The clusters transition over the barriers by thermal activation, with an associated rate of

$$\Gamma = \Gamma_0 e^{\frac{-E}{kT}}, \tag{6.7}$$

where Γ_0 is a characteristic attempt frequency of the cluster to overcome its energy barrier, taken here to be 10^{10} s^{-1}. These rates are calculated for each cluster and summed to determine the "total rate", Γ_{tot}. Next, an event is randomly selected from the possible pool of events, with the probability of selecting event i being equal to $P(i) = \frac{\Gamma_i}{\Gamma_{tot}}$. The time is then moved forward according to $\Delta t = \frac{-ln(r)}{\Gamma_{tot}}$, where r is a random number. This is equivalent to sampling a Poisson waiting time distribution.

The above described method becomes computationally prohibitive when the phenomena of interest are rare events, with rates of occurrence that are several orders of magnitude smaller than typical events. Not only are these rare events exceptionally unlikely to be chosen by the KMC algorithm, but the number of simulation steps needed to evolve the simulation time far enough

to see the rare events will be impossibly large. Using our base kinetic Monte Carlo algorithm, without any acceleration efforts, a million simulation steps only evolve the simulation time by one-hundredth of a second. This is completely inadequate to determine degradation that occurs on the scales of months or years.

Our solution to this problem was to implement the "accelerated super-basin kinetic Monte Carlo" (AS-KMC) algorithm [**211**]. The AS-KMC method adds the extra algorithmic step of checking whether any of the events that are part of a "super-basin" have been executed a pre-specified number of times. For such events, the AS-KMC increases the barrier height, thereby lowering their rate of occurrence. In conventional terms, a super-basin consists of clusters which are linked to each other by high-frequency events but are separated from the surrounding energy landscape by one or more high barriers, making the frequency of the escape from the basin dramatically lower. AS-KMC avoids getting stuck in a single super basin by boosting the probability of the system overcoming these high barriers. In our implementation, as the clusters are independent from each other, a superbasin is the set of fast transitions over the low energy sector of the barrier distribution for each cluster. The AS-KMC method increasing the barrier height in the low energy sector can be thought of as integrating out the fast degrees of freedoms in a renormalization group sense, thereby mapping the problem to a scaled problem where the slower transitions over the higher energy barriers are the typical processes. The formalism of our implementation of the AS-KMC method is as follows. Every N times that an event occurs, the transition rate Γ of that event is reduced by a factor α, such that $\Gamma' = \Gamma/\alpha$. Here α is taken as:

$$\alpha = 1 + (\mathrm{N}\,\delta)/|\ln(\delta)|. \tag{6.8}$$

where δ is the magnitude of the relative error in the new probability of escaping the superbasin once the internal activation barrier has been raised. We chose $N = 10$ and $\delta = 0.25$. As is clear from the above description of the KMC method of forwarding the time at each executed transition by the inverse of the executed rate, the scaling of the Γ rates scales the time itself. The integrating out of the fast degrees of freedom and the rescaling of time together map the model to a "slower transitions

only" model. As this integrating out and rescaling is repeated many times over, transitions over all time scales are properly accounted for by this AS-KMC method.

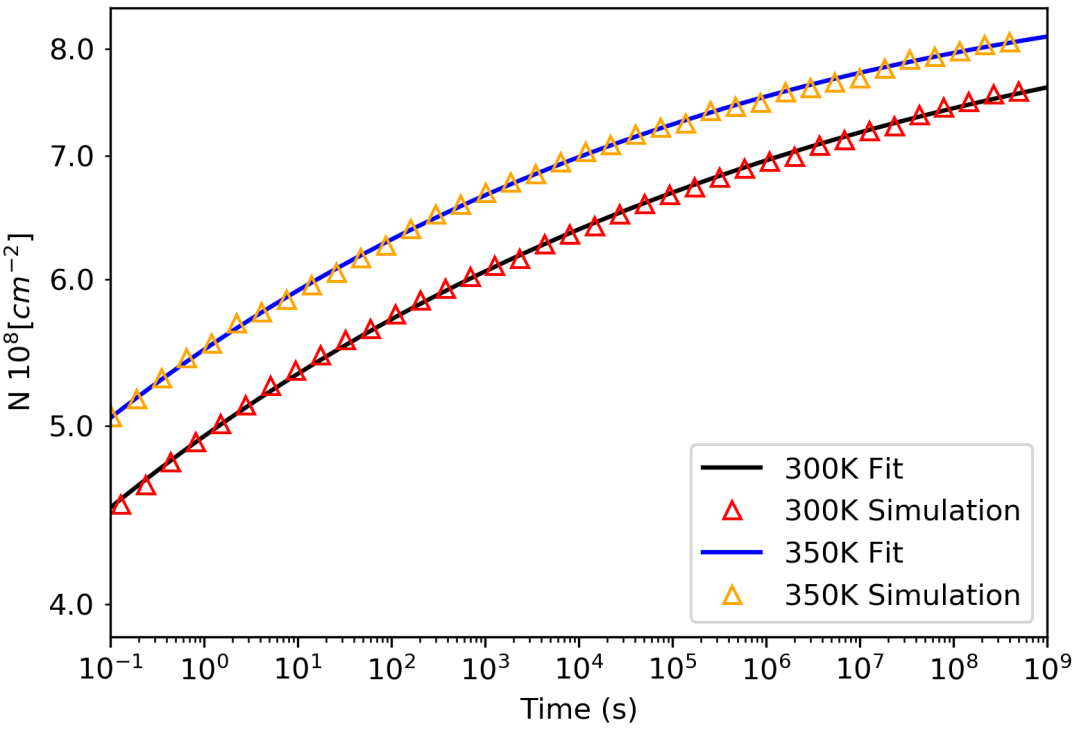

FIGURE 6.5. Defect density N(t) as a function of time. Defect saturation density was chosen as $N_{sat} = 1x10^9$ cm^{-2}. Orange: defect generation by AS-KMC at T=300K. Red: accelerated defect generation by AS-KMC at T=350K. Blue and green: Stretched exponential fits to AS-KMC results with stretching exponent $\beta(300\text{K}) = 0.019$, and $\beta(350\text{K}) = 0.022$.

We reduced the noise by simulating the AS-KMC dynamics for 64 samples of 20,000 clusters each, and finally by averaging the results. Fig. 6.5 shows the time dependent defect density $N(t)$, determined by this method. The minimal fluctuations of $N(t)$ are representative of the effective error bars and thus show that the above approach averaged out the fluctuations very efficiently. The AS-KMC dynamics was performed for samples with temperature at T=300K (red), and T=350K (orange), in order to simulate defect generation at ambient temperatures and with standard accelerated testing protocols at elevated temperatures, as described below in detail.

In order to develop an analytic model and understanding for these simulation results, we recall that systems that exhibit very slow dynamics are often thought of as glassy systems with a broad distribution of energy barriers $P(E)$ [**212**]. In general, the distribution of energy barriers $P(E)$ can be translated into a distribution of "barrier crossing times" $P(\tau)$, and then coupled rate equations can be written down for defect creation and defect annihilation. The expectation value of cluster transition rates at time t can be determined by integrating over the barrier crossing time distribution $P(\tau)$ up to t which turns out to be time dependent instead of the usual constant rates, typical for well defined transition energies. [**213**, **214**] This rate equation for the defect density with time dependent rates can then be solved for $N(t)$.

The specific time dependence of $N(t)$ depends on the functional form of the energy barrier distribution $P(E)$. As seen in Figs. 6.4a-b, our $P(E)$ distributions can be well-fitted with an exponential, $P(E) = (1/E^*)\exp(-E/E^*)$, with $E^* = 1.42$ eV for barrier creation and $E^* = 1.44$ eV for barrier annihilation. Following the above steps for an exponential energy barrier distribution yields a stretched exponential time dependence [**215**, **216**, **217**]:

$$N(t) = N_{sat}\left(1 - \exp\left[-(t/\tau_0)^{\beta}\right]\right), \tag{6.9}$$

where $\beta = k_B T/E^*$, and τ_0 is a short time cutoff. It is important to emphasize that here β was not a fitting parameter. Once we determined E^* from the $P(E)$ we computed earlier (Figs. 6.4a-b), this fixed the value of β. β being fixed makes it all the more remarkable that we were able to fit $N(t, 300\text{K})$ *over ten orders of magnitude* with $\beta(300\text{K}) = 0.019 = k_B * 300\text{K}/E^*$ since $E^* = 1.43$ eV, the average of the defect creation and defect annihilation energy scales; and analogously, fit $N(t, 350\text{K})$ with $\beta(350\text{K}) = 0.022$.

For completeness we note that we obtained very good fits setting τ_0 with $1/\Gamma_0$, but our fits improved by using shorter τ_0 cutoff values. Developing a physical interpretation for the best τ_0 is left for future work. Further, forcing power law or near-flat fits on $P(E)$ predicted power law and logarithmic time dependencies. Such forms can achieve reasonable fits for $N(t)$ over 2-4 orders of magnitude in time, but as the fitting range was extended, the stretched exponential fit produced the singularly best fit, and thus we conclude that the exponential for for $P(E)$ is the natural choice.

A stretched exponential time dependence was reported for the recombination lifetime at a-Si:H/c-Si interfaces [**218**] before. The measurement "annealing" temperature was T=450K, and the β exponent assumed values in the 0.29-0.71 range. Accordingly, the characteristic energy scale E^* of the barrier distribution that controlled this time dependence was in the range of $E^* = 50-125$ meV, an order of magnitude smaller than the Si defect energies that control the time evolution in this chapter. We agree with the conclusion of the authors of Ref. **218**: their time dependence was probably controlled by hydrogen diffusion, not considered in our model.

The main messages of Figs. 6.4a-b and Fig. 6.5 are as follows.

(1) It has been customary to think about degradation processes in Si solar cells as being controlled by chemical bonds with well-defined energies, at most with a narrow distribution. But our simulations of realistic a-Si/c-Si stack interfaces show that the bond energies of a large fraction of the Si atoms, especially those close to the interface, are weakened by stretching and twisting, many to the point of being broken. Therefore, the defect generation is controlled by a broad distribution of energy barriers instead of a narrow one. One is led to the conclusion that the solar cell degradation needs to be described in terms of such wide energy barrier distributions.

(2) We developed the SolDeg platform to answer the above need. SolDeg is capable of connecting the fast atomic motions that control defect structures and play out on the femtosecond time scale, with the slow, glassy transitions controlled by the wide distribution of energy barriers that take place over time scales up to gigaseconds, the order of 20 years. The ability of the SolDeg platform to bridge these 24 orders of magnitude in time makes it a uniquely powerful tool for a comprehensive study of defect generation in a-Si/c-Si stacks.

(3) We have shown that a simple, stretched exponential analytical form can successfully describe defect generation over an unparalleled range of ten orders of magnitude in time. This analytical form may turn out to be quite useful for the analysis of experimental degradation studies.

(4) As far as numerical values are concerned, the defect generation rate in the first month (starting from 10^5 seconds, about one day) is $\approx 1.5\%$/month that slows to 4%/year for the first year. This defect generation rate will be used to connect our theoretical work to experimental data as follows. The published NREL measurements capture degradation of fielded HJ a-Si/c-Si solar

cells in terms of V_{oc}, the open circuit voltage, with the result of 0.5%/year in relative terms [**27**]. The well-known relation connecting V_{oc} to the defect density reads:

$$V_{\mathrm{oc}} = \frac{kT}{q} \ln\left(\frac{J_L}{J_0}\right), \tag{6.10}$$

here J_0 is the dark saturation current, proportional to the defect density $N(t)$, and J_L is the light current. One expects that the primary driver of the performance degradation is the defect density, $N(t)$, thus, we can capture the degradation in natural, relative terms as

$$\frac{1}{V_{\mathrm{oc}}}\frac{dV_{\mathrm{oc}}}{dt} = \frac{-1}{\ln(J_L/J_0)}\frac{1}{N}\frac{dN}{dt}. \tag{6.11}$$

Using relevant values for J_L and J_0 reveals that $ln(\frac{J_L}{J_0})$ is realistically around 20, thus the 4%/year relative defect density growth rate gives a relative degradation rate for V_{oc} of about 0.2%/year. On one hand, it is a reassuring validation of the quantitative reliability of the SolDeg platform that our V_{oc} degradation rate came out to be comparable to the 0.5%/year change observed in fielded HJ modules [**27**]. On the other hand, the fact that our calculated degradation rate is notably lower than the observed value is consistent with the physical expectation that in commercial HJ cells the silicon is hydrogenated, and hydrogen migration is expected to be a primary driver of the defect generation. Further, exposure to illumination also enhances defect generation. The fact that our work has not included hydrogen or illumination yet comfortably accounts for the computed degradation rate being lower than the observed one. Finally, it is noted that while some published experiments report the above steady degradation rate of 0.5%/year over 7 years [**27**], other, shorter time studies report a strongly slowing degradation [**218**]. Our results are consistent with the latter, and thus we think that comparison with experiments should be done in terms of a full time dependence of $N(t)$ or V_{oc}. At any rate, the natural next step for the development of the SolDeg platform is to include hydrogen and illumination. This demanding work is already ongoing and will be reported soon.

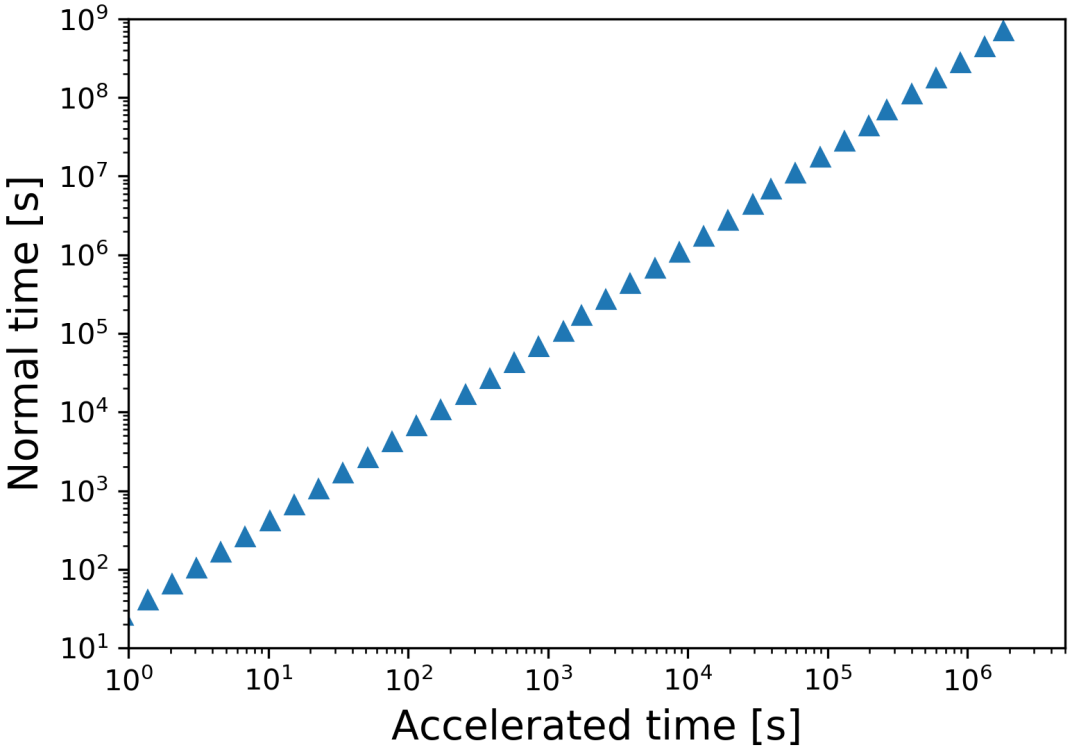

FIGURE 6.6. Time Correspondence Curve, translating accelerated degradation time to degradation time at standard temperature.

(5) The power of SolDeg can be further demonstrated by developing a quantitative guide to calibrate the widely used accelerated testing protocols of solar cells. Fig. 6.5 also shows the accelerated growth of the defect density in a HJ stack at the elevated temperature of T=350K. The two simulations were started with the same defect density at t=0: $N(T$=300K, t=0)=$N(T$=350K, t=0). Visibly, the T=300K and T=350K curves largely track each other: the difference is that $N(T$=350K, $t)$ reaches the same defect densities as $N(T$=300K, $t)$ at shorter times. This is why week-long accelerated testing can capture year-long defect generation under ambient/fielded conditions.

To turn this general observation into a quantitatively useful calibration tool, we created the Time Correspondence Curve (TCC). The TCC connects the times of accelerated testing with those times of normal, ambient degradation that produce the same defect density. In formula:

TCC plots the $t_{\text{accelerated}}$ – t_{normal} pairs for which $N(T{=}350\text{K}, t_{\text{accelerated}}) = N(T{=}300\text{K}, t_{\text{normal}})$. Fig. 6.6 shows the resulting TCC. For example, the TCC shows that $t_{\text{accelerated}}{=}10^6$ seconds of accelerated testing approximately generates the same density of defects as $t_{\text{normal}}{=}10^8$ seconds or normal degradation. In general, the TCC was created by taking horizontal slices across the two curves of Fig. 6.5 to find the corresponding pairs of times that generated the same defect density.

Even a cursory observation reveals that the TCC grows linearly on the log-log plot, i.e. as a power law over an extended, experimentally relevant time period:

$$t_{\text{accelerated}} \propto t_{\text{normal}}^{\nu} \tag{6.12}$$

where $\nu = 0.85 \pm 0.05$, an unexpected scaling relation with an unexpected precision. Just like in Fig. 6.5, this scaling relation is observed over the most remarkable ten orders of magnitude in time. Establishing such simple and practical correspondence relations can be a very helpful product of the SolDeg platform that can be widely used for calibrating accelerated testing protocols. Remarkably, the above-developed description in terms of an exponential $P(E)$ that led to an stretched exponential $N(t)$ that explained the results over ten orders of magnitude, also gives a straightforward explanation for this scaling relation. Direct observation of the stretched exponential formula reveals that $N(T{=}350\text{K}, t_{\text{normal}}^{300/350}) = N(T{=}300\text{K}, t_{\text{normal}})$, i.e. the stretched exponential form not only explains the existence of the scaling form of TCC, but makes a prediction for ν:

$$\nu = T_{\text{normal}}/T_{\text{accelerated}} = 300/350 = 0.85, \tag{6.13}$$

which is exactly the exponent what the direct analysis of the TCC determined. These considerations provide a remarkably self-consistent and powerful tool set to analyze degradation processes.

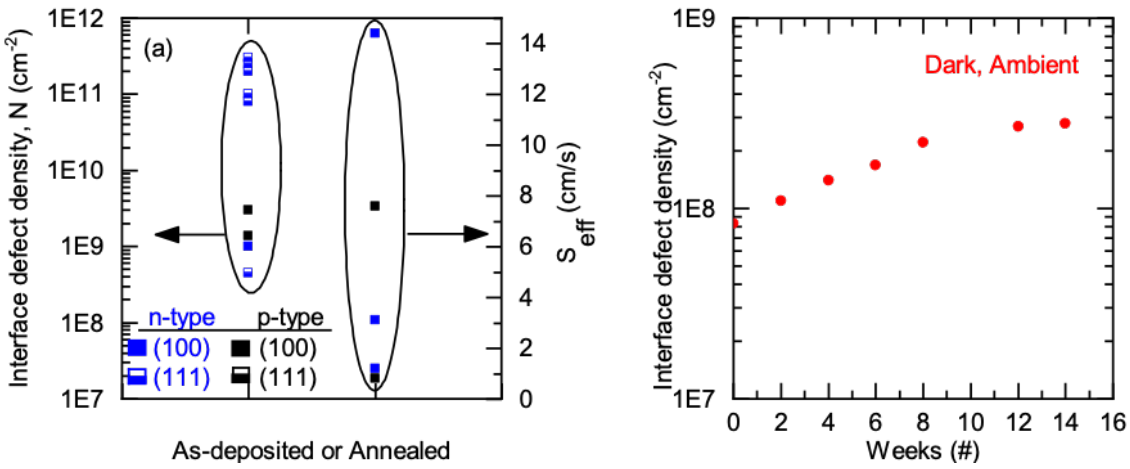

FIGURE 6.7. (a) Interface defect density and effective surface recombination velocity data reported in the literature for a-Si:H/c-Si interface at the time of deposition or after annealing. (b) Interface defect density measured in our a-Si:H/c-Si stacks, stored in the dark under standard ambient condition.

6.3. Experimental Studies of Degradation of a-Si:H/c-Si stacks

In this section, we explore the correspondence between our simulations and experiments on a-Si:H/c-Si heterojunction structures. Fig. 6.7(a) shows that for the interface defect density, a wide range of values have been reported in the literature [**219**, **220**, **221**, **222**]. This unusually wide range is caused by many different factors, such as the different methods and protocols employed for depositing a-Si, the level of cleanliness of c-Si wafer before deposition, substrate morphology, orientation of c-Si, microstructure of the a-Si film, hydrogen content, bonding in a-Si, and storing conditions of samples [**223**, **224**, **225**, **226**]. However, there are not many studies available correlating the impact of such differences to long-term stability of a-Si/c-Si interface. For completeness, in Fig. 6.7(a) we also summarize the corresponding surface recombination velocities (SRV) from the cited papers. Disappointingly, very few of these papers have analyzed the time dependence of the interface defect density and that of the SRV. Therefore, it is difficult to draw lessons from these papers for the long term performance degradation of heterojunction structures.

Driven by these considerations, we have set out to fabricate our own a-Si:H/c-Si heterojunction structures to measure the long time evolution of the defect density and SRV. In order to experimentally isolate the processes associated with the time evolution of interface defect density and

SRV from the processes occurring in other layers, and to be able to access these quantities with direct measurements, we created test structures that were simpler than Si HJ solar cells. This is to isolate the changes happening at the interface and in the film over time from the influence of other layers present in the cell.

These simpler structures, or stacks, were comprised of c-Si of varying thickness (160–260 μm), passivated on both sides with hydrogenated intrinsic a-Si (a-Si:H(i)). We used double-side polished float zone (FZ) quality n-type c-Si wafers with (100) crystal orientation, 2.5 Ωcm resistivity and initial thickness of ∼275 μm. These wafers went through rigorous surface cleaning before deposition of 50 nm of a-Si:H(i) on both sides. Complete details about cleaning protocol and deposition conditions are found in [**227**]. After deposition, these samples were annealed at 280 °C for 30 mins in air in a muffle furnace. Then we measured injection-dependent effective minority carrier lifetime (τ_{eff}) on these samples at temperatures between 30 and 230 °C using the WCT-120TS tool from Sinton Instruments. Data was collected in transient mode due to the long lifetime of the samples. We performed linear fits for $1/\tau_{eff}$ vs $1/W$ data at each injection level to obtain temperature- and injection-dependent SRVs from their slopes. Here W is thickness of the c-Si. As a final step we extracted the interface defect density by fitting the amphoteric defect model proposed by Olibet *et al.* to the SRV *vs* temperature data at different injection levels. The input parameters, along with their best-fit values to the model, were the interface charge density ($Q = -1.3 \times 10^{11}\,\mathrm{cm}^{-2}$), the neutral electron-to-hole capture cross-section ratio ($\frac{\sigma_n^o}{\sigma_p^0} = \frac{1}{20}$), and the charged-to-neutral capture cross-section ratio ($\frac{\sigma_n^+}{\sigma_n^o} = \frac{\sigma_p^-}{\sigma_p^o} = 500$) with $\sigma_p^o = 10^{-16}\,\mathrm{cm}^{-2}$.

The resulting interface defect density values over time for the samples stored in dark and ambient conditions are shown in Fig. 6.7(b). We found that the magnitude of the fitted interface charge density remained the same over time, indicating no change in field effect passivation [**218**]. However, the interface defect density increased with time at the rate of $dN/dt = 5.6 \times 10^7 \mathrm{cm}^{-2}$/month. This translates to a rate of increase of $(1/N)\ dN/dt = 68\%$/month in relative terms for the first 3.5 months. Similar results have been reported previously by Bernardini et al., where the defect density increased from $(6.5 \pm 0.5) \times 10^5 \mathrm{cm}^{-2}$ to $(5.5 \pm 1.5) \times 10^7 \mathrm{cm}^{-2}$ over a period of 28 months for samples stored in dark, ambient conditions [**29**]. This translates to a rate of 17%/month in relative terms. While our study found a higher rate in the initial 3.5 months, we expect the defect generation rate

to slow down considerably as time progresses, and converge to the results of Ref. [**29**]. The fact that the defect generation slows down was clearly established by our simulations as well, as shown in Fig. 6.5, where we found that the rate of change in the early months is about 1.5%/month, slowing to an overall rate of 4%/year for the first year.

We note that the initial defect density in our samples was lower than those reported for as-deposited films in Fig. 6.7(a) by at least an order of magnitude. This could be due to the difference of the deposited a-Si:H film in terms of the crystallinity, hydrogen content, hydrogen bonding configuration and void fraction [**228**]. Whatever the reason may be, the notably low defect density is a compelling indicator for the high quality of our a-Si deposition protocol.

It is noted, of course, that the degradation rate observed in our test structures shown in Fig. 6.7(b) is not expected to directly correspond to the degradation rate observed in complete Si HJ cells. This is due to the additional layers present in Si HJ cells on top of a-Si:H(i) which may efficiently suppress the migration of hydrogen away from the a-Si:H/c-Si interface, as well as prevent oxidation of the a-Si:H(i) layer.

6.4. Conclusions

In this chapter we reported the development of the SolDeg platform for the study of heterojunction solar cell degradation. SolDeg layers several techniques on top of each other, in order to determine the dynamics of electronic defect generation on very long time scales. The first layer of SolDeg was to adapt LAMMPS Molecular Dynamics simulations to create a-Si/c-Si stacks. Our simulations used femtosecond time-steps. For the interatomic potential, we used the machine-learning-based Gaussian approximation potential (GAP). Next, we optimized these stacks with density functional theory calculations. In SolDeg's next layer we created about 1,500 shocked clusters in the stacks by cluster blasting. We then analyzed the just-generated shocked clusters by the inverse participation ratio (IPR) method to conclude that cluster blasting generated electronic defects in about 500 of the 1,500 shocked clusters. Next, we adapted the nudged elastic band (NEB) method to determine the energy barriers that control the creation and annihilation of these electronic defects. We performed the NEB method for about 500 shocked clusters on our way to determine the distribution of these energy barriers. A simple exponential form gave a good fit for

$P(E)$. Finally, we developed an accelerated super-basin kinetic Monte Carlo (AS-KMC) approach to determine the time dependence of the electronic defect generation.

Our main conclusions were as follows. (1) The degradation of a-Si/c-Si heterojunction solar cells via defect generation is controlled by a very broad distribution of energy barriers, extending from the scale of meV to 4 eV. (2) We developed the SolDeg platform that can track the microscopic dynamics of defect generation $N(t)$ from femtoseconds to gigaseconds, over 24 orders of magnitude in time. This makes SolDeg a uniquely powerful tool for a comprehensive study of defect generation in a-Si/c-Si stacks and solar cells. (3) We have shown that a simple, stretched exponential analytical form can successfully describe the defect generation $N(t)$ over ten orders of magnitude in time. (4) We found that in relative terms $V_{\rm oc}$ degrades at a rate of 0.2%/year over the first year. It is a reassuring validation of the quantitative reliability of the SolDeg platform that our V_{oc} degradation rate came out to be comparable to the 0.5%/year change observed in fielded HJ modules [**27**]. The difference is most likely attributable to the SolDeg platform not yet including hydrogen and illumination. The project to include both has already started and will be reported in a later publication. (5) Further, we developed the Time Correspondence Curve to calibrate and validate accelerated testing of solar cells. This TCC connects the times of accelerated testing with those times of normal, fielded degradation that produce the same defect density. Intriguingly, we found a compellingly simple scaling relationship between accelerated and normal times $t(\text{accelerated}) \propto t(\text{normal})^{0.85}$, which can be used to calibrate accelerated testing protocols, making it a more quantitative assessment tool. (6) We ourselves also carried out experimental work on defect generation in a-Si/c-Si HJ stacks. We found that the degradation rate was high on the short, initial time scales, but slowed considerably at longer time scales. A possible explanation is that our samples had unusually low initial defect densities, in which case hydrogen diffusion may generate defects more efficiently.

We plan to continue this project by incorporating hydrogen and illumination into the SolDeg platform and determine the dynamics of the defect generation anew. We will validate and calibrate the improved SolDeg platform by a rigorous comparison to our experimental data. Once the driving forces of defect generation and degradation are reliably captured and characterized by the SolDeg platform and by our experiments, we plan to develop strategies to mitigate these degradation processes.

CHAPTER 7

Conclusions and Future Work

7.1. Summary

In chapter 2, we looked at commensuration effects in nanoparticle solids, and introduced one of the primary tools used in this work, the Hierarchical Nanoparticle Transport Simulator (HiNTS). We found that when the number of electrons per nanoparticle is near integer, transport can be greatly hindered. However, in two layer systems, the story becomes more complicated. Whether or not transport is suppressed by the Coulomb blockade. We developed a phase diagram to describe how different parameters, specifically the disorder and the transverse electric field, affect the transport when a full Coulomb blockade is possible. The three competing energy scales (charging energy, the energy difference between layers due to a transverse electric field, and the energy variation in the nanoparticle energy levels due to disorder) make it so that some fillings that are nominally commensurate experience a Coulomb blockade, while others do not. We identified five distinct dynamical phases within our model to describe these phenomena, and how the phases change as a boundary is crossed.

While most of the work was done in the context of a simple, two layer system, where the transverse field and the filling were independent of one another, additional work was done in the context of a FET, in which, the filling is dependent on the transverse field (gate voltage). The description of the phases discovered in the two-layer model were consistent with the results discovered in the case of the FET simulations, the key difference being that rather than having one transverse field associated with two fillings, each filling would have its own associated transverse field.

Understanding how these various parameters affect whether or not Coulomb blockades occur is important because it allows those who would create NP thin films to know which parameter regimes

to stay away from (or tune towards, as the case may be), depending on what kind of transport they want in their system.

In chapter 3, we added two key features to the HiNTS hierarchy. We developed the ability to simulate extended defects within HiNTS itself, as well as a new layer, a classical resistor network on top, to create the Transport in Defected Nanoparticle Solids (TRIDENS) simulator.

We used the underlying HiNTS method to determine mobility distributions for different types of defects (no defects, point defects, twin planes, and grain boundaries). These distributions were fed into random resistor networks of varying sizes to determine how the material behaved on length scales much larger than those that could be accessed with HiNTS alone (millions of nanoparticles, or a square of side length about 15 microns). We found that as we increased the number of defects, there was a transition from a low to high mobility insulator, whose transition followed a multiple parameter finite size scaling theory. We determined the critical exponents for this transition. One limitation of this method is that the defects placed into the resistor networks are uncorrelated, while looking at experimenal nanoparticle solids, the defects are usually quite extended (which means, in the context of our random resistor network, highly correlated), so in order to compare with experiment, there needs to be significant work done to decrease the size of the large scale defects in nanoparticle solids.

In Chapter 4, we introduced the idea that nanoparticle solids could be a realization of Mott-Hubbard physics. Specifically, we came to the MIT from the insulating side using HiNTS and from the metallic side using dynamical mean field theory. While the MIT has, in previous papers, been described using scaling theory and DMFT, this is, to our knowledge, the first time it has been approached from the insulating regime.

We found an interaction driven MIT when the number of electrons was commensurate with the number of nanoparticles, and a disorder driven MIT away from commensuration. We also identified a Mott-localized to disorder-localized transition at commensuration. Our results also led to identifying several strategies for inducing and MIT in real materials.

In chapter 5, we applied HiNTS to data obtained by electron tomography, that is, to a real experimental sample. Further, we implemented non-activated hopping through necks within HiNTS to identify the relative importance of necking and grain boundaries. We found that within our

model, it is likely that the enhanced transport from necking is a larger influence than the negative impact that normal grain boundaries have on transport. As an aside, these ideas have inspired other work not shown in this thesis, specifically, identifying how necked transport leads to an MIT from the metallic side using the transfer matrix method and finite size scaling, to be discussed in the next section.

In chapter 6 we developed a platform for simulating degradation of heterojunction solar cells over long time scales. We used the machine learning potential known as the Gaussian Approximation Potential (GAP) to generate density-functional-theory-accurate amorphous silicon structures and then place them atop crystalline silicon structures, followed by an anneal to create amorphous-crystalline silicon stacks. These stacks were analyzed using an inverse participation ratio (IPR) calculation to identify any electronic defects. Then, we shocked a small region near the interface by subjecting it to a very high temperature. These shocked structures were quickly frozen and minimized, then once again analyzed using IPR to identify any electronic defects.

Once we analyzed all of the initial and post-shock structures, we identified the initial and final states that differed by exactly one defect. These initial-final state pairs represent the creation or annihilation of a defect. We then used the nudged elastic band calculation to determine the minimum energy barriers between these initial and final states, which we interpret as the creation or annihilation energy of a defect. These energies were then fit with exponential distributions for creation and annihilation.

Next, we fed these distributions into an accelerated super basin kinetic Monte Carlo algorithm to determine the long time defect dynamics of a structure with those barrier distributions at two different temperatures, and, notably, in the dark. We determined that the resulting N(t) plot was fit remarkably well over 10 orders of magnitude in time by a stretched exponential function. We also developed the notion of the time correspondence curve, which relates the number of defects generated at accelerated testing temperatures to the number of defects generated at room temperature. We observed that the time correspondence curve was consistent with a power law relating the two times, and were able to match that power law exponent to the analytical result one gets if one assumes that the temperatures follow the stretched exponential function.

7.2. Future Work

7.2.1. Nanoparticles. In the space of nanoparticles, my future work involves identifying the MIT from the metallic side as a function of necking. We plan to use a modified Anderson Hamiltonian.

$$H = \sum_i \epsilon_i |i\rangle \langle i| + \sum_{<ij>} t_{ij} |i\rangle \langle j| \tag{7.1}$$

Where ϵ_i is drawn from a uniform distribution and t_{ij} is randomly chosen to be either t_{high} (necked transport) or t_{low} (non-necked transport) such that $P(t_{high}) + P(t_{low}) = 1$. We plan to choose the width of the on site energy distribution, t_{high}, and t_{low} such that as we increase $P(t_{high})$ from 0 to 1, we guarantee that we start at an insulator and end at a metal, with he goal of identifying the critical behavior of the metal-insulator transition. In order to do this, we will use something known as the transfer matrix method alongside finite size scaling.

The transfer matrix method [**229**] essentially involves taking a single strip (1D) or bar (2D), solving the Hamiltonian within that bar, and propagating the strip or bar into the 2nd or 3rd dimension respectively, a very large number of times, solving the Hamiltonian as you go.

In some more detail, we start with the recursive Schroedinger Equation [**230**]:

$$t^{||}_{n+1,m}\psi_{n+1,m} = (E - \epsilon_{n,m})\psi_{n,m} - t^{\perp}_{n,m+1}\psi_{n,m+1} - t^{\perp}_{n,m}\psi_{n,m-1} - t^{||}_{n,m}\psi_{n-1,m} \tag{7.2}$$

This can be reformulated into the transfer matrix formalism as

$$\begin{bmatrix} \psi_{n+1} \\ \psi_n \end{bmatrix} = \begin{bmatrix} [t^{||}_{n+1}]^{-1}(E - \epsilon_n - H_\perp) & [t^{||}_n]^{-1}t^{||}_m \\ 1 & 0 \end{bmatrix} \begin{bmatrix} \psi_n \\ \psi_{n-1} \end{bmatrix} = T_n \begin{bmatrix} \psi_n \\ \psi_{n-1} \end{bmatrix} \tag{7.3}$$

Where ϵ_n is the diagonal matrix whose entries are the site energies of the sites within the nth bar or strip, $t^{||}_n$ is the diagonal matrix whose entries are the hopping elements that connect strip or bar n with strip or bar n-1, and $H_\perp$ is the hopping Hamiltonian within the nth strip or bar. The resulting matrix, T_n is known as the transfer matrix.

At the end of the day, we are interested in the localization length of electrons within this system. This can be done by calculating the smallest Lyapunov exponent of the system. While in principle, this can be accomplished using something called Oseledec's theorem, discussed in many transfer matrix papers, in practice, due to numerical instability, one must use a different method to calculate the Lyapunov exponents. The method we use is to periodically (every 10 or so strips or bars) orthonormalize the product matrix using QR decomposition.

$$QR = \prod_{n=1}^{L_{QR}} T_n \tag{7.4}$$

Where Q is a matrix with orthogonal columns and R is an upper triangular matrix with positive elements on the diagonal, and L_{QR} is the number of strips or bars between decompositions. The elements of R correspond to the Lyapunov exponents of the system, the relation is:

$$\gamma_{min} \approx \frac{1}{L_{QR}} ln R_{N,N} \tag{7.5}$$

Where $R_{N,N}$ is the smallest eigenvalue (diagonal element of R). In principle, the entire spectrum of Lyapunov exponents can be computed, but our interest lies only in the smallest one. This process is repeated many times, saving the smallest exponent each time, and continued until the standard deviation of the mean reaches a threshold, usually .01%. The exponents are then averaged, and the localization length is then given as

$$\lambda = \frac{1}{\bar{\gamma}_{min}} \tag{7.6}$$

Once we have the transfer matrix, we turn to finite size scaling in order to determine the critical behavior of our system. The idea of finite size scaling is that when the correlation length ξ is comparable to the finite size of the system, then deviations from the infinite system will occur. As we approach criticality, the correlation length of the system diverges, and thus, the finite size of the system becomes the length scale of relevance. The results, derived from renormalization group,

are used here, though the derivation will not be not shown. Following the method of Sandvik [**231**], we write

$$\lambda(p, L) = L^{\frac{\kappa}{\nu}} f(pL^{\frac{1}{\nu}}) \tag{7.7}$$

Where $p = \frac{(P(t_{high}) - P(t_{high})_{crit})}{P(t_{high})_{crit}}$, the distance from criticality in our scaling parameter. The exponent ν determines the divergence of the correlation length, and in this case, κ determines the divergance of our quantity of interest, the localization length. From physical considerations, and confirmed with numerical simulation and fitting, it is found that $\kappa = \nu$ [**229**]. This equation suggests to us, that if we plot the results of our simulation such that $y_L = \lambda/L$ and $x_L = pL^{\frac{1}{\nu}}$, that our data should collapse onto eachother if we choose the right values for both $P(t_{high})_{crit}$ and ν. Since neither is known beforehand, we need to search parameter space in order to find where the curves collapse. In order to do this, we created a loss function that, when minimized, should correspond to a strong curve collapse that can then be checked by eye.

$$\sum_{i}^{N} \sum_{j \neq i}^{N} \sum_{k=1}^{X} E = \frac{(y_{i,j,k} - y_{j,k})^2}{(y_{i,j,k} + y_{j,k})^2} \tag{7.8}$$

Where N is the number of curves, X is the number of X data for curve j, $y_{j,k}$ is the y value corresponding to the kth x value of curve j, and $y_{i,j,k}$ is the value of y corresponding to the linear interpolation of $y_{i,k'}$ and $y_{i,k'+1}$ at the kth x value of curve j, such that the kth x value of curve j lies between the k'th and (k'+1)th x values of curve i.

Using the transfer matrix method alongside this method of finite size scaling has allowed us to determine the critical exponent in the case of purely diagonal disorder (only having disorder in ϵ), and our methods give values consistent with the literature. We are working on determining the exponents for the modified Anderson Hamiltonian described at the beginning of this section.

7.2.2. HIT Cells. In the space of HIT cells, my future work involves doing work similar to what was done in our initial foray into the SolDeg platform, but this time, including hydrogen. At the time of writing of the SolDeg paper, there did not exist a strong interatomic potential

for simulating Silicon and Hydrogen together in molecular dynamics. Inaccurate potentials for simulating them together did exist, but they were not widely accepted by the community, and their range of accuracy is not enough for our needs. Since then, Davis Unruh and Reza Vatan, alongside Gabor Csanyi, developed a silicon hydrogen GAP for use in a subsequent SolDeg paper. This new potential is much more accurate than previous silicon hydrogen interatomic potentials and will allow us to repeat a slightly modified SolDeg process on hydrogenated crystalline-amorphous silicon heterojunction stacks in order to find out how hydrogenation affects the degradation rate.

Bibliography

[1] Steve Byrnes. ShockleyQueisserBreakdown. publisher: Wikipedia.

[2] A. J. Nozik. Quantum dot solar cells. *Physica E: Low-dimensional Systems and Nanostructures*, 14(1-2):115–120, 2002.

[3] Prashant V. Kamat. Quantum dot solar cells. semiconductor nanocrystals as light harvesters†. *J. Phys. Chem. C*, 112(48):18737–18753, 2008.

[4] William Shockley and Hans J. Queisser. Detailed balance limit of efficiency of p-n junction solar cells. *Journal of Applied Physics*, 32(3):510–519, 1961.

[5] Lazaro A. Padilha, John T. Stewart, Richard L. Sandberg, Wan Ki Bae, Weon-Kyu Koh, Jeffrey M. Pietryga, and Victor I. Klimov. Carrier multiplication in semiconductor nanocrystals: Influence of size, shape, and composition. *Accounts of Chemical Research*, 46(6):1261–1269, 2013. PMID: 23530867.

[6] Y. Okada, N. J. Ekins-Daukes, T. Kita, R. Tamaki, M. Yoshida, A. Pusch, O. Hess, C. C. Phillips, D. J. Farrell, K. Yoshida, N. Ahsan, Y. Shoji, T. Sogabe, and J.-F. Guillemoles. Intermediate band solar cells: Recent progress and future directions. *Applied Physics Reviews*, 2(2):021302, 2015.

[7] Yasuhiro Shirasaki, Geoffrey J Supran, Moungi G Bawendi, and Vladimir Bulović. Emergence of colloidal quantum-dot light-emitting technologies. *Nature Photonics*, 7(1):13–23, 2013.

[8] Dmitri V. Talapin and Christopher B. Murray. PbSe nanocrystal solids for n- and p-channel thin film field-effect transistors. *Science*, 310(5745):86–89, 2005.

[9] Frederik Hetsch, Ni Zhao, Stephen V. Kershaw, and Andrey L. Rogach. Quantum dot field effect transistors. *Materials Today*, 16(9):312–325, September 2013.

[10] Ruili Wang, Yuequn Shang, Pongsakorn Kanjanaboos, Wenjia Zhou, Zhijun Ning, and Edward H Sargent. Colloidal quantum dot ligand engineering for high performance solar cells. *Energy & Environmental Science*, 9(4):1130–1143, 2016.

[11] Jaeyoung Jang, Wenyong Liu, Jae Sung Son, and Dmitri V. Talapin. Temperature-dependent hall and field-effect mobility in strongly coupled all-inorganic nanocrystal arrays. *Nano Letters*, 14(2):653–662, February 2014.

[12] Jong-Soo Lee, Maksym V. Kovalenko, Jing Huang, Dae Sung Chung, and Dmitri V. Talapin. Band-like transport, high electron mobility and high photoconductivity in all-inorganic nanocrystal arrays. *Nature Nanotechnology*, 6(6):348–352, June 2011.

[13] Chia-Hao M Chuang, Patrick R Brown, Vladimir Bulović, and Moungi G Bawendi. Improved performance and stability in quantum dot solar cells through band alignment engineering. *Nature materials*, 13(8):796, 2014.

[14] Daniel M Kroupa, Márton Vörös, Nicholas P Brawand, Brett W McNichols, Elisa M Miller, Jing Gu, Arthur J Nozik, Alan Sellinger, Giulia Galli, and Matthew C Beard. Tuning colloidal quantum dot band edge positions through solution-phase surface chemistry modification. *Nature communications*, 8:15257, 2017.

[15] Ting Chen, KV Reich, Nicolaas J Kramer, Han Fu, Uwe R Kortshagen, and BI Shklovskii. Metal-insulator transition in films of doped semiconductor nanocrystals. *Nature materials*, 15(3):299–303, 2016.

[16] Ji-Hyuk Choi, Aaron T. Fafarman, Soong Ju Oh, Dong-Kyun Ko, David K. Kim, Benjamin T. Diroll, Shin Muramoto, J. Greg Gillen, Christopher B. Murray, and Cherie R. Kagan. Bandlike transport in strongly coupled and doped quantum dot solids: A route to high-performance thin-film electronics. *Nano Letters*, 12(5):2631–2638, May 2012.

[17] Elise Talgorn, Yunan Gao, Michiel Aerts, Lucas T Kunneman, Juleon M Schins, TJ Savenije, Marijn A van Huis, Herre SJ van der Zant, Arjan J Houtepen, and Laurens DA Siebbeles. Unity quantum yield of photogenerated charges and band-like transport in quantum-dot solids. *Nature nanotechnology*, 6(11):733–739, 2011.

[18] Matteo Cargnello, Aaron C Johnston-Peck, Benjamin T Diroll, Eric Wong, Bianca Datta, Divij Damodhar, Vicky VT Doan-Nguyen, Andrew A Herzing, Cherie R Kagan, and Christopher B Murray. Substitutional doping in nanocrystal superlattices. *Nature*, 524(7566):450–453, 2015.

[19] Benjamin H. Savitzky, Robert Hovden, Kevin Whitham, Jun Yang, Frank Wise, Tobias Hanrath, and Lena F. Kourkoutis. Propagation of structural disorder in epitaxially connected quantum dot solids from atomic to micron scale. *Nano Letters*, 16(9):5714–5718, 2016. PMID: 27540863.

[20] Kevin Whitham, Jun Yang, Benjamin H Savitzky, Lena F Kourkoutis, Frank Wise, and Tobias Hanrath. Charge transport and localization in atomically coherent quantum dot solids. *Nature materials*, 15(5):557–563, 2016.

[21] Yao Liu, Jason Tolentino, Markelle Gibbs, Rachelle Ihly, Craig L Perkins, Yu Liu, Nathan Crawford, John C Hemminger, and Matt Law. PbSe quantum dot field-effect transistors with air-stable electron mobilities above 7 cm2 v–1 s–1. *Nano letters*, 13(4):1578–1587, 2013.

[22] David J Norris, Alexander L Efros, and Steven C Erwin. Doped nanocrystals. *Science*, 319(5871):1776–1779, 2008.

[23] Moon Sung Kang, Ayaskanta Sahu, C Daniel Frisbie, and David J Norris. Influence of silver doping on electron transport in thin films of PbSe nanocrystals. *Advanced Materials*, 25(5):725–731, 2013.

[24] Ayaskanta Sahu, Moon Sung Kang, Alexander Kompch, Christian Notthoff, Andrew W Wills, Donna Deng, Markus Winterer, C Daniel Frisbie, and David J Norris. Electronic impurity doping in CdSe nanocrystals. *Nano letters*, 12(5):2587–2594, 2012.

[25] David Mocatta, Guy Cohen, Jonathan Schattner, Oded Millo, Eran Rabani, and Uri Banin. Heavily doped semiconductor nanocrystal quantum dots. *Science*, 332(6025):77–81, 2011.

[26] Tem5psu. English: Schematic cross-section of a HIT solar cell. HIT stands for "Heterojunction with Intrinsic Thin layer"., March 2015.

[27] Chris Deline, Steve Johnston, Steve R. Rummel, Bill Sekulic, Dirk C Jordan, Steve R Rummel, Peter Hacke, Sarah R Kurtz, Kristopher O Davis, Eric John Schneller, Xingshu Sun, Muhammad A Alam, and Ronald A Sinton. Silicon heterojunction system field performance. *IEEE Journal of Photovoltaics*, 8(1):177–182, 2018.

[28] T. Ishii, S. Choi, R. Sato, Y. Chiba, and A. Masuda. Annual degradation rates of recent c-Si pv modules under subtropical coastal climate conditions. In *2018 IEEE 7th World Conference on Photovoltaic Energy Conversion (WCPEC) (A Joint Conference of 45th IEEE PVSC, 28th PVSEC 34th EU PVSEC)*, pages 705–708, 2018.

[29] Simone Bernardini and Mariana I. Bertoni. Insights into the degradation of amorphous silicon passivation layer for heterojunction solar cells. *Phys. Status Solidi A*, 216(4):1800705, 2019.

[30] Silvia Martin De Nicolas, Stefaan De Wolf, Christophe Ballif, Jakub Holovský, and Silvia Martín De Nicolás. Amorphous/crystalline silicon interface stability: Correlation between infrared spectroscopy and electronic passivation properties. *Adv. Mater. Interfaces*, 7(20):2000957, 2020.

[31] Phillip Hamer, Moonyong Kim, Catherine Chan, Alison Ciesla Nee Wenham, Daniel Chen, Alison Ciesla nee Wenham, Fiacre Rougieux, Yuchao Zhang, Malcolm Abbott, and Brett Hallam. Hydrogen-induced degradation: Explaining the mechanism behind light- and elevated temperature-induced degradation in n- and p-type silicon. *Sol. Energy Mater. Sol. Cells*, 207:110353, 2020.

[32] Hongbo Tong, Haitao Zhu, Chao Ding, Hua Li, Ran Chen, Daniel Chen, Brett Hallam, Chee Mun Chong, Stuart Wenham, and Alison Ciesla. 23.83% efficient mono-perc incorporating advanced hydrogenation. *Prog. Photovolt.*, 28(12):1239–1247, 2020.

[33] Phillip G. Hamer, Moonyong Kim, Tsun H. Fung, Gabrielle Bourret-Sicotte, Daniel Chen, Phillip G Hamer, Tsun H Fung, Shaoyang Liu, Catherine E Chan, Alison Ciesla, Ran Chen, Malcolm D Abbott, Brett J Hallam, and Stuart R Wenham. Hydrogen induced degradation: A possible mechanism for light- and elevated temperature- induced degradation in n-type silicon. *Sol. Energy Mater. Sol. Cells*, 185:174–182, 2018.

[34] D. L. Staebler and C. R. Wronski. Reversible conductivity changes in discharge-produced amorphous si. *Appl. Phys. Lett.*, 31(4):292–294, 1977.

[35] H. Dersch, J. Stuke, and J. Beichler. Light-induced dangling bonds in hydrogenated amorphous silicon. *Appl. Phys. Lett.*, 38(6):456–458, 1981.

[36] M. Stutzmann, W. B. Jackson, and C. C. Tsai. Light-induced metastable defects in hydrogenated amorphous silicon: A systematic study. *Phys. Rev. B*, 32:23–47, Jul 1985.

[37] J. Melskens, A. Schnegg, A. Baldansuren, K. Lips, M. P. Plokker, S. W. H. Eijt, H. Schut, M. Fischer, M. Zeman, and A. H. M. Smets. Structural and electrical properties of metastable defects in hydrogenated amorphous silicon. *Phys. Rev. B*, 91:245207, Jun 2015.

[38] Tatsuo Shimizu, Masaki Shimada, Hidekazu Sugiyama, and Minoru Kumeda. Relation between electron-spin-resonance and constant-photocurrent-method defect densities in hydrogenated amorphous silicon. *Jpn. J. Appl. Phys.*, 40(Part 1, No. 1):54–58, jan 2001.

[39] Tatsuo Shimizu, Masaki Shimada, and Minoru Kumeda. Comparative study of defect densities evaluated by electron spin resonance and constant photocurrent method in undoped and n-doped hydrogenated amorphous silicon. *Jpn. J. Appl. Phys.*, 41(Part 1, No. 5A):2829–2833, may 2002.

[40] T. Gotoh, S. Nonomura, M. Nishio, S. Nitta, M. Kondo, and A. Matsuda. Experimental evidence of photoinduced expansion in hydrogenated amorphous silicon using bending detected optical lever method. *Appl. Phys. Lett.*, 72(23):2978–2980, 1998.

[41] Kousaku Shimizu, Tsuguhiro Shiba, Takashi Tabuchi, and Hiroaki Okamoto. Reversible photo-induced structural change in hydrogenated amorphous silicon. *Jpn. J. Appl. Phys.*, 36(Part 1, No. 1A):29–32, jan 1997.

[42] Xinwei Niu and Christopher R Wronski. The limited relevance of swe dangling bonds to degradation in high-quality a-si:H solar cells. *IEEE J. Photovolt.*, 4(3):778–784, 2014.

[43] P. A. Khomyakov, Wanda Andreoni, N. D. Afify, and Alessandro Curioni. Large-scale simulations of *a*-si:H: The origin of midgap states revisited. *Phys. Rev. Lett.*, 107:255502, Dec 2011.

[44] Reza V. Meidanshahi, Stuart Bowden, and Stephen M. Goodnick. Electronic structure and localized states in amorphous Si and hydrogenated amorphous Si. *Phys. Chem. Chem. Phys.*, 21:13248–13257, 2019.

[45] Howard M. Branz. Hydrogen collision model: Quantitative description of metastability in amorphous silicon. *Phys. Rev. B*, 59:5498–5512, Feb 1999.

[46] Dmitri V. Talapin, Jong-Soo Lee, Maksym V. Kovalenko, and Elena V. Shevchenko. Prospects of colloidal nanocrystals for electronic and optoelectronic applications. *Chemical Reviews*, 110(1):389–458, January 2010.

[47] Maksym V. Kovalenko, Liberato Manna, Andreu Cabot, Zeger Hens, Dmitri V. Talapin, Cherie R. Kagan, Victor I. Klimov, Andrey L. Rogach, Peter Reiss, Delia J. Milliron, Philippe Guyot-Sionnnest, Gerasimos Konstantatos, Wolfgang J. Parak, Taeghwan Hyeon, Brian A. Korgel, Christopher B. Murray, and Wolfgang Heiss. Prospects of nanoscience with nanocrystals. *ACS Nano*, 9(2):1012–1057, 2015.

[48] Frederik Hetsch, Ni Zhao, Stephen V Kershaw, and Andrey L Rogach. Quantum dot field effect transistors. *Materials Today*, 16(9):312–325, 2013.

[49] Matt Law Group. Unpublished. *unpublished*, 2018.

[50] KV Reich, Tianran Chen, and BI Shklovskii. Theory of a field-effect transistor based on a semiconductor nanocrystal array. *Physical Review B*, 89(23):235303, 2014.

[51] Arjan J Houtepen and Daniel Vanmaekelbergh. Orbital occupation in electron-charged CdSe quantum-dot solids. *The Journal of Physical Chemistry B*, 109(42):19634–19642, 2005.

[52] Hugo E Romero and Marija Drndic. Coulomb blockade and hopping conduction in PbSe quantum dots. *Physical review letters*, 95(15):156801, 2005.

[53] Effendi Leobandung, Lingjie Guo, Yun Wang, and Stephen Y Chou. Observation of quantum effects and Coulomb blockade in silicon quantum-dot transistors at temperatures over 100 k. *Applied Physics Letters*, 67(7):938–940, 1995.

[54] KV Reich, M Schecter, and BI Shklovskii. Accumulation, inversion, and depletion layers in SrTiO3. *Physical Review B*, 91(11):115303, 2015.

[55] Moon Sung Kang, Ayaskanta Sahu, David J. Norris, and C. Daniel Frisbie. Size- and temperature-dependent charge transport in PbSe nanocrystal thin films. *Nano Letters*, 11(9):3887–3892, 2011.

[56] K. B. Efetov and A. Tschersich. Coulomb effects in granular materials at not very low temperatures. *Phys. Rev. B*, 67:174205, 2003.

[57] I. S. Beloborodov, A. V. Lopatin, and V. M. Vinokur. Coulomb effects and hopping transport in granular metals. *Phys. Rev. B*, 72:125121, 2005.

[58] I. S. Beloborodov, A. V. Lopatin, V. M. Vinokur, and K. B. Efetov. Granular electronic systems. *Rev. Mod. Phys.*, 79:469–518, 2007.

[59] I. Carbone, S. A. Carter, and G. T. Zimanyi. Monte carlo modeling of transport in PbSe nanocrystal films. *Journal of Applied Physics*, 114(19):193709, November 2013.

[60] Luman Qu, Márton Vörös, and Gergely T. Zimanyi. Metal-insulator transition in nanoparticle solids: Insights from kinetic monte carlo simulations. *Scientific Reports*, 7(1):7071, 2017.

[61] Luman Qu, Márton Vörös, and Gergely T Zimanyi. Unpublished. *submitted*, 2018.

[62] Inuk Kang and Frank W. Wise. Electronic structure and optical properties of PbS and PbSe quantum dots. *Journal of the Optical Society of America B*, 14(7):1632–1646, July 1997.

[63] Lin-Wang Wang and Alex Zunger. Dielectric constants of silicon quantum dots. *Phys. Rev. Lett.*, 73:1039–1042, Aug 1994.

[64] J. M. An, A. Franceschetti, and A. Zunger. Electron and hole addition energies in PbSe quantum dots. *Phys. Rev. B*, 76:045401, Jul 2007.

[65] C. Delerue, M. Lannoo, and G. Allan. Excitonic and quasiparticle gaps in Si nanocrystals. *Phys. Rev. Lett.*, 84:2457–2460, Mar 2000.

[66] Aleksandar Donev, Salvatore Torquato, and Frank H. Stillinger. Neighbor list collision-driven molecular dynamics simulation for nonspherical hard particles. i. algorithmic details. *Journal of Computational Physics*, 202(2):737–764, 2005.

[67] A. B. Bortz, M. H. Kalos, and J. L. Lebowitz. A new algorithm for monte carlo simulation of ising spin systems. *J. Comput. Phys.*, 17:10–18, 1975.

[68] R. A. Marcus. On the theory of oxidation-reduction reactions involving electron transfer. i. *The Journal of Chemical Physics*, 24(5):966–978, May 1956.

[69] R. E. Chandler, A. J. Houtepen, J. Nelson, and D. Vanmaekelbergh. Electron transport in quantum dot solids: Monte carlo simulations of the effects of shell filling, Coulomb repulsions, and site disorder. *Physical Review B*, 75(8):085325, February 2007.

[70] J Stephan, S Schrader, and L Brehmer. Monte carlo simulations of charge transport in molecular solids: a modified Miller Abrahams type jump rate approach. *Synthetic Metals*, 111-112:353–357, June 2000.

[71] Nenad Vukmirović and Lin-Wang Wang. Carrier hopping in disordered semiconducting polymers: How accurate is the Miller–Abrahams model? *Applied Physics Letters*, 97(4):043305, July 2010.

[72] O. Madelung, U. Rössler, and M. Schulz. Lead selenide (pbse) optical properties, dielectric constant. In *Non-Tetrahedrally Bonded Elements and Binary Compounds I*, volume 41C of *Landolt-Börnstein - Group III Condensed Matter*, pages 1–10. Springer Berlin Heidelberg, 1998.

[73] Hadrien Lepage. *Modélisation de solides à nanocristaux de silicium*. PhD thesis, institut national des sciences appliquées de Lyon, 2013.

[74] Jacek Jasieniak, Marco Califano, and Scott E. Watkins. Size-dependent valence and conduction band-edge energies of semiconductor nanocrystals. *ACS Nano*, 5(7):5888–5902, July 2011.

[75] Joshua J. Choi, Yee-Fun Lim, Mitk'El B. Santiago-Berrios, Matthew Oh, Byung-Ryool Hyun, Liangfeng Sun, Adam C. Bartnik, Augusta Goedhart, George G. Malliaras, Héctor D. Abruña, Frank W. Wise, and Tobias Hanrath. PbSe nanocrystal excitonic solar cells. *Nano Letters*, 9(11):3749–3755, Nov 2009.

[76] Yao Liu, Markelle Gibbs, James Puthussery, Steven Gaik, Rachelle Ihly, Hugh W. Hillhouse, and Matt Law. Dependence of carrier mobility on nanocrystal size and ligand length in PbSe nanocrystal solids. *Nano Letters*, 10(5):1960–1969, May 2010.

[77] J. M. An, A. Franceschetti, and A. Zunger. Electron and hole addition energies in PbSe quantum dots. *Physical Review B*, 76(4):045401, July 2007.

[78] William M. Merrill, R.E. Diaz, M.M. LoRe, M.C. Squires, and N.G. Alexopoulos. Effective medium theories for artificial materials composed of multiple sizes of spherical inclusions in a host continuum. *Antennas and Propagation, IEEE Transactions on*, 47(1):142–148, Jan 1999.

[79] Xavier Cartoixà and Lin-Wang Wang. Microscopic dielectric response functions in semiconductor quantum dots. *Phys. Rev. Lett.*, 94:236804, Jun 2005.

[80] David R. Penn. Wave-number-dependent dielectric function of semiconductors. *Phys. Rev.*, 128:2093–2097, Dec 1962.

[81] Ding Pan, Quan Wan, and Giulia Galli. The refractive index and electronic gap of water and ice increase with increasing pressure. *Nature communications*, 5, 2014.

[82] G. Allan and C. Delerue. Confinement effects in PbSe quantum wells and nanocrystals. *Physical Review B*, 70(24):245321, December 2004.

[83] Aleksandar Donev, Salvatore Torquato, and Frank H. Stillinger. Neighbor list collision-driven molecular dynamics simulation for nonspherical hard particles.: Ii. applications to ellipses and ellipsoids. *Journal of Computational Physics*, 202(2):765–793, 2005.

[84] Márton Vörös, Giulia Galli, and Gergely T Zimanyi. Colloidal nanoparticles for intermediate band solar cells. *ACS Nano*, 9(7):6882–6890, 2015.

[85] Soong Ju Oh, Nathaniel E. Berry, Ji-Hyuk Choi, E. Ashley Gaulding, Taejong Paik, Sung-Hoon Hong, Christopher B. Murray, and Cherie R. Kagan. Stoichiometric control of lead chalcogenide nanocrystal solids to enhance their electronic and optoelectronic device performance. *ACS Nano*, 7:2413–2421, 2013.

[86] K. V. Reich, Tianran Chen, and B. I. Shklovskii. Theory of a field-effect transistor based on a semiconductor nanocrystal array. *Phys. Rev. B*, 89:235303, Jun 2014.

[87] Luman Qu, Chase Hansen, Marton Vörös, and Gergely T. Zimanyi. Commensuration effects in layered nanoparticle solids. *Phys. Rev. B*, 101(4), JAN 17 2020.

[88] Eric B. Hostetler, Ki-Joong Kim, Richard P. Oleksak, Robert C. Fitzmorris, Daniel A. Peterson, Padmavathi Chandran, Chih-Hung Chang, Brian K. Paul, David M. Schut, and Gregory S. Herman. Synthesis of colloidal PbSe nanoparticles using a microwave-assisted segmented flow reactor. *Materials Letters*, 128:54–59, 2014.

[89] R. D. Schaller and V. I. Klimov. High efficiency carrier multiplication in pbse nanocrystals: Implications for solar energy conversion. *Phys. Rev. Lett.*, 92:186601, May 2004.

[90] M. Lannoo, C. Delerue, and G. Allan. Screening in semiconductor nanocrystallites and its consequences for porous silicon. *Phys. Rev. Lett.*, 74:3415–3418, Apr 1995.

[91] Philippe Guyot-Sionnest. Electrical transport in colloidal quantum dot films. *J. Phys. Chem. Lett.*, 3(9):1169–1175, 2012.

[92] Yao Liu, Markelle Gibbs, James Puthussery, Steven Gaik, Rachelle Ihly, Hugh W. Hillhouse, and Matt Law. Dependence of carrier mobility on nanocrystal size and ligand length in PbSe nanocrystal solids. *Nano Letters*, 10(5):1960–1969, 2010. PMID: 20405957.

[93] Alex Abelson, Caroline Qian, Trenton Salk, Zhongyue Luan, Kan Fu, Jian-Guo Zheng, Jenna L. Wardini, and Matt Law. Collective topo-epitaxy in the self-assembly of a 3d quantum dot superlattice. *Nature Materials*, 19(1):49+, Jan 2020.

[94] N Sh Izmailian, R Kenna, and F Y Wu. The two-point resistance of a resistor network: a new formulation and application to the cobweb network. *Journal of Physics A: Mathematical and Theoretical*, 47(3):035003, dec 2013.

[95] A. L. Efros and B. I. Shklovskii. Critical behaviour of conductivity and dielectric constant near the metal-nonmetal transition threshold. *Physica Status Solidi (B): Basic Research*, 76(2):475–485, August 1976.

[96] X Lan, O Voznyy, M Liu, J Xu, A Proppe, G Walters, F Fan, H Tan, M Liu, and E Sargent. 10.6% certified colloidal quantum dot solar cells via solvent-polarity-engineered halide passivation. *Nano letters*, 16(7):4630–4634, 2016.

[97] Shuang Jiao, Jun Du, Zhonglin Du, Donghui Long, Wuyou Jiang, Zhengxiao Pan, Yan Li, and Xinhua Zhong. Nitrogen-doped mesoporous carbons as counter electrodes in quantum dot sensitized solar cells with a conversion efficiency exceeding 12%. *J. Phys. Chem. Lett.*, 8(3):559–564, 2017.

[98] Erin M. Sanehira, Ashley R. Marshall, Jeffrey A. Christians, Steven P. Harvey, Peter N. Ciesielski, Lance M. Wheeler, Philip Schulz, Lih Y. Lin, Matthew C. Beard, and Joseph M. Luther. Enhanced mobility $cspbi_3$ quantum dot arrays for record-efficiency, high-voltage photovoltaic cells. *Sci. Adv.*, 3(10), 2017.

[99] Patrick A. Lee and T. V. Ramakrishnan. Disordered electronic systems. *Rev. Mod. Phys.*, 57:287–337, Apr 1985.

[100] A M. Finkel'shtein. Influence of Coulomb interaction on the properties of disordered metals. *Zh. Eksp. Teor. Fiz.*, 84(1):168–189, 1983.

[101] B L. Altshuler, A G. Aronov, and P A. Lee. Interaction effects in disordered fermi systems in 2 dimensions. *Phys. Rev. Lett.*, 44(19):1288–1291, 1980.

[102] C. Castellani, G. Kotliar, and P. A. Lee. Fermi-liquid theory of interacting disordered-systems and the scaling theory of the metal-insulator-transition. *Phys. Rev. Lett.*, 59(3):323–326, JUL 20 1987.

[103] Günter Schmid. *Nanoparticles: From Theory to Application*. John Wiley & Sons, 2006.

[104] Dong Yu, Congjun Wang, Brian L. Wehrenberg, and Philippe Guyot-Sionnest. Variable range hopping conduction in semiconductor nanocrystal solids. *Physical Review Letters*, 92(21):216802, May 2004.

[105] Heng Liu, Alexandre Pourret, and Philippe Guyot-Sionnest. Mott and efros-shklovskii variable range hopping in CdSe quantum dots films. *ACS Nano*, 4(9):5211–5216, September 2010.

[106] A. L. Efros and B. I. Shklovskii. Critical behaviour of conductivity and dielectric constant near the metal-non-metal transition threshold. *physica status solidi (b)*, 76(2):475–485, 1976.

[107] M C O. Aguiar, V. Dobrosavljević, E. Abrahams, and G. Kotliar. Critical behavior at the mott-anderson transition: A typical-medium theory perspective. *Phys. Rev. Lett.*, 102:156402, Apr 2009.

[108] Helena Bragança, M. C. O. Aguiar, J. Vučičević, D. Tanasković, and V. Dobrosavljević. Anderson localization effects near the mott metal-insulator transition. *Phys. Rev. B*, 92:125143, 2015.

[109] Krzysztof Byczuk, Walter Hofstetter, and Dieter Vollhardt. Mott-hubbard transition versus anderson localization in correlated electron systems with disorder. *Phys. Rev. Lett.*, 94:056404, Feb 2005.

[110] Sampaio, K. C. Beverly, and J. R. Heath. Dc transport in self-assembled 2d layers of ag nanoparticles. *The Journal of Physical Chemistry B*, 105(37):8797–8800, 2001.

[111] Tim Byrnes, Na Young Kim, Kenichiro Kusudo, and Yoshihisa Yamamoto. Quantum simulation of fermi-hubbard models in semiconductor quantum-dot arrays. *Phys. Rev. B*, 78:075320, Aug 2008.

[112] C. A. Stafford and S. Das Sarma. Collective Coulomb blockade in an array of quantum dots: A mott-hubbard approach. *Phys. Rev. Lett.*, 72:3590–3593, May 1994.

[113] C. A. Stafford and S. Das Sarma. Collective Coulomb blockade in an array of quantum dots: A mott-hubbard approach. *Phys. Rev. Lett.*, 72:3590–3593, May 1994.

[114] Andrew Shabaev, Alexander L Efros, and Alexei L Efros. Dark and photo-conductivity in ordered array of nanocrystals. *Nano Lett.*, 13(11):5454—5461, 2013.

[115] F. Remacle. On electronic properties of assemblies of quantum nanodots. *J. Phys. Chem. A*, 104(20):4739–4747, 2000.

[116] F. Remacle and R. D. Levine. Electronic response of assemblies of designer atoms: The metal-insulator transition and the role of disorder. *J. Am. Chem. Soc.*, 122(17):4084–4091, 2000.

[117] Christophe Delerue and Michel Lannoo. *Nanostructures: Theory and Modeling*. Springer-Verlag Berlin Heidelberg, 2004.

[118] Cherie R. Kagan and Christopher B. Murray. Charge transport in strongly coupled quantum dot solids. *Nat. Nanotechnol.*, 10:1013—-1026, 2015.

[119] S V Kravchenko and M P Sarachik. Metal–insulator transition in two-dimensional electron systems. *Reports on Progress in Physics*, 67(1):1–44, dec 2003.

[120] C. Castellani, C. Di Castro, and P. A. Lee. Metallic phase and metal-insulator transition in two-dimensional electronic systems. *Phys. Rev. B*, 57:R9381–R9384, Apr 1998.

[121] J M. An, A. Franceschetti, S V. Dudiy, and A. Zunger. The peculiar electronic structure of PbSe quantum dots. *Nano Lett.*, 6(12):2728–2735, 2006.

[122] Marcelo J. Rozenberg. Integer-filling metal-insulator transitions in the degenerate hubbard model. *Phys. Rev. B*, 55:R4855–R4858, Feb 1997.

[123] Antoine Georges, Gabriel Kotliar, Werner Krauth, and Marcelo Rozenberg. *Rev. Mod. Phys.*, 68(1):13–125, 1996.

[124] Emanuel Gull, Andrew J. Millis, Alexander I. Lichtenstein, Alexey N. Rubtsov, Matthias Troyer, and Philipp Werner. *Rev. Mod. Phys.*, 83(2):349–404, 2011.

[125] Kristjan Haule. Quantum monte carlo impurity solver for cluster dynamical mean-field theory and electronic structure calculations with adjustable cluster base. *Phys. Rev. B*, 75:155113, 2007.

[126] Philipp Werner, Emanuel Gull, and Andrew J. Millis. Metal-insulator phase diagram and orbital selectivity in three-orbital models with rotationally invariant hund coupling. *Phys. Rev. B*, 79:115119, Mar 2009.

[127] V. Janis˘ and D. Vollhardt. Coupling of quantum degrees of freedom in strongly interacting disordered electron systems. *Phys. Rev. B*, 46:15712–15715, Dec 1992.

[128] V. Dobrosavljević and G. Kotliar. Strong correlations and disorder in d=∞ and beyond. *Phys. Rev. B*, 50:1430–1449, Jul 1994.

[129] M. Ulmke, V. Janiš, and D. Vollhardt. Anderson-hubbard model in infinite dimensions. *Phys. Rev. B*, 51:10411–10426, Apr 1995.

[130] V. Dobrosavljević and G. Kotliar. Mean field theory of the mott-anderson transition. *Phys. Rev. Lett.*, 78:3943–3946, May 1997.

[131] M. C. O. Aguiar, V. Dobrosavljević, E. Abrahams, and G. Kotliar. Effects of disorder on the non-zero temperature mott transition. *Phys. Rev. B*, 71:205115, May 2005.

[132] Miloš M. Radonjić, D. Tanasković, V. Dobrosavljević, and K. Haule. Influence of disorder on incoherent transport near the mott transition. *Phys. Rev. B*, 81:075118, Feb 2010.

[133] Krzysztof Byczuk, Walter Hofstetter, and Dieter Vollhardt. Anderson localization vs. mott-hubbard metal-insulator transition in disordered, interacting lattice fermion systems. *Int. J. Mod. Phys. B*, 24(12n13):1727–1755, 2010.

[134] Andras G Pattantyus-Abraham, Illan J Kramer, Aaron R Barkhouse, Xihua Wang, Gerasimos Konstantatos, Ratan Debnath, Larissa Levina, Ines Raabe, Mohammad K Nazeeruddin, Michael Gratzel, and Edward Sargent. Depleted-heterojunction colloidal quantum dot solar cells. *ACS Nano*, 4(6):3374–3380, 2010.

[135] Edward H Sargent. Colloidal quantum dot solar cells. *Nat. Photonics*, 6(3):133, 2012.

[136] Graham H Carey, Ahmed L Abdelhady, Zhijun Ning, Susanna M Thon, Osman M Bakr, and Edward H Sargent. Colloidal quantum dot solar cells. *Chem. Rev.*, 115(23):12732–12763, 2015.

[137] Younghoon Kim, Fanglin Che, Jea Woong Jo, Jongmin Choi, F Pelayo García de Arquer, Oleksandr Voznyy, Bin Sun, Junghwan Kim, Min-Jae Choi, Rafael Quintero-Bermudez, et al. A facet-specific quantum dot passivation strategy for colloid management and efficient infrared photovoltaics. *Adv. Mater.*, page 1805580, 2019.

[138] Cherie R Kagan, Efrat Lifshitz, Edward H Sargent, and Dmitri V Talapin. Building devices from colloidal quantum dots. *Science*, 353(6302):aac5523, 2016.

[139] Soong Ju Oh, Zhuqing Wang, Nathaniel E Berry, Ji-Hyuk Choi, Tianshuo Zhao, E Ashley Gaulding, Taejong Paik, Yuming Lai, Christopher B Murray, and Cherie R Kagan. Engineering charge injection and charge transport for high performance PbSe nanocrystal thin film devices and circuits. *Nano Lett.*, 14(11):6210–6216, 2014.

[140] Gerasimos Konstantatos and Edward H Sargent. Colloidal quantum dot photodetectors. *Infrared Phys. Technol.*, 54(3):278–282, 2011.

[141] Matthew M Ackerman, Xin Tang, and Philippe Guyot-Sionnest. Fast and sensitive colloidal quantum dot mid-wave infrared photodetectors. *ACS Nano*, 12(7):7264–7271, 2018.

[142] Cuong Dang, Joonhee Lee, Craig Breen, Jonathan S Steckel, Seth Coe-Sullivan, and Arto Nurmikko. Red, green and blue lasing enabled by single-exciton gain in colloidal quantum dot films. *Nat. Nanotechnol.*, 7(5):335, 2012.

[143] Yujie Chen, Johannes Herrnsdorf, Benoit Guilhabert, Yanfeng Zhang, Ian M Watson, Erdan Gu, Nicolas Laurand, and Martin D Dawson. Colloidal quantum dot random laser. *Opt. Express*, 19(4):2996–3003, 2011.

[144] Yao Liu, Markelle Gibbs, James Puthussery, Steven Gaik, Rachelle Ihly, Hugh W Hillhouse, and Matt Law. Dependence of carrier mobility on nanocrystal size and ligand length in PbSe nanocrystal solids. *Nano Lett.*, 10(5):1960–1969, 2010.

[145] Iwan Moreels, Karel Lambert, Dries Smeets, David De Muynck, Tom Nollet, José C Martins, Frank Vanhaecke, Andre Vantomme, Christophe Delerue, Guy Allan, et al. Size-dependent optical properties of colloidal pbs quantum dots. *ACS Nano*, 3(10):3023–3030, 2009.

[146] Cherie R Kagan and Christopher B Murray. Charge transport in strongly coupled quantum dot solids. *Nat. Nanotechnol.*, 10(12):1013, 2015.

[147] William J Baumgardner, Kevin Whitham, and Tobias Hanrath. Confined-but-connected quantum solids *via* controlled ligand displacement. *Nano Lett.*, 13(7):3225–3231, 2013.

[148] Wiel H Evers, Bart Goris, Sara Bals, Marianna Casavola, Joost De Graaf, Rene Van Roij, Marjolein Dijkstra, and Daniel Vanmaekelbergh. Low-dimensional semiconductor superlattices formed by geometric control over nanocrystal attachment. *Nano Lett.*, 13(6):2317–2323, 2012.

[149] Wiel H Evers, Juleon M Schins, Michiel Aerts, Aditya Kulkarni, Pierre Capiod, Maxime Berthe, Bruno Grandidier, Christophe Delerue, Herre SJ Van Der Zant, Carlo Van Overbeek, et al. High charge mobility in two-dimensional percolative networks of PbSe quantum dots connected by atomic bonds. *Nat. Commun.*, 6:8195, 2015.

[150] CS Suchand Sandeep, Jon Mikel Azpiroz, Wiel H Evers, Simon C Boehme, Iwan Moreels, Sachin Kinge, Laurens DA Siebbeles, Ivan Infante, and Arjan J Houtepen. Epitaxially connected PbSe quantum-dot films: Controlled neck formation and optoelectronic properties. *ACS Nano*, 8(11):11499–11511, 2014.

[151] Mark P Boneschanscher, Wiel H Evers, Jaco J Geuchies, Thomas Altantzis, Bart Goris, Freddy T Rabouw, SAP Van Rossum, Herre SJ van der Zant, Laurent DA Siebbeles, Gustaaf Van Tendeloo, et al. Long-range orientation and atomic attachment of nanocrystals in 2d honeycomb superlattices. *Science*, 344(6190):1377–1380, 2014.

[152] Man Zhao, Fangxu Yang, Chao Liang, Dawei Wang, Defang Ding, Jiawei Lv, Jianqi Zhang, Wenping Hu, Chenguang Lu, and Zhiyong Tang. High hole mobility in long-range ordered 2d lead sulfide nanocrystal monolayer films. *Adv. Funct. Mater.*, 26(28):5182–5188, 2016.

[153] Jaco J Geuchies, Carlo Van Overbeek, Wiel H Evers, Bart Goris, Annick De Backer, Anjan P Gantapara, Freddy T Rabouw, Jan Hilhorst, Joep L Peters, Oleg Konovalov, et al. In situ study of the formation mechanism of two-dimensional superlattices from PbSe nanocrystals. *Nat. Mater.*, 15(12):1248, 2016.

[154] Willem Walravens, Jonathan De Roo, Emile Drijvers, Stephanie Ten Brinck, Eduardo Solano, Jolien Dendooven, Christophe Detavernier, Ivan Infante, and Zeger Hens. Chemically triggered formation of two-dimensional epitaxial quantum dot superlattices. *ACS Nano*, 10(7):6861–6870, 2016.

[155] Man Zhao, Defang Ding, Fangxu Yang, Dawei Wang, Jiawei Lv, Wenping Hu, Chenguang Lu, and Zhiyong Tang. Ligand effects on electronic and optoelectronic properties of two-dimensional pbs necking percolative superlattices. *Nano Res.*, 10(4):1249–1257, 2017.

[156] Benjamin E Treml, Benjamin H Savitzky, Ali M Tirmzi, Jessica Cimada DaSilva, Lena F Kourkoutis, and Tobias Hanrath. Successive ionic layer absorption and reaction for postassembly control over inorganic interdot bonds in long-range ordered nanocrystal films. *ACS Appl. Mater. Interfaces*, 9(15):13500–13507, 2017.

[157] Daniel M Balazs, Bartosz M Matysiak, Jamo Momand, Artem G Shulga, Maria Ibáñez, Maksym V Kovalenko, Bart J Kooi, and Maria Antonietta Loi. Electron mobility of 24 $cm^2v^{-1}s^{-1}$ in PbSe colloidal-quantum-dot superlattices. *Adv. Mater.*, 30(38):1802265, 2018.

[158] Carlo Van Overbeek, Joep L Peters, Susan AP Van Rossum, Marc Smits, Marijn A Van Huis, and Daniel Vanmaekelbergh. Interfacial self-assembly and oriented attachment in the family of pbx (x= s, se, te) nanocrystals. *J. Phys. Chem. C*, 122(23):12464–12473, 2018.

[159] Benjamin T Diroll, Nicholas J Greybush, Cherie R Kagan, and Christopher B Murray. Smectic nanorod superlattices assembled on liquid subphases: Structure, orientation, defects, and optical polarization. *Chem. Mater.*, 27(8):2998–3008, 2015.

[160] Davide Altamura, Vaclav Holý, Dritan Siliqi, Indira Chaitanya Lekshmi, Concetta Nobile, Giuseppe Maruccio, P Davide Cozzoli, Lixin Fan, Fabia Gozzo, and Cinzia Giannini. Exploiting gisaxs for the study of a 3d ordered superlattice of self-assembled colloidal iron oxide nanocrystals. *Cryst. Growth Des.*, 12(11):5505–5512, 2012.

[161] Benjamin H Savitzky, Robert Hovden, Kevin Whitham, Jun Yang, Frank Wise, Tobias Hanrath, and Lena F Kourkoutis. Propagation of structural disorder in epitaxially connected quantum dot solids from atomic to micron scale. *Nano Lett.*, 16(9):5714–5718, 2016.

[162] Alex Abelson, Caroline Qian, Trenton Salk, Zhongyue Luan, Kan Fu, Jian-Guo Zheng, Jenna L Wardini, and Matt Law. Collective topo-epitaxy in the self-assembly of a 3d quantum dot superlattice. *Nat. Mater.*, 19(1):49–55, 2020.

[163] Kevin Whitham and Tobias Hanrath. Formation of epitaxially connected quantum dot solids: Nucleation and coherent phase transition. *J. Phys. Chem. Lett.*, 8(12):2623–2628, 2017.

[164] Heiner Friedrich, Cedric J Gommes, Karin Overgaag, Johannes D Meeldijk, Wiel H Evers, Bart de Nijs, Mark P Boneschanscher, Petra E de Jongh, Arie J Verkleij, Krijn P de Jong, et al. Quantitative structural analysis of binary nanocrystal superlattices by electron tomography. *Nano Lett.*, 9(7):2719–2724, 2009.

[165] Mark P Boneschanscher, Wiel H Evers, Weikai Qi, Johannes D Meeldijk, Marjolein Dijkstra, and Daniel Vanmaekelbergh. Electron tomography resolves a novel crystal structure in a binary nanocrystal superlattice. *Nano Lett.*, 13(3):1312–1316, 2013.

[166] Wiel H Evers, Heiner Friedrich, Laura Filion, Marjolein Dijkstra, and Daniel Vanmaekelbergh. Observation of a ternary nanocrystal superlattice and its structural characterization by electron tomography. *Angew. Chem., Int. Ed.*, 48(51):9655–9657, 2009.

[167] Joep L Peters, Thomas Altantzis, Ivan Lobato, Maryam Alimoradi Jazi, Carlo Van Overbeek, Sara Bals, Daniel Vanmaekelbergh, and Sophia Buhbut Sinai. Mono-and multilayer silicene-type honeycomb lattices by oriented attachment of PbSe nanocrystals: Synthesis, structural characterization, and analysis of the disorder. *Chem. Mater.*, 30(14):4831–4837, 2018.

[168] Benjamin H Savitzky, Kevin Whitham, Kaifu Bian, Robert Hovden, Tobias Hanrath, and Lena F Kourkoutis. Three-dimensional arrangement and connectivity of lead-chalcogenide nanoparticle assemblies for next generation photovoltaics. *Microsc. Microanal.*, 20(S3):542–543, 2014.

[169] Jeannot Trampert and Jean-Jacques Leveque. Simultaneous iterative reconstruction technique: Physical interpretation based on the generalized least squares solution. *J. Geophys. Res.: Solid Earth*, 95(B8):12553–12559, 1990.

[170] Wim van Aarle, Willem Jan Palenstijn, Jan De Beenhouwer, Thomas Altantzis, Sara Bals, K Joost Batenburg, and Jan Sijbers. The astra toolbox: A platform for advanced algorithm development in electron tomography. *Ultramicroscopy*, 157:35–47, 2015.

[171] Chien-Chun Chen, Chun Zhu, Edward R White, Chin-Yi Chiu, MC Scott, BC Regan, Laurence D Marks, Yu Huang, and Jianwei Miao. Three-dimensional imaging of dislocations in a nanoparticle at atomic resolution. *Nature*, 496(7443):74, 2013.

[172] Davis Unruh, Chase Hansen, Alberto Camjanyi, Joel Bobadilla, Marcelo Rozenberg, and Gergely T Zimanyi. Persistent Coulomb blockade across the metal-insulator transition in nanoparticle solids. *arXiv.org, e-Print Arch., Condens. Matter*, 2019.

[173] Inuk Kang and Frank W Wise. Electronic structure and optical properties of pbs and PbSe quantum dots. *J. Opt. Soc. Am. B*, 14(7):1632–1646, 1997.

[174] Christophe Jean Delerue and Michel Lannoo. *Nanostructures: Theory and Modeling*. Springer Science & Business Media, 2013.

[175] Arjan J. Houtepen, Daan Kockmann, and Daniel Vanmaekelbergh. Reappraisal of variable-range hopping in quantum-dot solids. *Nano Lett.*, 8(10):3516–3520, 2008.

[176] Han Fu, K. V. Reich, and B. I. Shklovskii. Hopping conductivity and insulator-metal transition in films of touching semiconductor nanocrystals. *Phys. Rev. B*, 93:125430, Mar 2016.

[177] Angang Dong, Jun Chen, Patrick M Vora, James M Kikkawa, and Christopher B Murray. Binary nanocrystal superlattice membranes self-assembled at the liquid–air interface. *Nature*, 466(7305):474, 2010.

[178] Angang Dong, Yucong Jiao, and Delia J Milliron. Electronically coupled nanocrystal superlattice films by in situ ligand exchange at the liquid–air interface. *ACS Nano*, 7(12):10978–10984, 2013.

[179] Mark C Weidman, Detlef-M Smilgies, and William A Tisdale. Kinetics of the self-assembly of nanocrystal superlattices measured by real-time in situ x-ray scattering. *Nat. Mater.*, 15(7):775, 2016.

[180] Tobias Hanrath, Joshua J Choi, and Detlef-M Smilgies. Structure/processing relationships of highly ordered lead salt nanocrystal superlattices. *ACS Nano*, 3(10):2975–2988, 2009.

[181] Danielle K Smith, Brian Goodfellow, Detlef-M Smilgies, and Brian A Korgel. Self-assembled simple hexagonal ab2 binary nanocrystal superlattices: Sem, gisaxs, and defects. *J. Am. Chem. Soc.*, 131(9):3281–3290, 2009.

[182] Darren Dunphy, Hongyou Fan, Xuefa Li, Jin Wang, and C Jeffrey Brinker. Dynamic investigation of gold nanocrystal assembly using in situ grazing-incidence small-angle x-ray scattering. *Langmuir*, 24(19):10575–10578, 2008.

[183] Arthur RC McCray, Benjamin H Savitzky, Kevin Whitham, Tobias Hanrath, and Lena F Kourkoutis. Orientational disorder in epitaxially connected quantum dot solids. *ACS nano*, 13(10):11460–11468, 2019.

[184] Yu Wang, Xinxing Peng, Alex Abelson, Penghao Xiao, Caroline Qian, Lei Yu, Colin Ophus, Peter Ercius, Lin-Wang Wang, Matt Law, et al. Dynamic deformability of individual PbSe nanocrystals during superlattice phase transitions. *Sci. Adv.*, 5(6):eaaw5623, 2019.

[185] Junfeng Wang, Zongzheng Zhou, Wei Zhang, Timothy M Garoni, and Youjin Deng. Bond and site percolation in three dimensions. *Phys. Rev. E*, 87(5):052107, 2013.

[186] Willem Walravens, Eduardo Solano, Filip Geenen, Jolien Dendooven, Oleg Gorobtsov, Athmane Tadjine, Nayyera Mahmoud, Patrick Peiwen Ding, Jacob PC Ruff, Andrej Singer, et al. Setting carriers free, healing faulty interfaces promotes delocalization and transport in nanocrystal solids. *ACS nano*, 13(11):12774–12786, 2019.

[187] J. Tersoff. New empirical approach for the structure and energy of covalent systems. *Phys. Rev. B*, 37:6991–7000, 1988.

[188] Frank H. Stillinger and Thomas A. Weber. Computer simulation of local order in condensed phases of silicon. *Phys. Rev. B*, 31:5262–5271, 1985.

[189] S. Roorda, S. Doorn, W. C. Sinke, P. M. L. O. Scholte, and E. van Loenen. Calorimetric evidence for structural relaxation in amorphous silicon. *Phys. Rev. Lett.*, 62:1880–1883, Apr 1989.

[190] S. Roorda, W. C. Sinke, J. M. Poate, D. C. Jacobson, S. Dierker, B. S. Dennis, D. J. Eaglesham, F. Spaepen, and P. Fuoss. Structural relaxation and defect annihilation in pure amorphous silicon. *Phys. Rev. B*, 44:3702–3725, Aug 1991.

[191] F. Kail, J. Farjas, P. Roura, C. Secouard, O. Nos, J. Bertomeu, and P. Roca i Cabarrocas. The configurational energy gap between amorphous and crystalline silicon. *phys. status solidi (RRL)*, 5(10-11):361–363, 2011.

[192] Albert P. Bartók, James Kermode, Noam Bernstein, and Gabor Csányi. Machine learning a general-purpose interatomic potential for silicon. *Phys. Rev. X*, 8:041048, 2018.

[193] Albert P. Bartók, Mike C. Payne, Risi Kondor, and Gábor Csányi. Gaussian approximation potentials: The accuracy of quantum mechanics, without the electrons. *Phys. Rev. Lett.*, 104:136403, 2010.

[194] Albert P. Bartók, Risi Kondor, and Gábor Csányi. On representing chemical environments. *Phys. Rev. B*, 87:184115, 2013.

[195] Steve Plimpton. Fast parallel algorithms for short-range molecular dynamics. *J. Comput. Phys.*, 117:1–19, 1995.

[196] Manabu Ishimaru, Shinji Munetoh, and Teruaki Motooka. Generation of amorphous silicon structures by rapid quenching: A molecular-dynamics study. *Phys. Rev. B*, 56:15133–15138, Dec 1997.

[197] I. Štich, R. Car, and M. Parrinello. Amorphous silicon studied by ab initio molecular dynamics: Preparation, structure, and properties. *Phys. Rev. B*, 44:11092–11104, Nov 1991.

[198] K. Jarolimek, R. A. de Groot, G. A. de Wijs, and M. Zeman. First-principles study of hydrogenated amorphous silicon. *Phys. Rev. B*, 79:155206, Apr 2009.

[199] P. Giannozzi *et al.* Quantum espresso: a modular and open-source software project for quantum simulations of materials. *J. Phys.: Condens. Matter*, 21:395502, 2009.

[200] P Giannozzi, O Andreussi, T Brumme, O Bunau, M Buongiorno Nardelli, M Calandra, R Car, C Cavazzoni, D Ceresoli, M Cococcioni, N Colonna, I Carnimeo, A Dal Corso, S de Gironcoli, P Delugas, R A DiStasio, A Ferretti, A Floris, G Fratesi, G Fugallo, R Gebauer, U Gerstmann, F Giustino, T Gorni, J Jia, M Kawamura, H-Y Ko, A Kokalj, E Küçükbenli, M Lazzeri, M Marsili, N Marzari, F Mauri, N L Nguyen, H-V Nguyen, A Otero de-la Roza, L Paulatto, S Poncé, D Rocca, R Sabatini, B Santra, M Schlipf, A P Seitsonen, A Smogunov, I Timrov, T Thonhauser, P Umari, N Vast, X Wu, and S Baroni. Advanced capabilities for materials modelling with quantum ESPRESSO. *Journal of Physics: Condensed Matter*, 29(46):465901, oct 2017.

[201] John P. Perdew, Kieron Burke, and Matthias Ernzerhof. Generalized gradient approximation made simple. *Phys. Rev. Lett.*, 77:3865–3868, 1996.

[202] M. Methfessel and A. T. Paxton. High-precision sampling for brillouin-zone integration in metals. *Phys. Rev. B*, 40:3616–3621, Aug 1989.

[203] Khalid Laaziri, S. Kycia, S. Roorda, M. Chicoine, J. L. Robertson, J. Wang, and S. C. Moss. High resolution radial distribution function of pure amorphous silicon. *Phys. Rev. Lett.*, 82:3460–3463, Apr 1999.

[204] Andreas Pedersen, Laurent Pizzagalli, and Hannes Jónsson. Optimal atomic structure of amorphous silicon obtained from density functional theory calculations. *New J. Phys.*, 19(6):063018, jun 2017.

[205] J. Fortner and J. S. Lannin. Radial distribution functions of amorphous silicon. *Phys. Rev. B*, 39:5527–5530, Mar 1989.

[206] Graeme Henkelman and Hannes Jónsson. Improved tangent estimate in the nudged elastic band method for finding minimum energy paths and saddle points. *J. Chem. Phys.*, 113:9978, 2000.

[207] Graeme Henkelman, Blas P. Uberuaga, and Hannes Jónsson. A climbing image nudged elastic band method for finding saddle points and minimum energy paths. *J. Chem. Phys.*, 113:9901, 2000.

[208] Aiichiro Nakano. A space–time-ensemble parallel nudged elastic band algorithm for molecular kinetics simulation. *Comp. Phys. Comm.*, 178:280–289, 2008.

[209] E. Maras, O. Trushin, A. Stukowski, T. Ala-Nissila, and H. Jónsson. Global transition path search for dislocation formation in ge on si(001). *Comp. Phys. Comm.*, 205:13–21, 2016.

[210] Erik Bitzek, Pekka Koskinen, Franz Gähler, Michael Moseler, and Peter Gumbsch. Structural relaxation made simple. *Phys. Rev. Lett.*, 97:170201, 2006.

[211] Abhijit Chatterjee and Arthur F. Voter. Accurate acceleration of kinetic monte carlo simulations through the modification of rate constants. *J. Chem. Phys.*, 132:194101, 2010.

[212] Ariel Amir, Stefano Borini, Yuval Oreg, and Yoseph Imry. Huge (but finite) time scales in slow relaxations: Beyond simple aging. *Phys. Rev. Lett.*, 107:186407, Oct 2011.

[213] R. J. Freitas, K. Shimakawa, and T. Wagner. The dynamics of photoinduced defect creation in amorphous chalcogenides: The origin of the stretched exponential function. *J. Appl. Phys.*, 115(1):013704, 2014.

[214] D. C. Johnston. Stretched exponential relaxation arising from a continuous sum of exponential decays. *Phys. Rev. B*, 74:184430, Nov 2006.

[215] RJ Freitas, K Shimakawa, and T Wagner. The dynamics of photoinduced defect creation in amorphous chalcogenides: The origin of the stretched exponential function. *J. Appl. Phys.*, 115(1):013704, 2014.

[216] M Campos, JA Giacometti, and M Silver. Deep exponential distribution of traps in naphthalene. *Appl. Phys. Lett.*, 34(3):226–228, 1979.

[217] John T Bendler and Michael F Shlesinger. Derivation of the kohlrausch-williams/watts decay law from activation-energy dispersion. *Macromolecules*, 18(3):591–592, 1985.

[218] Stefaan De Wolf, Sara Olibet, and Christophe Ballif. Stretched-exponential a-Si:H/c-Si interface recombination decay. *Appl. Phys. Lett.*, 93(3):032101, 2008.

[219] Ruy S. Bonilla, Bram Hoex, Phillip Hamer, and Peter R. Wilshaw. Dielectric surface passivation for silicon solar cells: A review. *phys. status solidi (a)*, 214(7):1700293, 2017.

[220] Sara Olibet, Evelyne Vallat-Sauvain, and Christophe Ballif. Model for a-Si:H/c-Si interface recombination based on the amphoteric nature of silicon dangling bonds. *Phys. Rev. B*, 76:035326, Jul 2007.

[221] Sara Olibet, Evelyne Vallat-Sauvain, Luc Fesquet, Christian Monachon, Aïcha Hessler-Wyser, Jérôme Damon-Lacoste, Stefaan De Wolf, and Christophe Ballif. Properties of interfaces in amorphous/crystalline silicon heterojunctions. *phys. status solidi (a)*, 207(3):651–656, 2010.

[222] T. F. Schulze, H. N. Beushausen, C. Leendertz, A. Dobrich, B. Rech, and L. Korte. Interplay of amorphous silicon disorder and hydrogen content with interface defects in amorphous/crystalline silicon heterojunctions. *Appl. Phys. Lett.*, 96(25):252102, 2010.

[223] M. Stuckelberger, M. Despeisse, G. Bugnon, J.-W. Schüttauf, F.-J. Haug, and C. Ballif. Comparison of amorphous silicon absorber materials: Light-induced degradation and solar cell efficiency. *J. Appl. Phys.*, 114(15):154509, 2013.

[224] Jakub Holovský, Silvia Martín De Nicolás, Stefaan De Wolf, and Christophe Ballif. Amorphous/crystalline silicon interface stability: Correlation between infrared spectroscopy and electronic passivation properties. *Adv. Mater. Interfaces*, 7(20):2000957, 2020.

[225] T. F. Schulze, L. Korte, F. Ruske, and B. Rech. Band lineup in amorphous/crystalline silicon heterojunctions and the impact of hydrogen microstructure and topological disorder. *Phys. Rev. B*, 83:165314, Apr 2011.

[226] A. H. M. Smets, W. M. M. Kessels, and M. C. M. van de Sanden. Vacancies and voids in hydrogenated amorphous silicon. *Appl. Phys. Lett.*, 82(10):1547–1549, 2003.

[227] Simone Bernardini. *Efficiency-limiting recombination mechanisms in high-quality crystalline silicon for solar cells*. PhD thesis, Arizona State University, 2018.

[228] Z. Wu, L. Zhang, W. Liu, R. Chen, Z. Li, F. Meng, and Z. Liu. Role of hydrogen in modifying a-Si: H/c-Si interface passivation and band alignment for rear-emitter silicon heterojunction solar cell. *J. Mater. Sci. Mater. Electron.*, 31:9468–9474, 2020.

[229] A. MacKinnon and B. Kramer. The scaling theory of electrons in disordered solids: Additional numerical results. *Zeitschrift für Physik B Condensed Matter*, 53(1):1–13, Mar 1983.

[230] A. Eilmes, R. A. Römer, and M. Schreiber. The two-dimensional anderson model of localization with random hopping. *The European Physical Journal B - Condensed Matter and Complex Systems*, 1(1):29–38, Jan 1998.

[231] Anders W. Sandvik, Adolfo Avella, and Ferdinando Mancini. Computational studies of quantum spin systems. 2010.